

AASERT Grant #N00014-93-1-0827

**Final Progress Report**  
(covering the period of 7/1/93-6/30-97)

**Project Title: Investigation of Normal Incidence High  
Performance P-type Strained Layer  
InGaAs/AlGaAs and GaAs/AlGaAs Quantum  
Well Infrared Photodetectors.**

Submitted to

Max N. Yoder

Office of Naval Research  
Code 3410  
800 North Quincy Street  
Arlington, VA 22217-5000

Prepared by

Jerome T. Chu  
Student

and

Sheng S. Li  
Professor

Department of Electrical and Computer Engineering  
University of Florida  
Gainesville, FL 32611

Tel. & Fax (352) 392-4937  
e-mail: ShengLi@eng.ufl.edu

DTIC QUALITY INSPECTED 3

19970603 101

June 30, 1997

DISTRIBUTION STATEMENT A

Approved for public release;  
Distribution Unlimited

AASERT Grant #N00014-93-1-0827

**Final Progress Report**  
(covering the period of 7/1/93-6/30-97)

**Project Title: Investigation of Normal Incidence High  
Performance P-type Strained Layer  
InGaAs/AlGaAs and GaAs/AlGaAs Quantum  
Well Infrared Photodetectors.**

Submitted to

Max N. Yoder

Office of Naval Research  
Code 3410  
800 North Quincy Street  
Arlington, VA 22217-5000

Prepared by

Jerome T. Chu  
Student

and

Sheng S. Li  
Professor

Department of Electrical and Computer Engineering  
University of Florida  
Gainesville, FL 32611

Tel. & Fax (352) 392-4937  
e-mail: ShengLi@eng.ufl.edu

DNIC QUALITY INSPECTED 8

June 30, 1997

**REPORT DOCUMENTATION PAGE**Form Approved  
OMB No. 0704-0188

Public reporting burden for this collection of information is estimated to average 1 hour per response, including the time for reviewing instructions, searching existing data sources, gathering and maintaining the data needed, and completing and reviewing the collection of information. Send comments regarding this burden estimate or any other aspect of this collection of information, including suggestions for reducing this burden, to Washington Headquarters Services, Directorate for Information Operations and Reports, 1215 Jefferson Davis Highway, Suite 1204, Arlington, VA 22202-4302, and to the Office of Management and Budget, Paperwork Reduction Project (0704-0188), Washington, DC 20503.

**1. AGENCY USE ONLY** (Leave blank)**2. REPORT DATE**

30 June 1997

**3. REPORT TYPE AND DATES COVERED**

Final Progress Report 7/1/93-6/30/97

**4. TITLE AND SUBTITLE**

Investigation of Normal Incident High Performance P-type Strained Layer InGaAs/AlGaAs and GaAs/AlGaAs QWIPs

**5. FUNDING NUMBERS**

ONR #N00014-93-1-0827

**6. AUTHOR(S)**Jerome T. Chu, Student  
Sheng S. Li, Professor**7. PERFORMING ORGANIZATION NAME(S) AND ADDRESS(ES)**University of Florida  
Gainesville, FL 32511-6200**8. PERFORMING ORGANIZATION  
REPORT NUMBER**

92120712

**9. SPONSORING/MONITORING AGENCY NAME(S) AND ADDRESS(ES)**US Navy, Office of Naval Research  
800 North Quincy Street, Code 1512B:SM  
Arlington, VA 22217-5000**10. SPONSORING/MONITORING  
AGENCY REPORT NUMBERS****11. SUPPLEMENTARY NOTES****12a. DISTRIBUTION/AVAILABILITY STATEMENT**

Approved for public release, distribution unlimited.

**12b. DISTRIBUTION CODE****13. ABSTRACT** (Maximum 200 words)

In this research project, we have demonstrated several novel strained layer p-type quantum well infrared photodetectors (QWIPs) for the 3-5  $\mu\text{m}$  mid-wavelength infrared (MWIR) and 8-14  $\mu\text{m}$  long-wavelength infrared (LWIR) detection. These normal incidence p-QWIPs employed the tensile- and compressive-strained layer quantum well structures (e.g., InGaAs/InAlAs on InP and InGaAs/AlGaAs on GaAs) to enhance the performance of the p-QWIPs in the MWIR and LWIR spectral bands. Peak detection wavelengths at 7.4, 8.4, 9.2 and 10.1  $\mu\text{m}$  with corresponding detectivities of  $4 \times 10^9$ ,  $1.66 \times 10^{10}$ ,  $2.7 \times 10^9$  and  $1.04 \times 10^9 \text{ cm-Hz}^{1/2}/\text{W}$  were obtained for these QWIPs. In addition, a novel step-bound-to-miniband InGaAs/GaAs/AlGaAs p-QWIP with a peak wavelength at 10.4  $\mu\text{m}$  and  $D^* = 4 \times 10^9 \text{ cm-Hz}^{1/2}/\text{W}$  and a two-stack p-QWIP with peak wavelengths at 10, 5.4 and 4.8  $\mu\text{m}$ ,  $D^* = 1.1 \times 10^{10}$  for the LWIR and  $5.5 \times 10^{11} \text{ cm-Hz}^{1/2}/\text{W}$  for the MWIR were obtained for these QWIPs. Finally, a tensile strain layer InGaAs/InAlAs p-QWIP with very low dark current, high detectivity and high BLIP temperature has also been demonstrated.

**14. SUBJECT TERMS**

P-type strained layer InGaAs/GaAs/AlGaAs quantum well infrared photodetectors (QWIPs), intersubband absorption, dark current, responsivity, detectivity, normal incidence response

**15. NUMBER OF PAGES****16. PRICE CODE****17. SECURITY  
CLASSIFICATION OF REPORT**

Unclassified

**18. SECURITY  
CLASSIFICATION OF THIS  
PAGE****19. SECURITY  
CLASSIFICATION OF  
ABSTRACT****20. LIMITATION OF ABSTRACT**

Unlimited

## Contents

<b>1</b>	<b>Introduction</b>	<b>7</b>
<b>2</b>	<b>Project Summary</b>	<b>8</b>
2.1	Research Accomplishments . . . . .	8
2.2	Publications . . . . .	10
<b>3</b>	<b>P-QWIP Theory</b>	<b>14</b>
3.1	General P-QWIP Design Parameters . . . . .	14
3.2	P-QWIP Physics . . . . .	14
3.2.1	Strained Layer Growth Limitations and Theory . . . . .	14
3.2.2	Strain Induced Energy Band Shifts . . . . .	16
3.2.3	Energy Band Calculations . . . . .	17
3.2.4	The Transfer Matrix Method for the Calculation of Transmission Probability . . . . .	20
3.2.5	Determination of Intersubband Transitions and Absorption Coefficients	22
3.2.6	Photoconductive Detection Mode Operation . . . . .	23
3.3	P-QWIP Figures of Merit . . . . .	24
3.3.1	Spectral Responsivity . . . . .	24
3.3.2	QWIP Collection Efficiency . . . . .	25
3.3.3	Dark Current Relationship in a QWIP . . . . .	26
3.3.4	Noise in QWIPs . . . . .	27
<b>4</b>	<b>Technical Results</b>	<b>29</b>
4.1	An $\text{In}_{0.3}\text{Ga}_{0.7}\text{As}/\text{In}_{0.52}\text{Al}_{0.48}\text{As}$ on InP P-QWIP with Tensile Strain . . . . .	29
4.2	An $\text{In}_{0.4}\text{Ga}_{0.6}\text{As}/\text{GaAs}$ on GaAs P-QWIP with compressional strain . . . . .	38
4.3	An $\text{InGaAs}/\text{AlGaAs}$ on GaAs P-QWIP with compressive strain layers . . . . .	46
4.4	A novel Si-doped GaAs/AlGaAs on (311) SI GaAs p-QWIP . . . . .	56

4.5	New compressively strained InGaAs/AlGaAs p-QWIPs for 10.1 and 9.2 $\mu\text{m}$ detection . . . . .	60
4.6	A New p-type InGaAs/GaAs/AlGaAs SBTM QWIP at 10.4 $\mu\text{m}$ . . . . .	66
4.7	Noise Performance of a p-type Strained-layer QWIPs . . . . .	75
4.8	A Stacked Two-color Two-band Compressively Strained-Layer P-QWIP . . .	82
<b>5</b>	<b>Conclusion and Remarks</b>	<b>90</b>

## List of Figures

1	(a) Schematic energy band diagram for the tensile strain P-QWIP and the calculated energy levels in the quantum well for the P-QWIP (b) without and (c) with 1.6% tensile strain. . . . .	33
2	(a) Calculated absorption coefficient at normal incidence for a P-QWIP both with and without strain, and (b) measured dark current density and 300 K background photocurrent density. . . . .	34
3	Measured P-QWIP photoresponse at $T = 77$ K for (a) forward bias and (b) reverse bias. . . . .	35
4	% BLIP for the strained-layer P-QWIP as a function of applied bias. . . . .	36
5	Responsivity as a function of bias and device temperature. . . . .	37
6	Schematic of the compressive strain layer InGaAs/GaAs on GaAs p-QWIP (a) and the strain-layer energy band calculations (b). . . . .	41
7	Measured responsivities in the LWIR band (a) and the MWIR band (b) for the InGaAs/GaAs PCSL-QWIP. . . . .	42
8	Measured responsivity of the InGaAs/GaAs PCSL-QWIP as a function of applied bias for $\lambda_p = 8.9 \mu\text{m}$ . . . . .	43
9	Measured responsivity of the InGaAs/GaAs PCSL-QWIP as a function of applied bias for $\lambda_p = 5.5 \mu\text{m}$ . . . . .	44
10	Measured dark current for the InGaAs/GaAs PCSL-QWIP as a function of applied bias and device temperature. . . . .	45
11	The schematic diagram for the two-color two-band compressively strained InGaAs/AlGaAs p-QWIP. . . . .	50
12	Dark current characteristic of the InGaAs/AlGaAs CSL p-QWIP. . . . .	51
13	LWIR responsivity of the InGaAs/AlGaAs CSL p-QWIP at 77 K and +5.0 V bias. . . . .	52
14	MWIR responsivity of the InGaAs/AlGaAs CSL p-QWIP at 77 K and +5.0 V bias. . . . .	53

15	(a) LWIR responsivity at $\lambda_p = 7.4 \mu\text{m}$ and (b) MWIR responsivity at $\lambda_p = 5.5 \mu\text{m}$ as a function of applied bias and temperature. . . . .	54
16	Experimental and theoretical current noise spectral density versus reverse bias voltage for various temperatures. . . . .	55
17	Dark current characteristic for the Si-doped unstrained GaAs/AlGaAs p-QWIP.	58
18	Normalized responsivity for the Si-doped p-QWIP. . . . .	59
19	Dark current characteristic for the CSL InGaAs/AlGaAs p-QWIP with a detective peak at $\lambda_p = 10.1 \mu\text{m}$ . . . . .	62
20	Dark current characteristic for the CSL InGaAs/AlGaAs p-QWIP with a detective peak at $\lambda_p = 9.2 \mu\text{m}$ . . . . .	63
21	Measured LWIR responsivity of the $\lambda_p = 10.1 \mu\text{m}$ CSL p-QWIP at 55 K and -1.0 V bias. Estimated $D^* = 1.04 \times 10^9$ Jones. . . . .	64
22	Measured LWIR responsivity of the $\lambda_p = 9.2 \mu\text{m}$ CSL p-QWIP at 45 K and -2.5 V bias. Estimated $D^* = 2.7 \times 10^9$ Jones. . . . .	65
23	The schematic diagram for new $10.4 \mu\text{m}$ peak compressively strained InGaAs/AlGaAs/GaAs p-type SBTM CSL-QWIP. . . . .	69
24	The calculated transmission peaks for the InGaAs/AlGaAs/GaAs compressively strained p-type SBTM CSL-QWIP. . . . .	70
25	The layer structure for the p-type SBTM CSL-QWIP. . . . .	71
26	Measured dark I-V and 300 K background photocurrents for the p-type SBTM CSL-QWIP. . . . .	72
27	The measured photoresponse versus incident IR wavelength at $T=60 \text{ K}$ , $V=2.0 \text{ V}$ for the p-type SBTM CSL-QWIP. . . . .	73
28	The measured responsivity versus bias at $10.4 \mu\text{m}$ and various temperatures.	74
29	Current noise spectral density versus frequency at different bias voltages and temperatures. . . . .	78
30	Current noise spectral density versus dark current for various temperatures. .	79
31	Measured and calculated dark currents of the $7.4 \mu\text{m}$ peak InGaAs/AlGaAs at low bias voltages and different temperatures. . . . .	80

32	Measured and calculated dark current of the 9.2 $\mu\text{m}$ peak p-QWIP at low applied biases and various temperatures. . . . .	81
33	The energy band diagrams and intersubband transition scheme for the two-color stacked PCSL-InGaAs/AlGaAs QWIP for the MWIR and LWIR detection.	85
34	The dark I-V characteristics for (a) the stacked, MWIR, and LWIR PCSL-QWIP, and (b) the LWIR QWIP for $T = 40, 60,$ and $77\text{ K}$ . . . . .	86
35	The spectral responsivity versus wavelength for the MWIR PCSL-QWIP, measured at $T = 77\text{ K}$ and $V = 5\text{ V}$ . Two response peaks at 4.8 $\mu\text{m}$ and 5.4 $\mu\text{m}$ were observed for this device. . . . .	87
36	The spectral responsivity versus wavelength for the LWIR PCSL-QWIP, measured at $T = 40\text{ K}$ and $V = 2\text{ V}$ . One response peak at 10 $\mu\text{m}$ was obtained for this device. . . . .	88
37	The relative photoresponse versus wavelength for the combined stacked PCSL-QWIP. Three photoresponse bands were detected in this stacked QWIP. . .	89
38	The comparison of the (a) photoresponse and (b) detectivity between the strained and unstrained p-QWIPs at the same operating biases. . . . .	93



## 1 INTRODUCTION

During the period of this project (July 1993 to June 1997), significant progress has been made towards the design, fabrication, and characterization of new strained layer p-type GaAs/InGaAs on GaAs and InGaAs/AlGaAs on GaAs quantum-well infrared photodetectors (p-QWIPs) in the 8-14  $\mu\text{m}$  range for staring focal plane arrays (FPAs). Specific tasks performed during this project include: (i) the design, fabrication, and characterization of a normal incidence tensile strained-layer p-type InGaAs/InAlAs QWIP on InP with a detection peak at 8.1  $\mu\text{m}$ , (ii) the design, fabrication, and characterization of a compressively strained InGaAs/GaAs p-QWIP with two long-wavelength infrared (LWIR) band peaks at 8.4 and 8.9  $\mu\text{m}$  and a mid-wavelength infrared (MWIR) peak at 5.5  $\mu\text{m}$ , (iii) the design, fabrication, and characterization of a compressively strained InGaAs/AlGaAs p-QWIP with a detection peaks at 7.5 and 5.5  $\mu\text{m}$ , (iv) the design, fabrication, and characterization of a novel Si-doped InGaAs/AlGaAs p-QWIP on a (311) GaAs substrate which exhibited MWIR response peaks at 3.0 and 5.2  $\mu\text{m}$ , (v) the design, growth, and characterization of two compressively strained InGaAs/AlGaAs p-QWIPs with LWIR responsivity peaks at 9.2 and 10.1  $\mu\text{m}$ , (vi) the design, fabrication, and characterization of the first p-type QWIP to utilize the step bound-to-miniband transition scheme with a peak detective wavelength at 10.4  $\mu\text{m}$ , (vii) the modeling and characterization of the dark current and noise in p-type QWIPs at low applied biases, and (viii) the design, fabrication, and characterization of a stacked two-band two-color compressively strained-layer InGaAs/AlGaAs p-QWIP with responsivity peaks at 10, 5.4, and 4.8  $\mu\text{m}$ . The following sections of this report will cover the technical results of the study obtained during this reporting period and the research accomplishments and publications. A summary of the various types of p-QWIPs studied is listed at the end of this report in table A.

## 2 PROJECT SUMMARY

### 2.1 Research Accomplishments

1. The demonstration and characterization of an ultra-low dark current strained layer InGaAs/InAlAs p-QWIP with a  $\lambda_p = 8.1 \mu\text{m}$ . The background limited detectivity was found to be  $5.9 \times 10^{10} \text{ cm}\sqrt{\text{Hz}}/\text{W}$  at  $T=77 \text{ K}$  with BLIP limited operation up to 90 K. These are the highest reported BLIP conditions for a QWIP.
2. The design, growth, fabrication, and characterization of a compressively strained p-type InGaAs/GaAs QWIP on a GaAs substrate with peak wavelengths of  $\lambda_{p1,2} = 8.4, 8.9 \mu\text{m}$  and  $\lambda_{p3} = 5.5 \mu\text{m}$ . Maximum responsivities of 93 mA/W and 30 mA/W were measured for each respective peak wavelength at 75 K. BLIP performance was achieved in the long-wavelength infrared (LWIR) detection band at  $T=70 \text{ K}$  and under 0.3 V of applied bias. This device exhibited a spectral bandwidth of  $\Delta\lambda/\lambda_p = 35 \%$  in the LWIR band and  $\Delta\lambda/\lambda_p = 27 \%$  in the MWIR band.
3. The design, growth, fabrication and characterization of a compressively strained InGaAs/AlGaAs p-QWIP on a (100) GaAs substrate with a peak detection wavelength of  $7.5 \mu\text{m}$  and a MWIR peak at  $5.5 \mu\text{m}$ . Very low dark current densities were measured for this device at 77 K. Maximum responsivities of 40 mA/W and 8 mA/W were measured for each of the respective peak wavelengths at 77 K under an applied bias of +5.0 V with operation at up to 85 K possible under moderate bias ( $\leq 2 \text{ V}$ ). BLIP performance was achieved in both detection bands at 63 K within the applied bias range of -2.7 to 3.0 V. Measured detectivity ( $D^*$ ) at  $T=81 \text{ K}$  and  $V=1.0 \text{ V}$  was  $1.06 \times 10^{10} \text{ cm}\sqrt{\text{Hz}}/\text{W}$ . Using mechanical techniques for responsivity improvements a detectivity of  $1.66 \times 10^{10}$  was achieved at 81 K and 1.0 V of bias. In addition, extensive noise characterization studies were performed and the results are presented.
4. The design, growth, fabrication and characterization of a Si-doped InGaAs/AlGaAs p-QWIP on a 311 GaAs substrate with peak detection wavelengths at  $3.0$  and  $5.2 \mu\text{m}$  in the MWIR band. Highly symmetrical dark current densities were found for this unstrained device at all measured temperatures (40 to 120 K).

5. The design, growth, fabrication and characterization of two Be-doped compressively strained InGaAs/AlGaAs p-QWIPs on SI (100) GaAs substrates with peak wavelengths at 9.3 and 10.1  $\mu\text{m}$ , respectively. The 9.3  $\mu\text{m}$  p-QWIP exhibits a peak responsivity of 28 mA/W at  $T=45$  K under a bias of -2.5 V; while the 10.1  $\mu\text{m}$  p-QWIP has a maximum responsivity of 17 mA/W at  $T=55$  K and  $V=-1.0$  V. BLIP operation is achieved when the 9.2  $\mu\text{m}$  p-QWIP for positive biases under 2.0 V and at temperatures less than 45 K. Similarly, the 10.1  $\mu\text{m}$  p-QWIP exhibits BLIP operation when the applied bias is under 1.0 V at  $T=46$  K.
6. The design, growth, fabrication, and characterization of a Be-doped compressively strained InGaAs/GaAs/AlGaAs p-QWIP on SI GaAs with a peak detection wavelength at 10.4  $\mu\text{m}$ , which utilizes the step bound-to-miniband transition scheme for photoexcited carrier transport. The observed peak responsivity at  $T=65$  K and  $V_b=3.0$  V was 28 mA/W. This device was BLIP limited when  $T \leq 40$  K with the corresponding bias of  $\leq |2V|$ . The calculated spectral detectivity at  $T=65$  K and  $V=1.0$  V was determined to be  $1.4 \times 10^9 \text{ cm}\sqrt{\text{Hz}}/\text{W}$ .
7. The characterization of the dark current noise performance of a 7.4  $\mu\text{m}$  peak p-type compressively strained-layer quantum well infrared photodetector between  $10^1$  and  $10^5$  Hz. A value of  $2.6 \times 10^{-13} \text{ cm}^2$  was determined for the scattering cross section at 100 K.
8. The noise characterization of a p-type compressively strained QWIP with a detection peak at 9.2  $\mu\text{m}$  at low applied biases. Using this data, we were able to model the dark current characteristics of the p-type QWIPs. Excellent agreement was obtained between the measured and calculated dark I-V characteristics.
9. The characterization of a stacked dual band two-color p-QWIP grown on (100) SI GaAs with peak responsivities at 10 and 4.8  $\mu\text{m}$  in the LWIR and MWIR bands. This device demonstrates the ability of p-type QWIPs to sense radiation in both infrared bands of interest separately or simultaneously depending on the readout format. The LWIR detection peak at  $\lambda_p = 10 \mu\text{m}$  exhibited a responsivity of 25 mA/W at  $V_b = 2$  V,  $T = 40$  K, with a FWHM of  $\Delta\lambda/\lambda_p = 40\%$ , and the calculated detectivity was found to be  $D^* = 1.1 \times 10^{10} \text{ cm}\sqrt{\text{Hz}}/\text{W}$ . Two response peaks for the MWIR QWIP were found

to be at 4.8  $\mu\text{m}$  and 5.4  $\mu\text{m}$  with maximum responsivities of 12 and 19 mA/W ( at  $T = 77\text{ K}$  and  $V_b = 5\text{ V}$ ), and spectral bandwidths of 21% and 26%, respectively. The detectivity ( $D^*$ ) for the MWIR stack determined at  $\lambda_p = 5.4\text{ }\mu\text{m}$ ,  $V_b = 1.0\text{ V}$  and  $T = 77\text{ K}$  was found to be  $5.5 \times 10^{11}\text{ cm}\sqrt{\text{Hz}}/\text{W}$ .

## 2.2 Publications

### A. Journal Papers:

1. Y. H. Wang, S. S. Li, and J. Chu and Pin Ho, "An Ultra-low Dark Current P-type Strained-layer InGaAs/InAlAs Quantum Well Infrared Photodetector with Background Limited Performance (BLIP)" *Appl. Phys. Letts*, **64**(4), 727 (1994).
2. Y. H. Wang, S. S. Li, and J. Chu and Pin Ho, "A Normal Incidence P-type Compressive Strained-Layer InGaAs/GaAs Quantum Well Infrared Photodetector for Mid-Wavelength Infrared (MWIR) and Long-Wavelength Infrared (LWIR) Detection" *J. Appl. Phys.*, **76**(10), 6009 (1994).
3. D. C. Wang, G. Bosman, and S. S. Li, "Noise Characterization and Device Parameter Extraction on a p-type Strained Layer Quantum Well Infrared Photodetector", *J. Appl. Phys.*, **79**(3), 1486 (1996).
4. J. Chu, S. S. Li, and P. Ho, "A New Compressively Strained P-type Quantum Well Infrared Photodetector Using the Step Bound-to-miniband Detection Scheme", *Appl. Phys. Lett.*, **69**(9), 1258 (1996).
5. D. C. Wang, G. Bosman, and S. S. Li, "Current Conduction and Noise Characteristics of Quantum Well Infrared Photodetectors Under Low Bias Operation", *Appl. Phys. Lett.*, **68**(18), 2532 (1996).
6. S. S. Li, J. Chu, Y. H. Wang, "Investigation of P-type Strained-Layer  $\text{In}_x\text{Ga}_{1-x}\text{As}/\text{Al}_y\text{Ga}_{1-y}\text{As}$  Quantum Well Infrared Photodetectors for Long Wavelength Infrared Imaging Arrays Applications", *Superlattices and Microstructures*, **19**(3), 229 (1996).
7. J. Chu, S. S. Li, and P. Ho, "The Growth and Characterization of Two P-type Compressively Strained-layer InGaAs/AlGaAs/GaAs Quantum Well Infrared Photodetec-

tors for Mid- and Long-Wavelength Infrared Detection", accepted for publication in the *J. Crystal Growth*, Dec. 1996.

8. A. Chin, C. C. Liao, J. Chu, and S. S. Li, "Investigation of Si-doped P-type AlGaAs/GaAs, AlGaAs/InGaAs Quantum Well Infrared Photodetectors and Multiquantum Wells Grown on 311(A) GaAs", accepted for publication in the *J. Crystal Growth*, Dec. 1996.
9. J. Chu and S. S. Li, "The Effect of Compressive Strain on the Performance of P-Type Quantum Well Infrared Photodetectors", accepted for publication in the *IEEE J. Quantum Electronics*, July 1997 issue.

#### **B. Conference Presentations:**

1. S. S. Li, J. Chu, and Y. H. Wang, "A Normal Incidence P-type Strained Layer InGaAs/InAlAs Quantum Well Infrared Photodetector with Background Limited Performance at 77 K", presented at the 1994 SPIE symposium, Orlando, FL, April 4-8, 1994. Full paper published in the conference proceedings.
2. Pin Ho, Y. H. Wang, S. S. Li, and J. Chu, "MBE Growth of P-type Strained-layer InGaAs/InAlAs QWIPs", presented at the 1994 14th North American Conference on Molecular-beam Epitaxy, Urbana-Champaign, IL, October 10-12, 1994.
3. Y. H. Wang, J. Chu, S. S. Li, and Pin Ho, "A Normal Incidence P-type Compressive Strained-Layer InGaAs/GaAs Quantum Well Infrared Photodetector", 2nd. International Conference on 2-20  $\mu\text{m}$  Wavelength Infrared Detectors and Arrays, Miami Beach, FL, October 9-14, 1994. Full paper published in the conference proceedings.
4. S. S. Li, Y. H. Wang, and J. Chu, "A New Class of Normal Incidence Strained-Layer III-V Quantum Well Infrared Photodetectors", presented at the 1994 LEOS Conference, Boston, MA, October 31-November 3, 1994. Full paper published in the conference proceedings.
5. J. Chu, Y. H. Wang, S. S. Li, and Pin Ho, "A New Compressively Strained InGaAs/AlGaAs p-type Quantum Well Infrared Photodetector with Ultra-low Dark Cur-

- rent and Detective Peaks in the LWIR and MWIR Bands", presented at the 3rd. International Symposium on Long Wavelength Infrared Detectors and Arrays: Physics and Applications, Chicago, IL, October 9-11, 1995. Full paper published in the conference proceedings.
6. J. Chu, S. S. Li, S. Y. Yen, A. Chin, and K. M. Chang, "Investigation of Si-doped p-type GaAs/AlGaAs and Strained-layer InGaAs/AlGaAs Quantum Well Infrared Photodetectors grown on (311) GaAs for Mid- and Long-Wavelength IR Detection", presented at the 3rd. International Symposium on Long Wavelength Infrared Detectors and Arrays: Physics and Applications, Chicago, IL, October 9-11, 1995.
  7. D. Wang, G. Bosman, S. S. Li, and J. Chu, "Noise Performance of p-type Strained Layer Quantum Well Infrared Photodetectors", presented at the 3rd. International Symposium on Long Wavelength Infrared Detectors and Arrays: Physics and Applications, Chicago, IL, October 9-11, 1995. Full paper published in conference proceedings.
  8. S. S. Li, J. Chu, and Y. H. Wang, "P-type Strained-layer III-V Quantum Well Infrared Photodetectors for Long-wavelength Infrared Focal Plane Array Applications", invited paper, presented at the Int. Conf. on Intersubband Transitions in Quantum Wells (ITQW '95), Kibbutz Ginosar, Israel, Oct. 23-26, 1995. Full paper published in the conference proceedings.
  9. A. Chin, C. C. Liao, J. Chu, and S. S. Li, "Investigation of Si-doped P-type AlGaAs/GaAs, AlGaAs/InGaAs Quantum Well Infrared Photodetectors and Multiquantum Wells grown on 311(A) GaAs", presented at the 9th International Molecular Beam Epitaxy Conference, Malibu, CA, August 5-6, 1996. Full paper published in the conference proceedings.
  10. J. Chu, S. S. Li, and Pin Ho, "The Growth and Characterization of Two P-type Compressively Strained-layer InGaAs/AlGaAs/GaAs Quantum Well Infrared Photodetectors for Mid- and Long-Wavelength Infrared Detection", presented at the 9th International Molecular Beam Epitaxy Conference, Malibu, CA, August 5-9, 1996. Full paper published in the conference proceedings.

11. S. S. Li and J. Chu, "The Effect of Compressive Strain on the Performance of P-type Quantum Well Infrared Photodetectors", invited paper, presented at SPIE 97, San Jose, CA, Feb 12-14, 1997. Full paper published in the conference proceedings.

### 3 P-QWIP THEORY

#### 3.1 General P-QWIP Design Parameters

With the advent of molecular beam epitaxial technologies in the last few decades, device structures utilizing heterostructure quantum wells have been heavily explored. N-type quantum well infrared photodetectors (QWIPs) have been extensively studied in recent years [1, 2, 28]. These systems use GaAs/AlGaAs and InGaAs/InAlAs structures for detection in the 3 - 5  $\mu\text{m}$  mid-wavelength infrared (MWIR) and 8 - 14  $\mu\text{m}$  LWIR atmospheric transmission windows. Since n-type GaAs/InGaAs and InGaAs/InAlAs QWIPs have inherently low electron effective masses and high electron mobilities, they offer excellent infrared (IR) detection properties. Due to the quantum mechanical selection rules which prohibit normal incidence intersubband absorption, focal plane arrays (FPA) using n-type QWIPs must use either metal or dielectric gratings to couple normal incidence IR radiation into the quantum well [2, 3, 4]. In contrast, because of the mixing between the light hole and heavy hole states under either biaxial tension or compressive strain, normal incidence illumination is allowed for the intersubband transition in p-type QWIPs; thus eliminating the need for metal or dielectric grating couplers.

#### 3.2 P-QWIP Physics

##### 3.2.1 Strained Layer Growth Limitations and Theory

P-type QWIPs using valence intersubband transitions have been demonstrated [5, 6, 7] in lattice-matched GaAs/AlGaAs and InGaAs/InAlAs material systems. In general, intersubband transitions excited by normal incidence radiation in p-type quantum wells are allowed since a linear combination of p-like valence band Bloch states exists, which provides a nonzero coupling between the normal radiation field and valence band Bloch states. The strong mixing between the heavy hole and the light hole states greatly enhances intersubband absorption. The drawback of using lattice-matched systems is the fact that the intersubband transition occurs between the heavy hole ground states and the upper excited states. Because of the relatively large heavy hole effective mass when compared to the electron effective



mass, relatively weak absorption and therefore similarly low responsivity is predicted in the IR wavelength range when compared to n-type QWIPs. In order to increase the absorption characteristics and responsivity of P-QWIPs, biaxial stress is introduced into the well layers of the QWIP structure. If the intentionally introduced biaxial stress between the well layers and the barrier layers contained in the layer thickness (the total thickness of the wells and barriers) in the P-QWIP structure is less than the critical thickness, then pseudomorphic or coherent heterointerfaces can be grown without the introduction of defects between the layers. Based upon the force balance model [8, 28, 29, 30], the equilibrium critical layer thickness,  $L_c$ , for an epilayer with the lattice constant,  $a$ , grown on a substrate with a lattice constant,  $a_s$ , is given as

$$L_c = \left( \frac{a}{\sqrt{2}\delta_o} \right) \frac{1 - \nu \cos^2 \Theta}{8\pi(1 + \nu) \cos \alpha} \left[ 1 + \ln(h\sqrt{2}/a) \right], \quad (1)$$

where  $h$  is the epilayer thickness,  $\Theta$  is the angle between the dislocation line and the Burges' vector,  $\alpha$  is the angle between the slip direction and the layer plane direction,  $\delta_o$  is the lattice-mismatch or the in-plane strain, and  $\nu$  is the Poisson ratio.  $\delta_o$  is defined as  $\delta_o = (a_s - a)/a$  where  $\delta_o > 0$  for tensile strain and  $\delta_o < 0$  for compressive strain. Similarly,  $\nu$  is defined as  $\nu = -C_{12}/C_{11}$ .  $C_{ij}$ 's are the elastic constants and can be found in reference [9].

The strained-layers have the same effective in-plane lattice constant,  $a_{||}$  (i.e.,  $a_{x,y}$ ), and can store the excess energy due to the elastic strain within the layers. The in-plane lattice constant,  $a_{||}$ , can be expressed by [8]

$$a_{||} = a_1 \left[ 1 + \delta_o / \left( 1 + \frac{\xi_1 L_1}{\xi_2 L_2} \right) \right], \quad (2)$$

where  $a_{1,2}$  and  $L_{1,2}$  are the individual layer lattice constants and thicknesses, respectively, and  $\xi_{1,2}$  are the shear moduli as described by  $\xi = (C_{11} + C_{12} - 2C_{12}^2/C_{11})$ , where the  $C_{ij}$ 's are elastic constants for the strained material.  $\delta_o$  denotes the lattice mismatch between layers and  $a_{1,2}$  are the lattice constants of the strained well and the substrate (or barrier) respectively. When  $a_{||} \neq a_s$ , the coherently strained superlattice structure is no longer in equilibrium with the substrate. If the lattice constant of the barrier layers is equal to that of the substrate, the strain will be completely accommodated in the well layers with no strain in the barrier layers. However, Hull *et al.* [22] showed that if the individual layer thickness in the superlattice is less than its critical thickness, even though  $a_{||} \neq a_s$ , the loss

only occurs at the interface between the whole superlattice and the substrate, while the superlattice itself remains coherent.

### 3.2.2 Strain Induced Energy Band Shifts

If the QWIP structure is grown along the [100] direction and the strained-layer is within the critical thickness,  $L_c$ , then a pseudomorphic or coherent heterointerface can be obtained and the components of the strain tensor  $[e]$  are simplified to the expressions given by

$$e_{xx} = e_{yy} = e_{||} \quad (3)$$

$$e_{zz} = -e_{||} \left( \frac{2C_{12}}{C_{11}} \right) \quad (4)$$

$$e_{xy} = e_{yz} = e_{zx} = 0. \quad (5)$$

In addition to altering the physical parameters of the QWIP, lattice strain can also induce energy band shifts, which can be used to alter the absorption characteristics of the QWIP. The strain induced energy band shifts for the conduction band, the heavy hole subband, and light hole subband can be approximated as follows.

$$\Delta E_c = 2c_1 \frac{C_{11} - C_{12}}{C_{11}} \delta_o \quad (6)$$

$$\Delta E_{hh} = b \frac{C_{11} + C_{12}}{C_{11}} \delta_o \quad (7)$$

$$\Delta E_{lh} = -\Delta E_{hh} + \frac{(\Delta E_{hh})^2}{2\Delta_o} \quad (8)$$

where  $c_1$  is the combined hydrostatic deformation potential which characterizes the splitting of the  $\Gamma_8$  valence band under strain, and  $b$  is the shear deformation potential, and  $\Delta_o$  is the spin orbit split-off energy<sup>9</sup>. The total hydrostatic deformation potential ( $c_1 + V_v$ ), where  $V_v$  is the valence band deformation potential, can be expressed by [10]

$$c_1 + V_v = -\frac{1}{3}(C_{11} + 2C_{12}) \frac{dE_g^o}{dP}, \quad (9)$$

where  $dE_g^o/dP$  is the unstrained energy bandgap change with respect to the unit pressure.

The effect of strain on the energy band structure results in the splitting of the heavy hole and light hole band at the valence band zone center [11] (i.e., the in-plane wavevector  $k_{||} = 0$ ), which is degenerate in the unstrained case. When tensile strain is applied between the

quantum well and the barrier layers [12, 13, 14] along the superlattice growth  $z$ -direction, the strain can push the light hole levels upwards and pull the heavy hole levels downwards. We can therefore expect that heavy hole and light hole states are inverted at specific lattice strains and quantum well thicknesses. This phenomena will in turn cause the intersubband transitions in a QWIP structure to take place from the populated light hole ground state to the upper energy band states. Since the light hole has a small effective mass (comparable to the electron effective mass), the optical absorption and spectral responsivity in p-type QWIPs can be greatly enhanced, as a result of introducing strain in the quantum well. In addition to the utilization of the light hole states for their small effective masses, etc., certain heavy hole states under compressional strain may also have similar characteristics, like high mobilities, small effective masses, and long mean free paths; which in turn favorably alter the intersubband absorption and transport characteristics, as shown by Hirose, *et al.* [31]. This is achieved by distorting the heavy hole valence band at and near the zone center via the introduction of compressional strain.

### 3.2.3 Energy Band Calculations

To calculate the locations of the energy subbands, we can use the transfer matrix method (TMM) [13, 15, 33], based on the eight-band  $\mathbf{k} \cdot \mathbf{p}$  model. This model is represented by the Luttinger-Kohn Hamiltonian [16, 17],  $H_t$ , which describes the unstrained semiconductor.

$$H_t = H + V(z) \quad (10)$$

where

$$H = \begin{bmatrix} H_{11} & H_{12} & H_{13} & H_{14} \\ H_{21} & H_{22} & H_{23} & H_{24} \\ H_{31} & H_{32} & H_{33} & H_{34} \\ H_{41} & H_{42} & H_{43} & H_{44} \end{bmatrix} \quad (11)$$

with:

$$\begin{aligned} H_{11} &= \frac{\gamma_1 + \gamma_2}{2} (k_x^2 + k_y^2) + \frac{\gamma_1 - \gamma_2}{2} k_z^2 \\ H_{22} &= \frac{\gamma_1 - \gamma_2}{2} (k_x^2 + k_y^2) + \frac{\gamma_1 + \gamma_2}{2} k_z^2 \\ H_{12} &= i\sqrt{3}\gamma_3 (k_x - ik_y)k_z \end{aligned}$$

$$\begin{aligned}
H_{13} &= \frac{\gamma_2\sqrt{3}}{2}(k_x^2 - k_y^2) - i\sqrt{3}\gamma_3 k_x k_y \\
H_{21} &= H_{12}^*, & H_{13} &= H_{31}^*, & H_{24} &= H_{13} \\
H_{34} &= H_{12}, & H_{42}^* &= H_{13}^*, & H_{43} &= H_{12}^* \\
H_{14} &= H_{23} = H_{32} = H_{41} = 0
\end{aligned}$$

and  $V(z)$  is a step function where  $V(z)$  vanishes inside the well layers and equals  $V_o$  in the barrier layers. The effect of strain is included by adding the Pikus-Bir Hamiltonian [18],  $H_s$ , to the general Luttinger-Kohn Hamiltonian. As shown below, the strain Hamiltonian for the well material is a diagonal matrix.

$$H_s = \begin{bmatrix} -\Delta E_c - \Delta E_{hh} & 0 & 0 & 0 \\ 0 & -\Delta E_c + \Delta E_{hh} & 0 & 0 \\ 0 & 0 & -\Delta E_c + \Delta E_{hh} & 0 \\ 0 & 0 & 0 & \Delta E_c + \Delta E_{hh} \end{bmatrix} \quad (12)$$

Using the aforementioned techniques, we can numerically calculate the energy of the zone-center valence subband levels as a function of well width for any material system under tensile or compressional strain and also determine the change in the valence subband structures.

All of the previously described calculations are derived from the multiband effective mass  $\mathbf{k} \cdot \mathbf{p}$  model for a coherently strained structure, which is based upon the perturbation approximation. In the  $\mathbf{k} \cdot \mathbf{p}$  model, the interactions of S-P type coupling among conduction (C), light-hole (LH), heavy-hole (HH), and spin-orbit (SO) states combined with spin-orbit like coupling are taking into consideration to derive the band structures. This results in an  $8 \times 8$   $\mathbf{k} \cdot \mathbf{p}$  Hamiltonian and momentum matrix elements. Using the perturbation approximation, a set of wave functions of  $S_{1/2}$ :  $|1/2, \pm 1/2\rangle_c$ ;  $P_{3/2}$ :  $|3/2, \pm 3/2\rangle$ ,  $|3/2, \pm 1/2\rangle$ ; and  $P_{1/2}$ :  $|1/2, \pm 1/2\rangle$  are used to represent the unperturbed and unstrained basis in the  $|J, m_j\rangle$  presentation [23].  $m_j = \pm 1/2$  represents either the electron or LH states, while  $m_j = \pm 3/2$  denotes the HH or heavy particle states. A slightly simplified  $6 \times 6$   $\mathbf{k} \cdot \mathbf{p}$  Hamiltonian can be used to roughly predict the P-like properties of the coherently strained layers by considering the S-like conduction band states as a perturbation, if a large enough bandgap exists, like in InGaAs and GaAs layers. The wave functions of the coherently strained superlattice

at the zone center ( $\mathbf{k}=0$ ) are given by [24]

$$|3/2, \pm 3/2 \rangle \quad HH \text{ states} \quad (13)$$

$$\gamma |3/2, \pm 1/2 \rangle + \beta |1/2, \pm 1/2 \rangle \quad LH \text{ states} \quad (14)$$

$$-\beta |3/2, \pm 1/2 \rangle + \gamma |1/2, \pm 1/2 \rangle \quad SO \text{ states} \quad (15)$$

where  $\gamma$  and  $\beta$  are constants which are dependent on the strain parameters. Note that the heavy-hole states,  $|3/2, \pm 3/2 \rangle$ , are still decoupled from the other valence band states even under biaxial stress at the zone center, while the light-hole and spin-orbit split off states are coupled at  $\mathbf{k}=0$ . However, the HH, LH, and SO states are mixed [25, 26] in the coherently strained superlattice at off zone center ( $\mathbf{k} \neq 0$ ). This mixing between the states with different  $m_j$ 's is due to the boundary conditions across the interface of the quantum well layers. By examining the  $\mathbf{k} \cdot \mathbf{p}$  matrix, we can see that the interaction between the different  $m_j$  states is proportional to the transverse components of the wave vector,  $k_{x,y}$ , so that the HH states are decoupled when  $k_{x,y}=0$ . It is interesting to note that the  $k_{x,y}$ 's are conserved across the interfaces since the interface potential depends only on  $z$ , the quantum well growth direction. Thus the band mixing can be significant if the  $\Gamma$ -bandgap is small, e.g., with GaAs and InGaAs, and if the LH and SO bands involved in the transition have a large  $k_z$  value [25].

Since the heavy hole and light hole valence subbands are non-degenerate following the introduction of strain into the QWIP structure, a simpler method can be used to determine the energies of the subbands. By using the parabolic band approximation near the valence band zone-center, and the energy band shifts for the conduction band minimum, heavy hole subband maximum, and light hole subband maximum, we can utilize the simpler two-band Hamiltonian for electrons just by finding the effective mass of the carriers (i.e., heavy-hole effective mass and light-hole effective mass) and the barrier heights for each carrier type. Although this does not simultaneously determine the energy levels of both carriers, it does allow accurate predictions of the energy subbands. When compared to the direct calculation of the energy subbands, the two-band approximation yields accurate results when compared to the direct calculation results [13, 18]. One limitation of the TMM is that this method cannot calculate the energy levels of the allowed energy subbands in the continuum states. In order to determine the transition energy from the ground state to the continuous state,

we used the Kronig-Penney model to determine the locations of the allowed energy bands in the continuum states.

When a biaxial internal tension is applied to the well material, the strain pulls the LH subbands up with respect to the HH subbands for a given well thickness. While quantum confinement effects tend to push the LH subbands down with respect to the HH subbands. As the well width is increased above a certain value, the strain effect can overcome the quantum confinement effect and therefore induce the inversion of the heavy hole and light hole subbands at the ground state. In contrast, with the application of compressional strain on the well layers, the strain forces the LH subbands down with respect to the HH subbands for a given well thickness.

### 3.2.4 The Transfer Matrix Method for the Calculation of Transmission Probability

The transfer matrix method (TMM) [33] allows the calculation of the transmission probability through a superlattice. Like any typical quantum mechanical barrier or well, the carrier conduction in each layer of the superlattice consists of the superposition of two components propagating forwards and backwards. The complete wave function can be expressed as

$$\psi_i = \psi_i^+ e^{+ik_i} e^{-\Delta_i} + \psi_i^- e^{-k_i} e^{+\Delta_i} \quad (16)$$

where

$$\begin{aligned} \Delta_1 &= \Delta_2 = 0 \\ \Delta_i &= k_i(d_2 + d_3 + \dots + d_i) \\ i &= 3, 4, \dots, N \\ k_i &= \left[ \frac{2m_i^*}{\hbar^2} (E - E_i) \right]^{1/2}, \end{aligned}$$

where  $\psi_i^+$  and  $\psi_i^-$  represent the magnitudes of the wave functions propagating in the forward, or  $+z$  direction and the backwards, or  $-z$  direction, respectively. While  $N$  is the number of periods in the superlattice,  $d_i$  is the thickness of the  $i$ -th layer in the superlattice,  $m_i^*$  is the effective mass of the particle in the  $i$ -th superlattice layer, and  $E_i$  is the potential energy of the  $i$ -th layer. Since the wave function,  $\psi$ , and its derivative,  $d\psi/dz$ , are continuous at the

boundaries, the wave functions then become

$$\psi_i^+ = (e^{-i\delta_i}\psi_{i+1}^+ + r_i e^{-i\delta_i}\psi_{i+1}^-)/t_i \quad (17)$$

$$\psi_i^- = (r_i e^{i\delta_i}\psi_{i+1}^+ + e^{i\delta_i}\psi_{i+1}^-)/t_i. \quad (18)$$

The recurrence relationship of the wave functions can be written in matrix form as

$$\begin{pmatrix} \psi_i^+ \\ \psi_i^- \end{pmatrix} = \frac{1}{t_i} \begin{pmatrix} e^{-i\delta_i} & r_i e^{-i\delta_i} \\ r_i e^{i\delta_i} & e^{i\delta_i} \end{pmatrix} \begin{pmatrix} \psi_{i+1}^+ \\ \psi_{i+1}^- \end{pmatrix}, \quad (19)$$

where at normal incidence

$$r_i = \frac{k_i - k_{i+1}}{k_i + k_{i+1}}, \quad (20)$$

$$t_i = \frac{2k_i}{k_i + k_{i+1}}, \quad (21)$$

and

$$\delta_i = k_i d_i. \quad (22)$$

Which gives us the following form for determining the  $N + 1$ -th wave functions

$$\begin{pmatrix} \psi_1^+ \\ \psi_1^- \end{pmatrix} = S_1 \begin{pmatrix} \psi_2^+ \\ \psi_2^- \end{pmatrix} = S_1 S_2 \begin{pmatrix} \psi_3^+ \\ \psi_3^- \end{pmatrix} = S_1 S_2 \cdots S_N \begin{pmatrix} \psi_{N+1}^+ \\ \psi_{N+1}^- \end{pmatrix}, \quad (23)$$

where

$$S_i = \frac{1}{t_i} \begin{pmatrix} e^{-i\delta_i} & r_i e^{-i\delta_i} \\ r_i e^{i\delta_i} & e^{i\delta_i} \end{pmatrix}. \quad (24)$$

Since there is no backwards, or in the  $-z$  direction, propagation in the  $N + 1$ -th layer, the magnitude of the wave function  $\psi_{N+1}^- = 0$ . Thus we can find the  $\psi_i^+$  term of  $E_1^+$ , in the  $i$ -th layer ( $i = 2, 3, 4, \dots, N + 1$ ).

If we determine the quantity,  $\psi_i^+/\psi_1^+$ , as a function of  $E_1$ , then we will know the locations of the resonant peaks. The transmission probability can be expressed as

$$|T \cdot T| = \left| \frac{\psi_i^+}{\psi_1^+} \right|^2. \quad (25)$$

### 3.2.5 Determination of Intersubband Transitions and Absorption Coefficients

In addition to the energy level and energy band locations, the calculation of intersubband and interband transitions are also of great interest. In order to determine the intersubband and interband transitions in a p-type strained layer QWIP, the usage of the 6×6 Hamiltonian which includes the previously mentioned  $\mathbf{k} \cdot \mathbf{p}$  Hamiltonian [16, 17, 24] and the strain Hamiltonian [18]. Since the strain and the spin-orbit coupling terms do not lift the spin degeneracy, the 6×6 Hamiltonian matrix can then be factorized into two 3×3 irreducible matrices. The assumption that the Fermi distribution function is equal to one for the confined ground state and equal to zero for the excited states in equilibrium is used to simplify the calculation without loss of accuracy. The absorption coefficient for the intersubband or interband transition between the initial ground state,  $i$ , and the final continuum state,  $f$ , is given by [27]

$$\alpha_i(\omega) = \sum_f \frac{4\pi^2 e^2}{n_r c m_o^2 \omega} \int_{BZ} \frac{2d\mathbf{k}}{(2\pi)^3} \left[ (f_i - f_f) |\hat{\mathbf{e}} \cdot \mathbf{P}_{i,f}|^2 \frac{\Gamma/2\pi}{[\Delta_{i,f}(\mathbf{k}) - \hbar\omega]^2 + (\Gamma^2/4)} \right] \quad (26)$$

where  $n_r$  is the refractive index in the quantum well,  $m_o$  is the free electron mass,  $\Delta_{i,f}$  is the energy difference between the initial ground state,  $i$ , of energy  $E_i(\mathbf{k})$  and the final state,  $f$ , with the corresponding energy of  $E_f(\mathbf{k})$ .  $\hat{\mathbf{e}}$  and  $\omega$  are the unit polarization vector and the frequency of the incident IR radiation, respectively,  $f_i$  and  $f_f$  are the Fermi distribution functions of the initial and final states, and  $\Gamma$  is the full width of level broadening.  $\Gamma \sim \hbar/\tau_{if}$ , where  $\tau_{if}$  is the lifetime between the initial,  $i$ , and final,  $f$ , states.  $|\hat{\mathbf{e}} \cdot \mathbf{P}_{i,f}|$  are the optical transition elements between the quantum well valence subband ground states,  $i$ , and the continuum subband states,  $f$ , in the HH, LH, and SO bands; which can be derived from the two 3×3  $\mathbf{k} \cdot \mathbf{p}$  matrix elements as shown below.

Using the following 3×3 optical matrix,

$$\frac{m_o}{\hbar} \begin{bmatrix} T_{HH} & T_{HL} & T_{HS} \\ T_{LH} & T_{LL} & T_{LS} \\ T_{SH} & T_{SL} & T_{SS} \end{bmatrix}, \quad (27)$$

the optical matrix elements,  $|\hat{\mathbf{e}} \cdot \mathbf{P}_{i,f}|$ , can be obtained. These matrix elements have the same form as the  $\mathbf{k} \cdot \mathbf{p}$  matrix elements except that the  $k_i k_j$ 's are replaced with  $k_i \epsilon_j + k_j \epsilon_i$  multiplied by a constant factor of  $m_o/\hbar$  [27]. The  $T_{ij}$ 's are defined as follows:

$$T_{HH} = 2(A - B)\epsilon_z k_z + (2A + B)(\epsilon_x k_x + \epsilon_y k_y), \quad (28)$$



$$T_{LL} = 2(A + B)\epsilon_z k_z + (2A - B)(\epsilon_x k_x + \epsilon_y k_y), \quad (29)$$

$$T_{SS} = 2A(\epsilon_x k_x + \epsilon_y k_y + \epsilon_z k_z) \quad (30)$$

$$\begin{aligned} T_{HL} = & i\frac{1}{\sqrt{3}}N(\epsilon_x \cos \eta - \epsilon_y \sin \eta)k_z - i\frac{1}{3}N\epsilon_z k_{\parallel} \\ & - \sqrt{3}B(\epsilon_x k_x - \epsilon_y k_y) \cos \chi \\ & + \frac{1}{\sqrt{3}}N(\epsilon_x k_y + \epsilon_y k_x) \sin \chi, \end{aligned} \quad (31)$$

$$\begin{aligned} T_{HS} = & \frac{1}{\sqrt{6}}N(\epsilon_x \cos \eta + \epsilon_y \sin \eta)k_z + \frac{1}{6}N\epsilon_z k_{\parallel} \\ & + i\sqrt{6}B(\epsilon_x k_x - \epsilon_y k_y) \cos \chi \\ & - \frac{2}{\sqrt{6}}N(\epsilon_x k_y + \epsilon_y k_x) \sin \chi, \end{aligned} \quad (32)$$

$$\begin{aligned} T_{LS} = & \left[ i2\sqrt{2}B\epsilon_z + \frac{1}{\sqrt{2}}N\epsilon_x \cos(\chi - \eta) - \epsilon_y \sin(\chi - \eta) \right] k_z \\ & - i\sqrt{2}B(\epsilon_x k_x + \epsilon_y k_y) \\ & - \frac{1}{\sqrt{2}}N\epsilon_z k_{\parallel} \cos(\chi - 2\eta), \end{aligned} \quad (33)$$

$$T_{SH} = T_{HS}^*, \quad (34)$$

$$T_{SL} = T_{LS}^*, \quad (35)$$

$$T_{LH}^* = T_{HL}. \quad (36)$$

Here  $A, B, N, \chi, \eta$  are inverse mass band parameters [27].

### 3.2.6 Photoconductive Detection Mode Operation

When IR radiation impinges on a photoconductor, the photoconductive material undergoes a physical change characterized by a change in resistance,  $\Delta R_d$ . This change in resistance is due to the photo-excitation of carriers, forming mobile excess carriers in the photoconductor. The excess photogenerated carriers,  $\Delta n$ , can be expressed as

$$\Delta n = \frac{\eta \Delta \Phi \tau_L}{V_d} \quad (37)$$

where,  $\eta$ , is the quantum efficiency,  $\Delta \Phi$  is the incident photon flux,  $\tau_L$  is the excess carrier lifetime, and  $V_d$  is the volume of the detector. These photogenerated carriers are transported out of the detector under the influence of the applied external bias, which results in a photovoltage signal. The change in the output photovoltage,  $\Delta V_o$ , due to the resistance

change is given by

$$\Delta V_o = -\frac{V_a R_L \Delta R_d}{(R_L + R_d)^2}, \quad (38)$$

where  $R_L$  is the load resistance and its value is typically chosen to be about equal to  $R_d$ , the detector resistance, to match loads and to optimize the output signal.

### 3.3 P-QWIP Figures of Merit

Although our band structure and absorption calculations can be used to determine the positions of the subbands in the quantum wells, and hence determine the peak absorption wavelength of the QWIP, many other factors must be taken into account to design a QWIP with the correct detection peak. Generally, for a high-performance QWIP, the responsivity must be high, while the noise current, and hence the dark current, must be low.

#### 3.3.1 Spectral Responsivity

The responsivity,  $R$ , for a photodetector may be expressed as [19]

$$R = \frac{q\lambda\eta}{hc} G = \frac{q}{h\nu} \eta_c, \quad (39)$$

where  $q$  is the electronic charge,  $\lambda$  is the wavelength of the incident photon,  $h$  is the Planck constant,  $c$  is the speed of light,  $\eta$  is the quantum efficiency,  $\eta_c$  is the collection efficiency,  $\nu$  is the incident frequency, and the photoconductive gain is  $G$ . The quantum efficiency and photoconductive gain are described, respectively, by [19]

$$\eta = A(1 - R)[1 - \exp(-B\alpha l_{qw})] \quad (40)$$

$$G = \frac{L}{t_c} \quad (41)$$

where  $A$  is a constant that is polarization dependent,  $\alpha$  is the absorption coefficient of the quantum well,  $l_{qw}$  is the total width of all quantum well regions,  $L$  is the mean free path of the carrier,  $R$  is the reflection coefficient, and  $t_c$  is the total width of all quantum well and barrier regions.  $B$  is a constant dependent on the number of passes IR radiation makes through the photodetector. For n-type QWIPs,  $A=0.5$ , while for p-type QWIPs  $A=1$ . The mean free path of the carrier may be expressed as [19]

$$L = \tau T_{qw} \mu_{eff} \mathcal{E}, \quad (42)$$

where  $\tau$  is the well recapture lifetime of the carrier,  $T_{qw}$  is the transmission coefficient over the quantum well,  $\mu_{eff}$  is the effective mobility of the carrier, and  $\mathcal{E}$  is the electric field. The effective mobility for a two-band transport model is shown to be [19]

$$\mu_{eff} = \frac{\Delta p_{lh}\mu_{lh} + \Delta p_{hh}\mu_{hh}}{\Delta p_{lh} + \Delta p_{hh}}, \quad (43)$$

where  $\Delta p_{hh}$  and  $\Delta p_{lh}$  are the concentrations of optically induced heavy- and light- hole carriers, respectively, and  $\mu_{hh}$  and  $\mu_{lh}$  are the respective heavy and light hole mobilities. When only the ground state is completely occupied, either  $\Delta p_{lh}$  or  $\Delta p_{hh}$ , the optically induced light holes or the optically induced heavy holes dominate, so that we may estimate  $\mu_{eff}$  as the in-plane effective mass of the ground state carriers.

### 3.3.2 QWIP Collection Efficiency

A figure of merit that can be easily quantified by simple measurements is the collection efficiency,  $\eta_c$ . The collection efficiency describes the ease in which the energy from the incident photon flux is converted into mobile carriers which are swept out of the QWIP by the applied bias and collected; and is defined as the product of the quantum efficiency,  $\eta$ , and the photoconductive gain,  $G$ .

$$\eta_c = \eta G \quad (44)$$

In addition to being expressed as the mean free path over the total width of the quantum wells and barriers,  $G$  can be viewed as the ratio of the carrier transport lifetime,  $\tau_L$ , to the transit time,  $\tau_T$ , through the QWIP. Empirically, the photoconductive gain can be described in terms of the capture or trapping probability,  $p_c$  [34, 35, 36],

$$G = \frac{1}{Np_c(1 + p_c)}, \quad (45)$$

and  $N$  is the number of wells. If  $p_c$  is small, then  $G$  can be approximated as,  $G \simeq 1/Np_c$ .

Physically, the trapping probability is defined as the ratio of the escape time from the well region to the lifetime of the excited carriers from the confined ground state. If the excited states are in resonance with the top of the barrier potential energy, then the escape time will be greatly reduced, which theoretically minimizes the trapping probability and maximizes the photoconductive gain. Therefore in all of our designs, we attempted to make

the energy of the upper excited peak for the main detective peak in resonance with the top of the barrier potential energy.

If  $B\alpha l_{qw} \ll 1$  and  $p_c \ll 1$ , an approximate expression for  $\eta_c$  can be written as

$$\eta_c = A(1-R)[1 - \exp(-B\alpha l_{qw})] \frac{1-p_c}{Np_c} \quad (46)$$

$$\approx A(1-R) \frac{B\alpha l_{qw}}{Np_c}. \quad (47)$$

where  $B$  is a constant dependent on the number of passes the IR radiation makes through the photodetector,  $A$  is a polarization dependent variable equal to 0.5 for n-type QWIPs and 1 for p-QWIPs,  $R$  is the reflection coefficient,  $l_{qw}$  is the total width of all quantum well regions, and  $\alpha$  is the absorption coefficient.

### 3.3.3 Dark Current Relationship in a QWIP

Another important parameter to be considered in a QWIP design is the dark current density ( $J_d$ ), which can be expressed using the Richardson-Dushman equation [14] as

$$J_d \propto T^2 m^* \exp\left(\frac{-\Delta E}{k_B T}\right), \quad (48)$$

where  $m^*$  is the effective mass,  $\Delta E$  is the difference in energy between the barrier height and the quantum confined state in the well,  $k_B$  is the Boltzmann constant, and  $T$  is the temperature. This type of expression assumes that the dominant source of dark current is thermionic emission over the quantum well barrier.

In the low-field regime, the thermionic emission current is related to the density of mobile carriers,  $n_t$  and the average drift velocity,  $v_d$ , and can be expressed as [37]

$$I_{th} = eA_d v_d n_t, \quad (49)$$

where  $A_d$  is the active detector area,  $e$  is the electronic charge, and

$$v_d = \frac{\mu \varepsilon}{[1 + (\mu \varepsilon / v_s)^2]^{1/2}}, \quad (50)$$

$$n_t = (m^* k_B T / \pi \hbar^2 L) \exp[-(E_{cf} - E_F) / k_B T]. \quad (51)$$

In the above equations,  $\mu$  is the mobility,  $\varepsilon$  is the electric field,  $v_s$  is the saturation velocity,  $E_{cf}$  is the cut-off energy related to the cut-off wavelength  $\lambda_c$ , and  $m^* / \pi \hbar^2$  is the two-dimensional density of states. The Fermi energy,  $E_F$ , can be obtained from the expression

of  $N_D$ :

$$N_D = \frac{m^* k_B T}{\pi \hbar^2 L} \sum_n \ln \left[ 1 + \exp \left( \frac{E_F - E_n}{k_B T} \right) \right] \quad (52)$$

$$\approx \frac{m^*}{\pi \hbar^2 L} \sum_n (E_F - E_n). \quad (53)$$

Equation (52) for  $N_D$  is valid when summed over the subband levels  $E_n$  below the Fermi level, and Eq. (53) is only valid at cryogenic temperatures.

Using the previous result in the cryogenic temperature regime, we see that the dark current due to thermionic emission is exponentially dependent on the doping concentration in the quantum well, i.e.,

$$I_{th} \propto \exp\left(\frac{E_F}{k_B T}\right) \propto \exp\left(\frac{N_D}{k_B T}\right). \quad (54)$$

Therefore, as the doping density in the quantum well increases, the dark current density due to thermionic emission also increases exponentially. In contrast to this, the intersubband absorption is directly proportional to the doping concentration. Therefore, a tradeoff between the dark current density and the intersubband absorption is required to optimize the QWIP performance. However, in the case of p-QWIPs, the Fermi level in the quantum well is pinned at or slightly above the ground state energy for highly doped quantum wells. We can increase the doping in the quantum well to increase optical absorption without increasing the dark current of the p-QWIP significantly because the thermionic emission is pinned with the Fermi level.

### 3.3.4 Noise in QWIPs

The noise in QWIP structures is mainly due to random fluctuations of thermally excited carriers. The noise is expressed as [5]

$$i_{noise} = \sqrt{4 A_d q G \Delta f J_d}, \quad (55)$$

where  $A_d$  is the detector area, and  $\Delta f$  is the bandwidth. Finally, a figure of merit measurement used to compare detectors is the detectivity,  $D^*$ , which is shown to be [19]

$$D^* = \sqrt{A_d \Delta f} \frac{R}{i_{noise}}. \quad (56)$$

If the dark current in a particular QWIP is lower than the 300 K background photocurrent, then the QWIP can be considered to be under background limited performance (BLIP). In a BLIP QWIP, the dominant current is due to photon noise, since all the other sources are negligible by comparison. The photon noise is calculated from the arrival statistics of the incoherent photons. The background photon noise current,  $i_{np}$ , is given by [20, 21]

$$i_{np}^2 = 4Aq^2\eta g^2 P_b B_f / (h\nu), \quad (57)$$

where  $P_b$  is the incident background optical power,  $B_f$  is the QWIP bandwidth,  $\eta$  is the absorption quantum efficiency,  $\nu$  is the incident photon frequency, and  $g$  is the noise current gain. The photocurrent,  $I_p$  can be approximated by

$$I_p = A(q/h\nu)\eta g P_s, \quad (58)$$

where  $P_s$  is the incident optical signal power. The constant,  $A$ , in Eqs. (46), (47), (57), and (58), is due to the polarization selectivity for n-type QWIPs versus p-type QWIPs. As previously stated, for n-type QWIPs,  $A = 0.5$ , while  $A = 1$  for p-type QWIPs. By setting the signal-to-noise power ratio equal to unity, the background limited noise equivalent power,  $(NEP)_{BLIP}$  and the detectivity,  $D_{BLIP}^*$ , for n-type QWIPs can be expressed as

$$(NEP)_{BLIP} = 2\sqrt{2h\nu B P_b / \eta}. \quad (59)$$

$$D_{BLIP}^* = \sqrt{A_d B} / (NEP)_{BLIP} = \frac{\lambda_p}{2\sqrt{2}hc} \left( \frac{\eta}{Q_b} \right)^{1/2}, \quad (60)$$

where  $A_d$  is the active area of the detector, and  $Q_b = P_b / (A h \nu)$  is the incident photon flux from the background for a given spectral bandwidth,  $\Delta\nu$ , and a peak wavelength,  $\lambda_p$ .  $Q_b$  is defined as

$$Q_b = \frac{2\pi}{c^2} \frac{\nu^2 \Delta\nu}{e^{h\nu/k_B T} - 1} \sin^2 \left( \frac{\theta}{2} \right), \quad (61)$$

where,  $\theta$ , is the field of view (FOV). For a p-type QWIP, a factor of  $\sqrt{2}$  is used in the denominator of Eq. (60),  $D_{BLIP}^*$ , since it can absorb both optical polarizations of the incident IR radiation.

## 4 TECHNICAL RESULTS

### 4.1 An $\text{In}_{0.3}\text{Ga}_{0.7}\text{As}/\text{In}_{0.52}\text{Al}_{0.48}\text{As}$ on InP P-QWIP with Tensile Strain

As can be seen in figures 1(b) and 1(c), we can utilize the strain inherent in a lattice mismatched system in addition to the engineering of the well thicknesses and barrier layers to modify the energy band structure of the p-type QWIPs. The strained-layer  $\text{In}_{0.3}\text{Ga}_{0.7}\text{As}/\text{In}_{0.52}\text{Al}_{0.48}\text{As}$  P-QWIP as shown in figure 1(a), uses a light hole ground state to heavy hole continuum state intersubband transition for IR detection. The QWIP structure was grown on a (100) semi-insulating (SI) InP substrate via molecular beam epitaxy (MBE). Beryllium was used as the p-type dopant and the structure consists of 20 periods of 40 Å thick  $\text{In}_{0.3}\text{Ga}_{0.7}\text{As}$  quantum wells with a dopant density of  $1 \times 10^{18} \text{ cm}^{-3}$  separated by 450 Å thick barrier layers of undoped  $\text{In}_{0.52}\text{Al}_{0.48}\text{As}$  barrier layers. A 0.3 μm thick cap layer and a 1 μm thick buffer layer of lattice-matched  $\text{In}_{0.53}\text{Ga}_{0.47}\text{As}$  were grown with a dopant density of  $2 \times 10^{18} \text{ cm}^{-3}$  to serve as ohmic contacts. The contact and barrier layers were designed to be lattice matched with the InP substrate. The quantum wells are in biaxial tension with a lattice mismatch of 1.6% between the well layers and the substrate. A 200 μm by 200 μm mesa was then created by chemical etching to facilitate the measurement of spectral responsivity and dark current of the QWIP. Since the dopant density in the ohmic contact cap and buffer regions were slightly less than that required for using Au/Cr contacts, an Au/Zn alloy was used to make ohmic contacts to the p-type QWIP. The ohmic contacts were thermally evaporated onto the QWIP mesas to a thickness of approximately 1200 Å. The QWIPs were annealed at 480 °C for two minutes to obtain stable and low contact resistances.

Figure 2(b) shows the measured dark current density from 77 K to 110 K with a 300 K background photocurrent superimposed. The asymmetric dark current characteristic in this p-type QWIP was observed due to the band bending in the barrier layers as shown in Fig. 1(a). Due to the extremely low dark current density of this QWIP, it is under background limited performance (BLIP) for a field of view (FOV) of 90° at a temperature less than 90 K under applied biases from -2.5 V to +5 V and higher. In the forward biased regime, the QWIP is under BLIP operation up to 100 K with an applied bias of +2.5 V. Figure 2(a) shows the calculated absorption coefficient at normal incidence for a SL P-QWIP with a 6

nm well thickness versus that of an unstrained P-QWIP.

The responsivity of the QWIP can be measured as a function of temperature, applied bias, and incident radiation wavelength. Using a globar and an automatic PC-controlled single grating monochromator, under normal incidence infrared (IR) radiation, we can measure the photocurrent versus radiation wavelength for both positive and negative biases; which are shown in figures 3(a) and 3(b), respectively. A peak wavelength at  $\lambda_p=8.1 \mu\text{m}$  was observed in the LWIR detection band, which is attributed to the intersubband transition between the confined ground light hole state,  $E_{LH1}$ , and the continuum heavy hole states,  $E_{HH3}$ . The cutoff wavelength was found to be  $8.8 \mu\text{m}$  which corresponds to a spectral bandwidth of  $\Delta\lambda/\lambda_p = 12\%$ . The responsivities for the p-type QWIP were calibrated using a standard pyroelectric detector and lock-in amplifier. Asymmetric responsivities of 34 mA/W and 51 mA/W at +4 V and -4 V bias, respectively, were measured. The maximum BLIP detectivity,  $D_{BLIP}^*$ , at  $\lambda_p=8.1 \mu\text{m}$  was determined to be  $5.9 \times 10^{10} \text{ cm-Hz}^{1/2}/\text{W}$  with a responsivity,  $R$  of 18 mA/W at +2 V bias with a FOV =  $90^\circ$  at 77 K. The quantum efficiency for the p-type QWIP was estimated from the responsivity measurements using a conservative photoconductive gain estimate of  $g=0.015$ . The %BLIP can be evaluated as follows when the Johnson noise and readout noise are ignored; with  $i_{np}$  and  $i_{nd}$  are the 300 K background photocurrent noise and dark current noise, respectively.

$$\%BLIP \approx \frac{i_{np}}{(i_{np}^2 + i_{nd}^2)^{1/2}} \quad (62)$$

Using the above expression, a nearly full BLIP detection was achieved at biases with magnitudes less than 2 V, as seen in figure 4. Due to the BLIP detection, the noise equivalent temperature difference (NE $\Delta$ T) is expected to be improved significantly for this QWIP.

The temperature dependence of the responsivity and detectivity was also explored for this  $\text{In}_{0.3}\text{Ga}_{0.7}\text{As}/\text{In}_{0.52}\text{Al}_{0.48}\text{As}$  SL P-QWIP. Due to the non-uniformities across the QWIP wafer, the peak responsivities and detectivities varied from device to device. As illustrated by figure 5, the responsivity increases with increased applied bias at each temperature. For applied biases above 3 V at 100 K, the sudden drop in responsivity can be attributed to the onset of non-BLIP operation, as also indicated in figure 2(b). The calculated detectivity at 2 V and 4 V of applied bias for this device at temperatures ranging from 77 K to 100 K is presented in table 1. As expected, the detectivity decreases as the temperature increases



above 77 K, since the inherent dark current density is rapidly increasing with the increasing ambient temperature and larger applied bias.

Temperature (K)	Bias (V)	Responsivity (mA/W)	Detectivity ( $\frac{cm\sqrt{Hz}}{W}$ )
77	4	12.10	$3.92 \times 10^{10}$
	2	5.30	$8.10 \times 10^{10}$
90	4	11.71	$3.29 \times 10^{10}$
	2	5.34	$7.60 \times 10^{10}$
100	4	13.04	$1.88 \times 10^{10}$
	2	5.69	$3.69 \times 10^{10}$

Table 1. Measured responsivities and detectivities as a function of applied bias and device temperature at  $\lambda_p=8.1 \mu m$ .

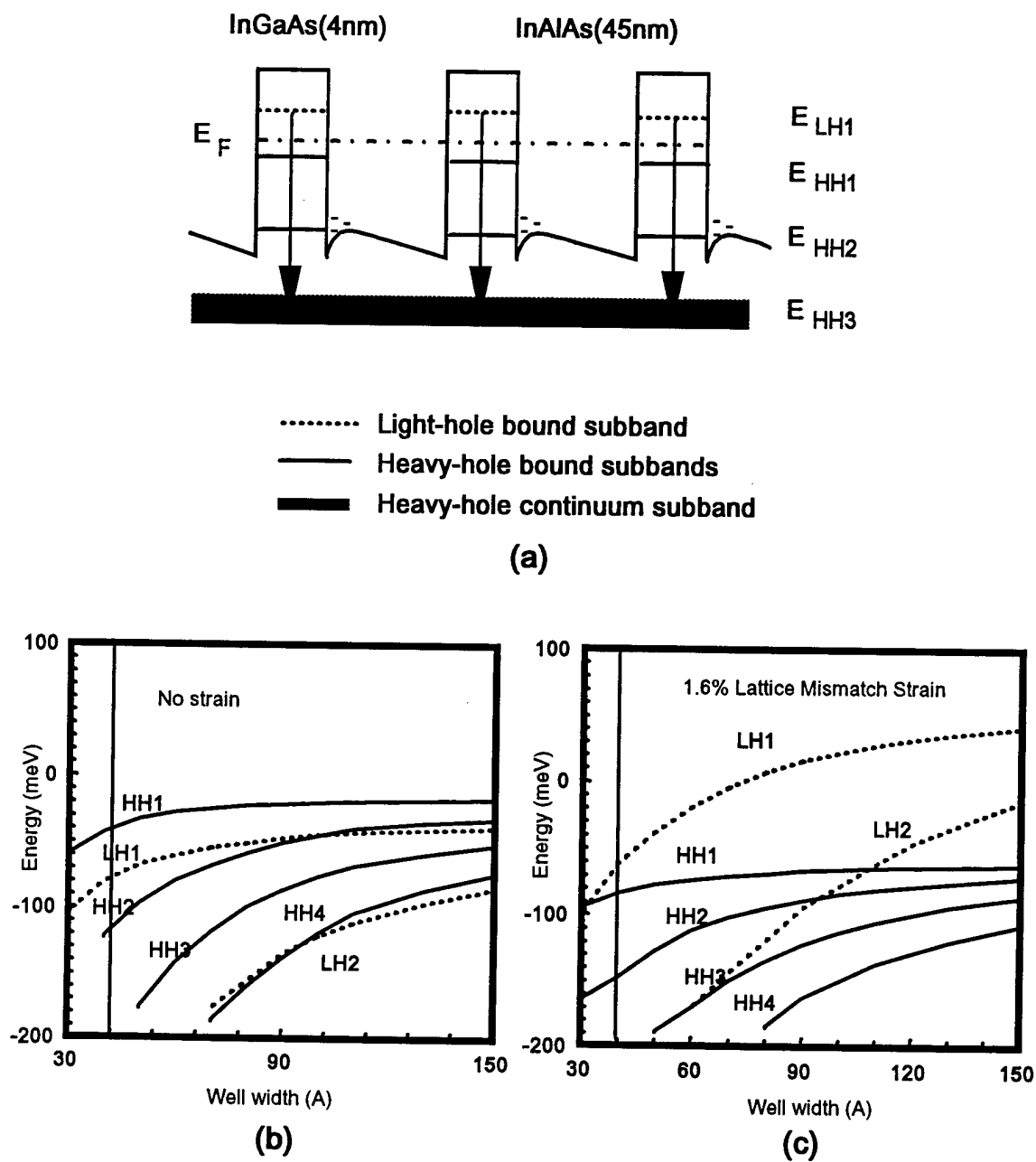


Figure 1: (a) Schematic energy band diagram for the tensile strain P-QWIP and the calculated energy levels in the quantum well for the P-QWIP (b) without and (c) with 1.6% tensile strain.

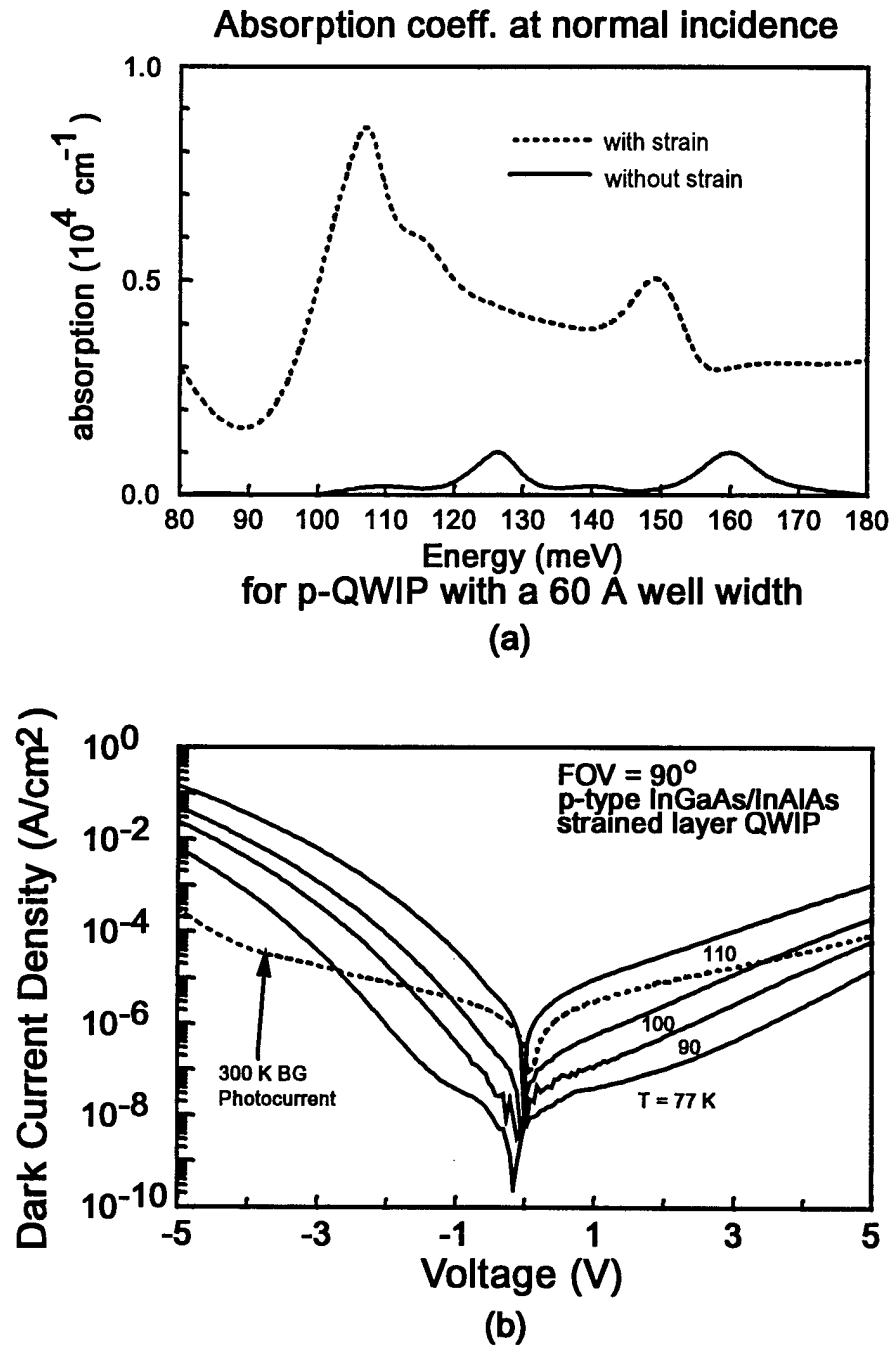
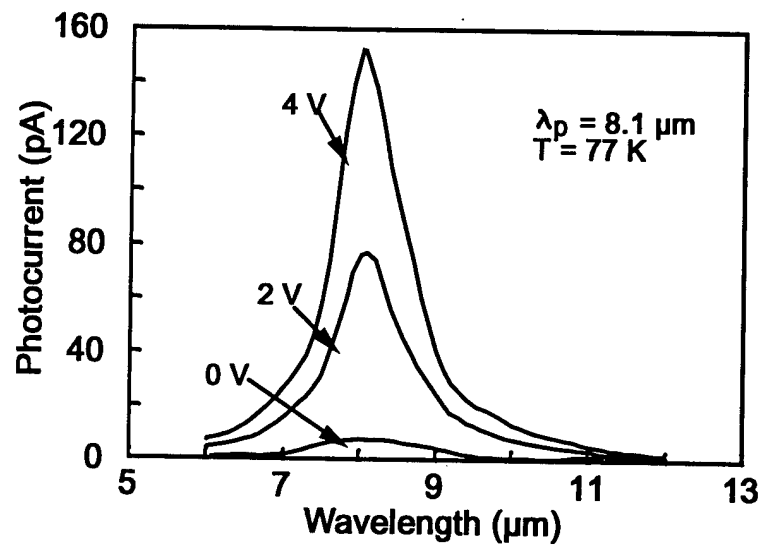
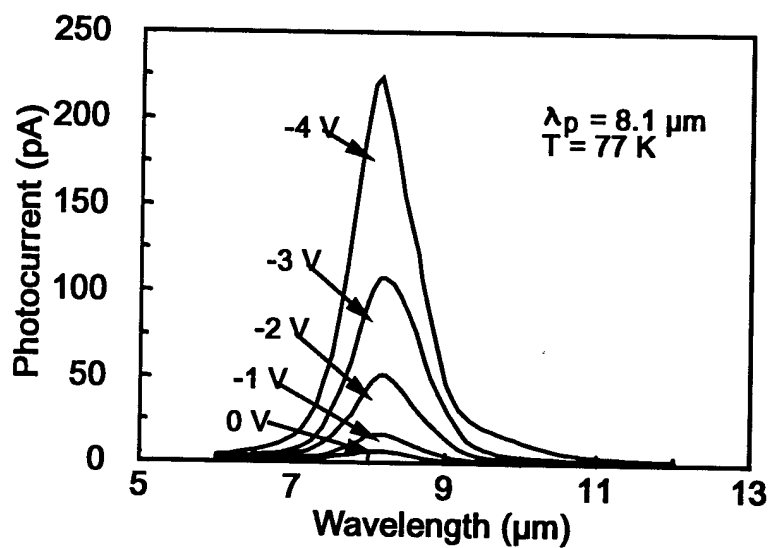


Figure 2: (a) Calculated absorption coefficient at normal incidence for a P-QWIP both with and without strain, and (b) measured dark current density and 300 K background photocurrent density.



(a)



(b)

Figure 3: Measured P-QWIP photoresponse at  $T = 77\text{ K}$  for (a) forward bias and (b) reverse bias.

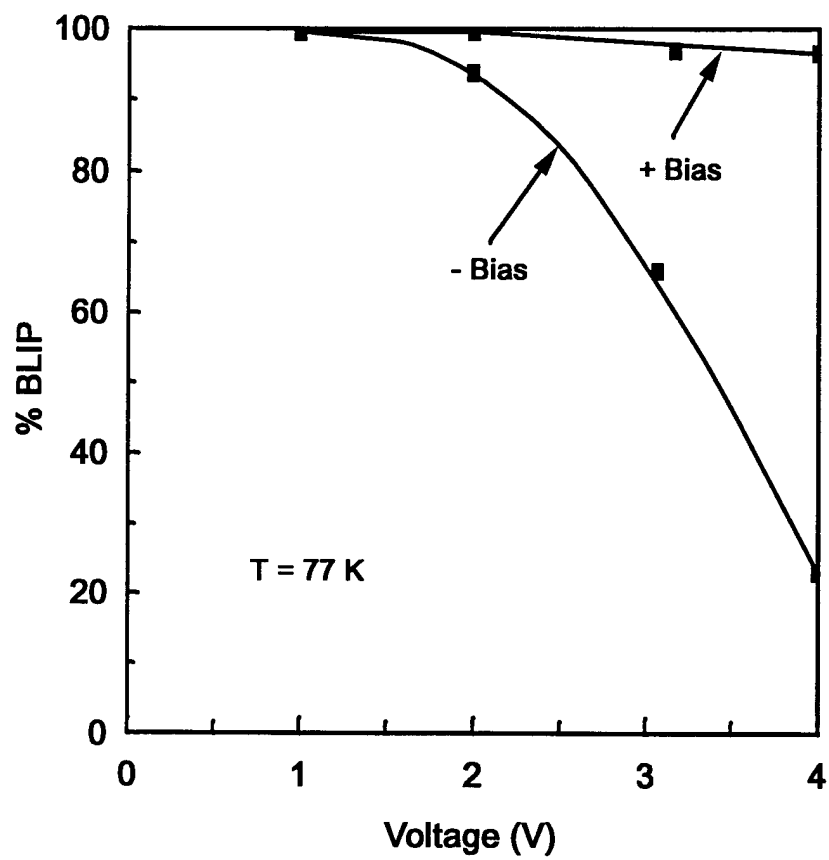


Figure 4: % BLIP for the strained-layer P-QWIP as a function of applied bias.

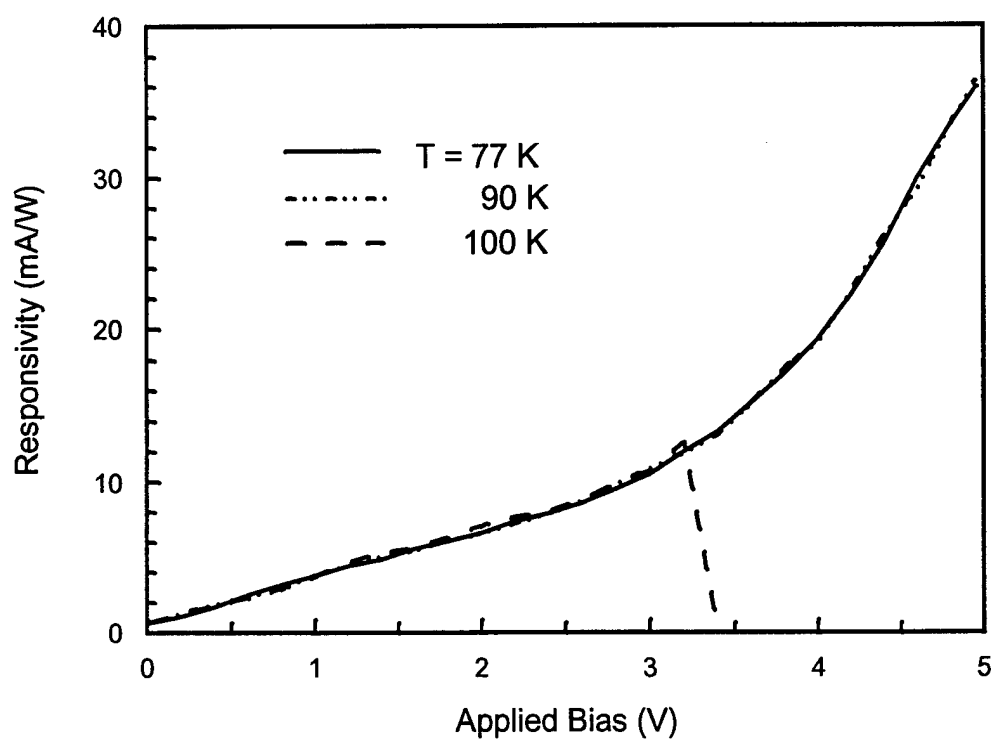


Figure 5: Responsivity as a function of bias and device temperature.

## 4.2 An $\text{In}_{0.4}\text{Ga}_{0.6}\text{As}/\text{GaAs}$ on $\text{GaAs}$ P-QWIP with compressional strain

Unlike the  $\text{In}_{0.3}\text{Ga}_{0.7}\text{As}/\text{In}_{0.52}\text{Al}_{0.48}\text{As}$  on  $\text{InP}$  P-QWIP with tensile strain between the layers; a normal incidence  $\text{In}_{0.4}\text{Ga}_{0.6}\text{As}/\text{GaAs}$  on  $\text{GaAs}$  P-QWIP was designed for two color detection in the 3-5  $\mu\text{m}$  MWIR and 8-14  $\mu\text{m}$  LWIR bands. With this device, we have demonstrated two color detection in p-type strained-layer QWIPs for the first time.

The p-type compressively strained  $\text{In}_{0.4}\text{Ga}_{0.6}\text{As}/\text{GaAs}$  QWIP was grown on a semi-insulating (SI)  $\text{GaAs}$  substrate via molecular beam epitaxy (MBE). This QWIP structure consists of 20 periods of 40  $\text{\AA}$   $\text{In}_{0.4}\text{Ga}_{0.6}\text{As}$  quantum well Be-doped to a density of  $4 \times 10^{18} \text{ cm}^{-3}$  separated by a 350  $\text{\AA}$  wide barrier layer of undoped  $\text{GaAs}$ . A 0.3  $\mu\text{m}$  cap layer and a 1.0  $\mu\text{m}$  buffer layer of Be-doped  $\text{GaAs}$  with a dopant density of  $5 \times 10^{18} \text{ cm}^{-3}$  were grown to serve as top and bottom ohmic contacts. The contact and barrier layers are lattice matched with the SI  $\text{GaAs}$  substrate, while the  $\text{In}_{0.4}\text{Ga}_{0.6}\text{As}$  quantum well layers are under biaxial compression with a designed lattice mismatch of approximately 2.8%. Due to the heavily doped large-bandgap contact layers of this P-QWIP, a large tunneling current from the triangle potential near the ohmic contact region may be dominant with respect to the QWIP's dark current. Therefore a relatively thick (550  $\text{\AA}$ ) undoped  $\text{GaAs}$  barrier layer was grown next to the top and bottom contact layers to reduce this dark current component.

To facilitate the characterization of this P-QWIP, a  $200 \times 200 \mu\text{m}^2$  mesa structure was created by wet chemical etching. An  $\text{Au}/\text{Cr}$  film was deposited onto the QWIP mesas and the buffer layer via e-beam deposition with a thickness of approximately 1500  $\text{\AA}$  for ohmic contacts. The semi-insulating  $\text{GaAs}$  substrate was thinned down to approximately 50  $\mu\text{m}$  to lower the substrate absorption screening effect, and polished to a mirror-like surface to reduce the reflection of the normal incidence IR radiation.

Figures 6(a) and 6(b) show the idealized energy band diagram and energy subband states for the compressively strained P-QWIP. In this case, the intersubband transitions are from the highly populated heavy hole ground state ( $E_{HH1}$ ) to the upper heavy hole continuum states ( $E_{HH3}$  and  $E_{HH4}$ ) for the 8.9  $\mu\text{m}$  LWIR detection peak and the 5.5  $\mu\text{m}$  MWIR detection peak, respectively.

The mobility of the heavy-hole is enhanced by the compressive strain in the  $\text{In}_{0.4}\text{Ga}_{0.6}\text{As}$  quantum well due to the reduction of heavy hole effective mass by a factor of three<sup>31</sup>. Another



effect attributed to the compressional strain localized in the quantum well is the decrease of the density of states in the well. This causes more heavy holes to reside in higher energy states, which effectively raises the Fermi level when compared with the same unstrained quantum well. The raised Fermi level will cause an increase in the number of off-center (i.e.,  $k \neq 0$ ) free heavy holes with lighter effective mass; which in turn causes a larger intersubband absorption when exposed to normal incidence IR radiation. Our InGaAs/GaAs compressional strain P-QWIP has its heavy holes in type-I band alignment, while the light holes are in the type-II band configuration. The binary GaAs layer used as the barrier layer should also exhibit superior current transport characteristics when compared to a ternary barrier. Finally, the heavy hole excited continuum states are resonantly lined up with the light hole states; which gives rise to a strong quantum coupling effect. This resonant lined up effect makes the conducting holes behave like light holes. These resonant heavy holes exhibit high mobilities, small effective masses, and long mean free paths. Therefore, larger photoconductive gain and higher photoconductivity are expected for a compressively strained P-QWIP when compared with an unstrained one.

When compared with the  $\text{In}_{0.3}\text{Ga}_{0.7}\text{As}/\text{In}_{0.52}\text{Al}_{0.48}\text{As}$  tensile strain P-QWIP and the new InGaAs/AlGaAs compressive strain P-QWIP, the measured dark current at various temperatures is much higher. This device also exhibits an asymmetrical dark current characteristic (figure 10), like the InGaAs/InAlAs tensile strain P-QWIP, which can be attributed to the dopant migration effect which occurs during layer growth<sup>32</sup>. For a field of view (FOV) of  $90^\circ$  the InGaAs/GaAs compressional strain P-QWIP is under background limited performance (BLIP) at  $V_b = 0.3$  V,  $T = 70$  K and  $V_b = 0.7$  V,  $T = 55$  K.

The responsivity of this QWIP was measured under normal incidence illumination as a function of temperature, applied bias, and incident IR wavelength using a blackbody radiation source and automatic PC-controlled single grating monochromator system. Twin LWIR peaks were detected at  $\lambda_{p1} = 8.9 \mu\text{m}$  and  $\lambda_{p2} = 8.4 \mu\text{m}$  as shown in figure 7(a). A single MWIR peak was discovered at  $\lambda_{p3} = 5.5 \mu\text{m}$  as seen in figure 7(b). At each peak wavelength, responsivities were measured as 24 mA/W at  $V_b = 0.3$  V and 45 mA/W at  $V_b = 0.7$  V for  $T \leq 75$  K. The twin LWIR peaks covered a broad wavelength band ranging from 6.5 to  $12 \mu\text{m}$ . The cut-off wavelength for the LWIR band was found to be  $\lambda_c \approx 10 \mu\text{m}$ , which corresponds to a spectral bandwidth of  $\Delta\lambda/\lambda_p = 35\%$ . The twin peak wavelengths are

attributed to the intersubband transition from the confined ground heavy hole state ( $E_{HH1}$ ) to the continuum heavy hole states ( $E_{HH3}$ ), which is resonantly lined up with the type-II light hole continuum states. The transition energies for the 8.9  $\mu\text{m}$  and 8.4  $\mu\text{m}$  peak wavelengths are in reasonable agreement with our theoretical calculations. While the physical origins of the twin LWIR peaks is not clear, a possible explanation can be given as follows. When the HH and LH bands in the continuum are strongly mixed, either individual subband can further split into two sub-subbands due to coupling or interaction, with one shifting up in energy and the other shifting down in energy. This gives rise to the observed twin detection peaks in the LWIR band. The MWIR peak observed at 5.5  $\mu\text{m}$  had a wavelength bandwidth ranging from 4 to 6.5  $\mu\text{m}$ . The measured responsivities of the MWIR band were found to be 7 mA/W and 13 mA/W at  $V_b = 0.3, 0.7$  V and  $T = 75$  K, respectively. The spectral bandwidth of  $\Delta\lambda/\lambda_{p3} = 27\%$  was obtained with the cut-off wavelength at  $\lambda_c = 6$   $\mu\text{m}$ . The MWIR detection is attributed to the intersubband transition between the ground heavy hole state ( $E_{HH1}$ ) and the upper continuum heavy hole state ( $E_{HH4}$ ). In this case, no mixing or interaction between the HH and LH subbands was observed. A probable explanation is that the weak overlap interaction at higher subband levels prevents the sub-subband formation.

Responsivities for this compressively strained P-QWIP were measured at  $T = 75$  K, and the results are shown in figures 8 and 9. The responsivity of the twin peak (either  $\lambda_{p1} = 8.9$   $\mu\text{m}$  or  $\lambda_{p2} = 8.4$   $\mu\text{m}$ ) LWIR band increases almost linearly with bias voltage for  $V_b \geq -1.6$  V and  $V_b \leq +1.2$  V. A similar photoresponse was obtained for the detective peak at  $\lambda_{p3} = 5.5$   $\mu\text{m}$ , as shown in figure 9. The gain has a maximum value of 0.13 at  $V_b = 1.6$  V. The linear photoresponse exhibited by this device is due to the photoconductive gain which varies linearly with bias. The maximum gain,  $G = 0.13$ , is the highest value ever reported in a P-QWIP.

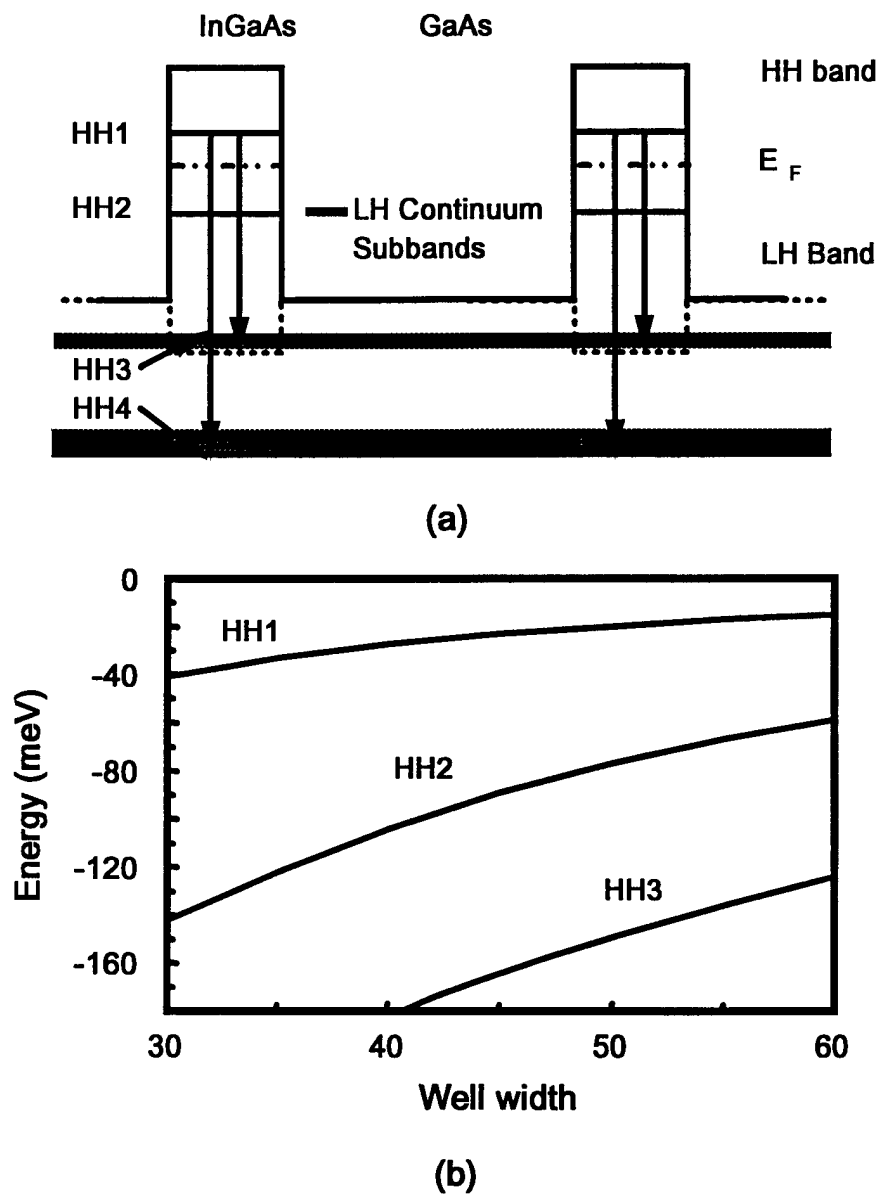


Figure 6: Schematic of the compressive strain layer InGaAs/GaAs on GaAs p-QWIP (a) and the strain-layer energy band calculations (b).

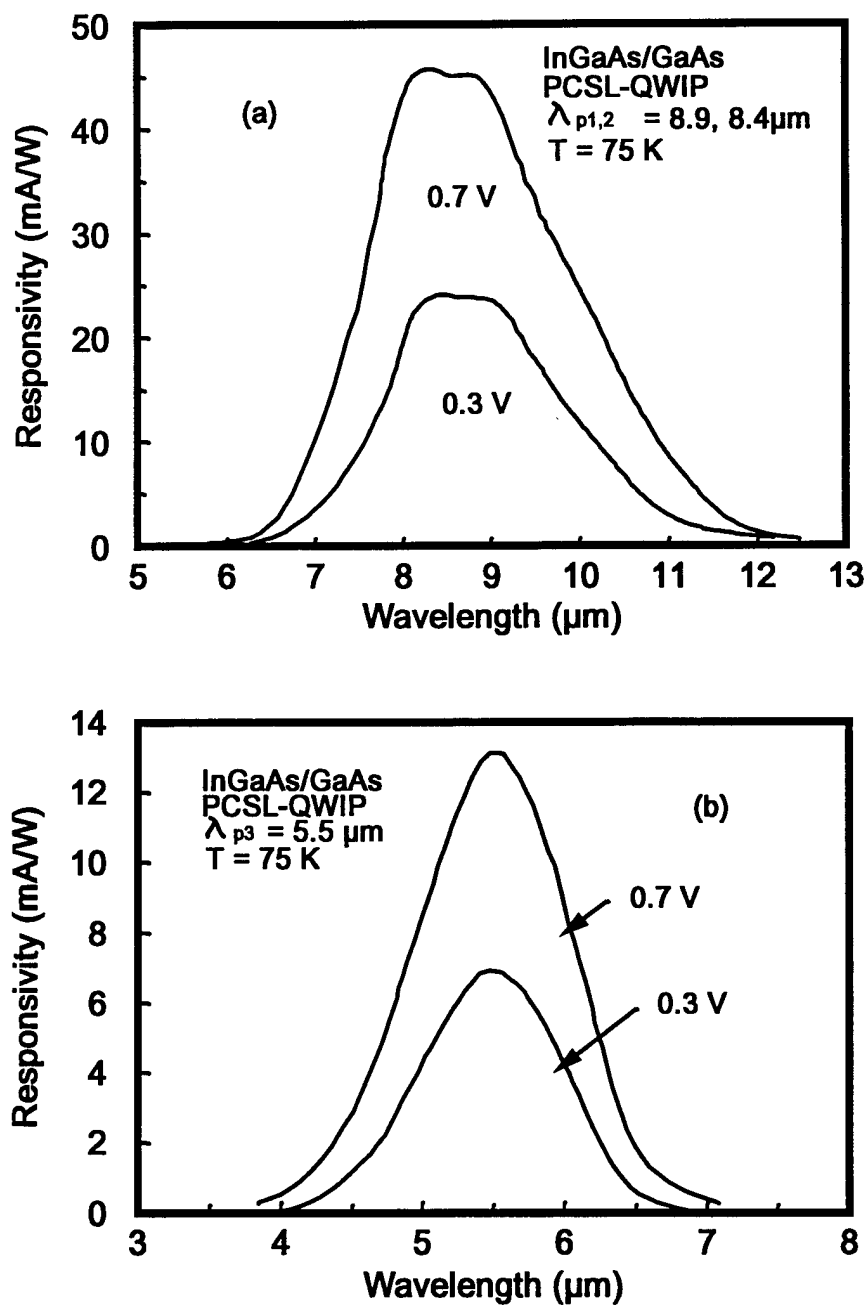


Figure 7: Measured responsivities in the LWIR band (a) and the MWIR band (b) for the InGaAs/GaAs PCSL-QWIP.

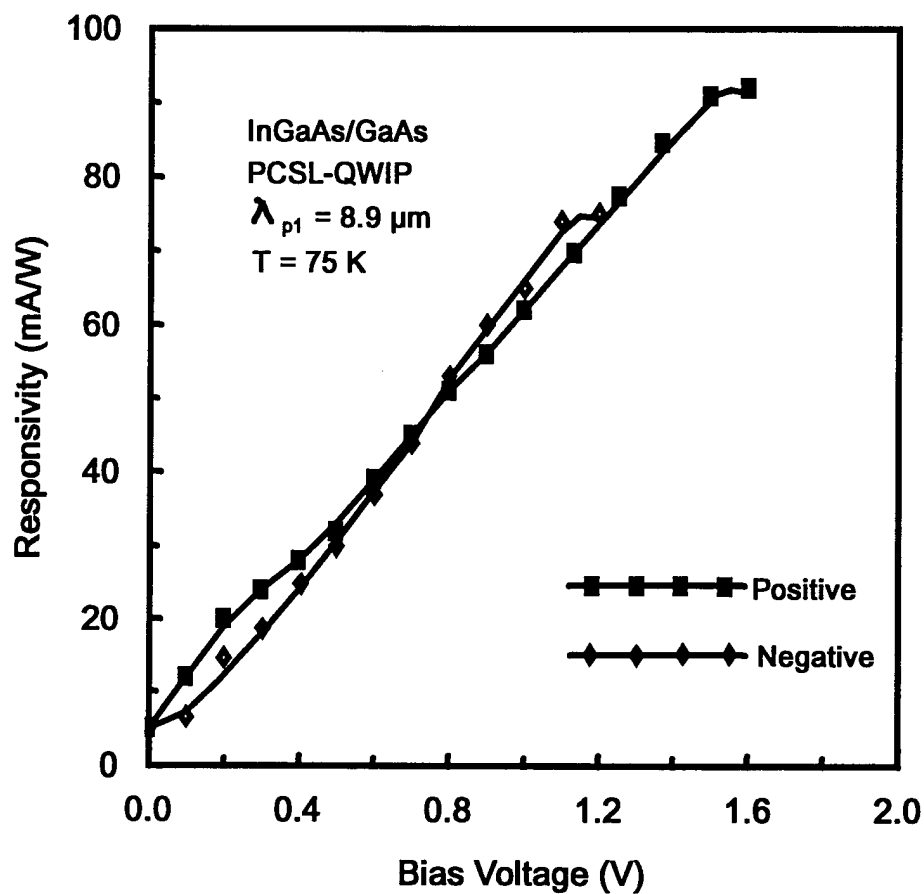


Figure 8: Measured responsivity of the InGaAs/GaAs PCSL-QWIP as a function of applied bias for  $\lambda_p = 8.9 \mu\text{m}$ .

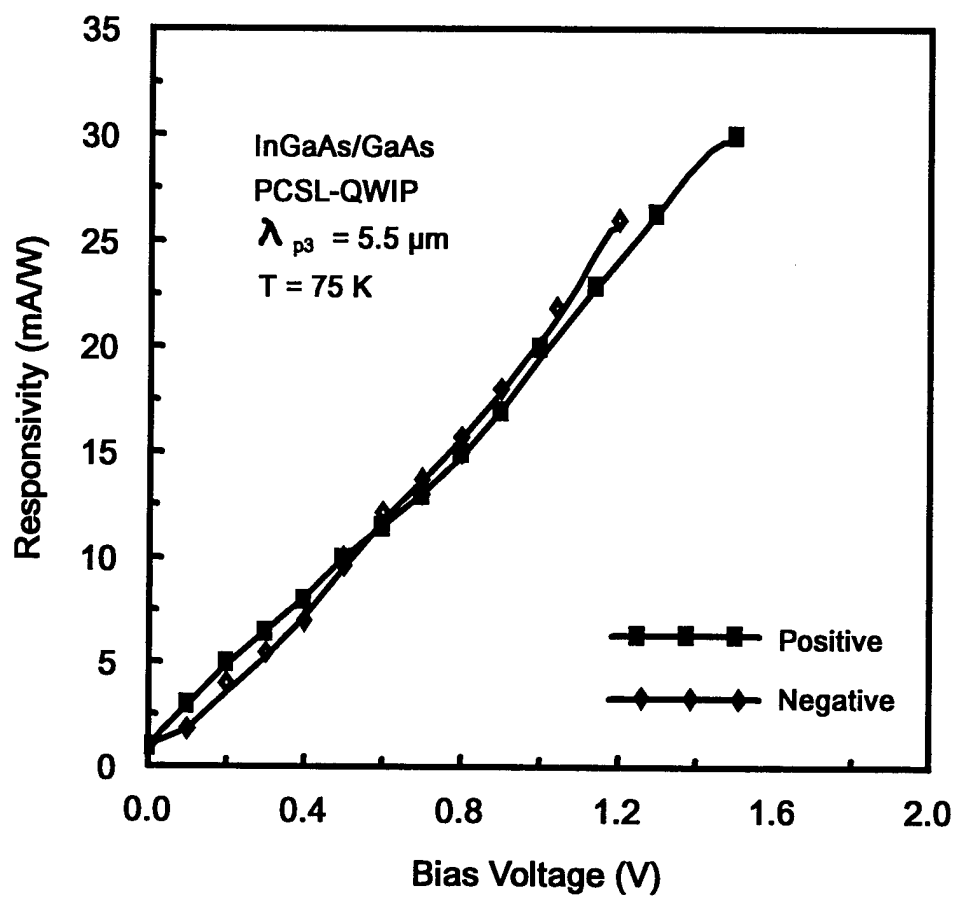


Figure 9: Measured responsivity of the InGaAs/GaAs PCSL-QWIP as a function of applied bias for  $\lambda_p = 5.5 \mu\text{m}$ .

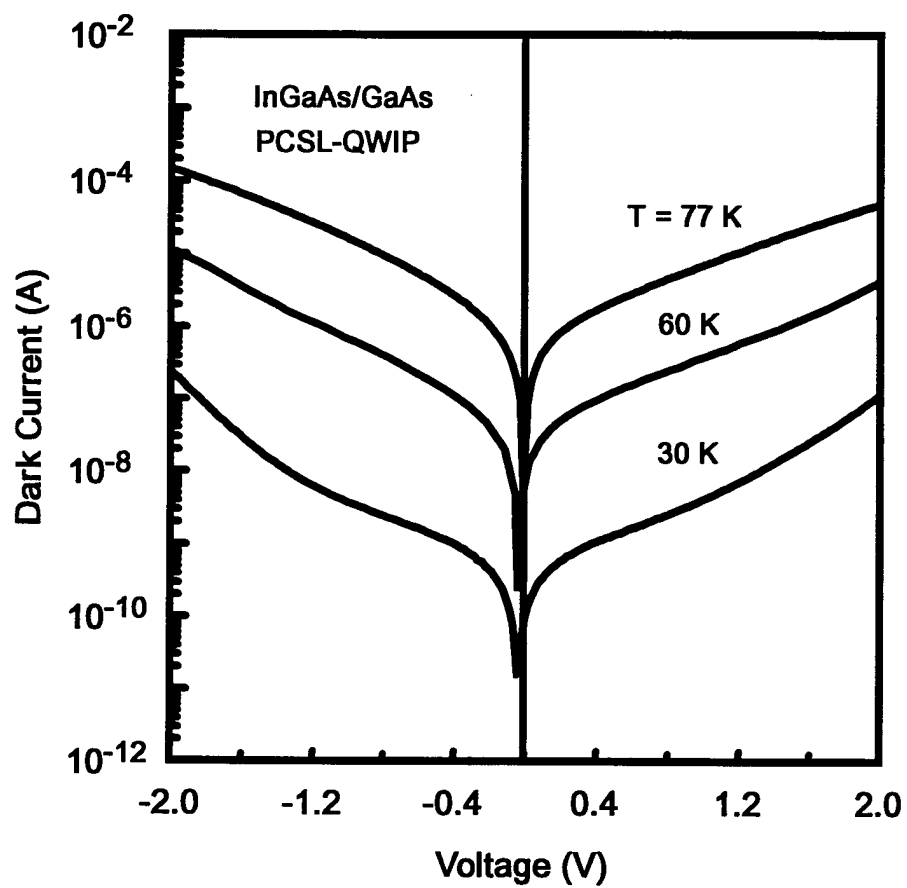


Figure 10: Measured dark current for the InGaAs/GaAs PCSL-QWIP as a function of applied bias and device temperature.

### 4.3 An InGaAs/AlGaAs on GaAs P-QWIP with compressive strain layers

A compressively strained p-QWIP based on the InGaAs/GaAs on SI GaAs was designed using the InGaAs/AlGaAs system for the quantum well/barrier structures, which was grown on the semi-insulating GaAs. With this new structure, we have demonstrated the continued viability and flexibility of the p-type compressively strained QWIP system. This structure exhibits the lowest dark current obtained for a p-type compressively strained QWIP to date, and exhibits excellent uniformity with respect to staring focal plane array applications.

The p-type compressively strained QWIP was grown on a semi-insulating GaAs substrate by molecular beam epitaxy. It consists of 20 periods of  $\text{In}(y \approx 0.2)\text{GaAs}$  quantum wells of roughly  $40 \text{ \AA}$  in width p-doped to a density of approximately  $2 \times 10^{18} \text{ cm}^{-3}$ , separated by approximately  $500 \text{ \AA}$  wide undoped  $\text{Al}(x \approx 0.15)\text{GaAs}$  barriers. A  $0.3 \text{ }\mu\text{m}$  cap layer and a  $1.0 \text{ }\mu\text{m}$  buffer layer of p-doped AlGaAs with a dopant density of  $5 \times 10^{18} \text{ cm}^{-3}$  were also grown to serve as top and bottom ohmic contacts. The contact and barrier layers are roughly lattice matched to the SI GaAs substrate so that the InGaAs quantum wells are in biaxial compression with a designed lattice mismatch of nearly  $-1.4 \%$ . Since the top and bottom contact layers are formed from heavily doped, large bandgap materials, a large tunneling current from the triangle potential near these ohmic contact regions may dominate the dark current of the QWIP. Therefore, rather thick undoped barrier layers of AlGaAs were grown between the contact layers and the QWIP structure to reduce this component of the dark current. A schematic diagram of this structure is shown in figure 11. The LWIR hole transition after absorption was designed to be from the heavy hole ground state (HH1) to the third heavy hole state (HH3), which is slightly below the valence band of the AlGaAs barrier. The MWIR transition is speculated to arise from the same heavy hole ground state to the (HH4) extended state. The extremely low dark current density levels most likely arise for the fact that the barrier height for thermionic emission is higher if the HH3 states were in resonance with the AlGaAs barrier.

To facilitate the characterization of this compressively strained p-QWIP, a  $216 \times 216 \text{ }\mu\text{m}^2$  mesa was etched onto the wafer by wet chemical etching. After patterning via a contact mask, a thin film of approximately  $1200 \text{ \AA}$  of Au/Cr was deposited onto the mesa top contact and bottom buffer contact layers via e-beam deposition at a relatively slow rate for ohmic contacts. For this sample, the semi-insulating GaAs substrate was not thinned for ease of



handling and simplification of the processing steps. Although this does lower the effective quantum efficiency of the device, by only letting the incident radiation have one pass through the quantum well layers. Further samples did utilize substrate thinning and a top reflective layer which indeed improved the device performance.

Figure 12 shows the dark current characteristic of the InGaAs/AlGaAs compressively strained p-QWIP. When compared with the dark current characteristics of the previous compressively strained p-QWIP with a LWIR peak at  $\lambda = 8.9 \mu\text{m}$ , at similar device temperatures, the dark current for the new p-QWIP is roughly two orders of magnitude lower (see previous report). As can be clearly seen in this figure, the device is under background limited performance (BLIP) conditions at temperatures of less than 63 K for applied biases of up to  $\pm 3 \text{ V}$  with BLIP temperatures of up to 70 K possible at biases of lower than approximately 1 V. When compared with the dark current characteristic of the previously studied tensile strain p-QWIP, the dark current in the compressively strained InGaAs/AlGaAs p-QWIP is still higher. Like all of the previously studied p-QWIPs, the dark current characteristic is slightly asymmetric. This can be attributed to the doping migration effect which occurs during layer growth, as previously explained<sup>32</sup>.

Again, in this p-QWIP, the mobility of the heavy-holes are enhanced by the compressive strain in the InGaAs quantum well due to the reduction of the heavy hole effective mass by a factor of three<sup>31</sup>. Another effect that is attributed to the compressional strain localized in the quantum well layer is the decrease in the density of states in the well. This phenomenon causes more heavy holes to reside in higher energy states, the net effect of which is to raise the Fermi level inside the quantum well when compared to the unstrained state. This effect not only causes an increase in the number of off-center ( $k \neq 0$ ) free heavy holes with lighter effective mass, which in turn causes a larger intersubband absorption when exposed to normal incidence IR radiation; but it also reduces the effective doping needed in the quantum well, so that the dark current is similarly reduced.

The responsivity of this p-QWIP was measured under normal incidence illumination as a function of temperature, applied bias, and incident IR radiation by using a blackbody radiation source running through an automatic PC-controlled single grating monochrometer with the appropriate filters attached. A single LWIR peak was detected at  $\lambda_p = 7.4 \mu\text{m}$  at liquid nitrogen (LN<sub>2</sub>) temperatures ( $T = 77 \text{ K}$ ) and under an applied bias of 5 V, as shown

in figure 13. A single MWIR peak was found at  $\lambda_p = 5.5 \mu\text{m}$  under the same conditions as previously mentioned, and is shown in figure 14. The respective responsivities for the LWIR and MWIR peaks were found to be 38 mA/W and 8 mA/W. The LWIR band is rather broad as illustrated in figure 13, with a cut-off wavelength of  $\lambda_c \approx 10 \mu\text{m}$ , which corresponds to a half-peak spectral bandwidth of  $\Delta\lambda/\lambda_p = 30 \%$ . The asymmetrical responsivity around the spectral peak is attributed to the long-pass filter characteristic, which has a cut-on at  $\lambda = 6.7 \mu\text{m}$ . In figure 15(a), we see the peak responsivity measured as a function of bias and device temperature. As clearly seen in this figure, the responsivity is linearly proportional to the applied bias and that the variation with temperature is minimal. The MWIR peak at  $\lambda_p = 5.5 \mu\text{m}$  has an approximate wavelength bandwidth ranging from 4 to 6.5  $\mu\text{m}$ , which overlaps with the expected bandwidth of the 7.4  $\mu\text{m}$  peak. For a cut-off wavelength of 6  $\mu\text{m}$ , a spectral bandwidth of  $\Delta\lambda/\lambda_p = 27 \%$  was obtained. Again, the responsivity as a function of bias was measured and a linear relation was found, as seen in figure 15(b).

Noise measurements were also performed on this p-QWIP using standard noise measurement procedures [38]. A Brookdeal 5004 low noise amplifier (LNA) which has an input referred current noise  $S_{ia} \approx 4 \times 10^{-27} \text{A}^2/\text{Hz}$  was used to amplify the signal generated by this QWIP. The spectral density of the output of the LNA was measured using a HP 3561A spectrum analyzer which has a bandwidth of 100 kHz and allows data collection via computer. In order to extract the device parameters, all the measurements were carried out at temperatures higher than the device BLIP temperature of 67 K.

The noise spectral density measured at a bias of 1.0 V at 81 K was found to be  $6.5 \times 10^{-28} \text{A}^2/\text{Hz}$ . Given a device area of  $216 \times 216 \mu\text{m}^2$ , and a measured current responsivity of 12.5 mA/W, we calculated a detectivity,  $D^*$ , of  $1.06 \times 10^{10} \text{cm}\sqrt{\text{Hz}}/\text{W}$  at the 7.5  $\mu\text{m}$  peak wavelength. As the bias is increased, the detectivity is decreased due to the increase in dark current and the noise spectral density. The calculated  $D^*$  values at 2 V and 3 V of applied bias are  $6.3 \times 10^9$  and  $3.2 \times 10^9 \text{cm}\sqrt{\text{Hz}}/\text{W}$ , respectively. The noise spectral density of the the p-QWIP as a function of ambient temperature and applied reverse bias voltage is shown in figure 16. As this figure shows, at a low bias voltage, the number fluctuation noise translates into current fluctuation noise via the diffusion mechanism. As the applied bias increases, charge transport becomes drift dominant and the number fluctuation noise couples to current noise via the hole drift mechanism; which results in a strong current dependence

[38].

The next step taken in the characterization of this p-QWIP was to create a structure that utilizes a thinned substrate layer and a reflective top contact to create a waveguide-like configuration that increases the responsivity of the QWIP without increasing the dark current and the noise of the p-QWIP, thereby raising the detectivity a proportional amount. This p-QWIP mesa structure was again created via wet chemical etching, and the same 120 Å of Cr with 1000 Å of Au was used as an ohmic contact and a reflective layer. The substrate was then polished to a thickness of 250 μm to create the waveguide-like structure while retaining quite a bit of mechanical strength. The dark current was measured at 77 K and was found to be in good agreement with that obtained from the previous device. The responsivity was then measured using the same system, and was found to increase at least by 33%. Given that this structure has a larger mesa area (by 50%), and taking the same noise spectral density as the previous sample, we obtain a detectivity ( $D^*$ ) of  $1.66 \times 10^{10} \text{ cm}\sqrt{\text{Hz}}/\text{W}$  at  $T = 80 \text{ K}$  and an applied bias of 1.0 V, which gives us a roughly 50% increase in detectivity. Recent developments show that the substrate layer can be thinned even further to improve the responsivity and detectivity of the device.

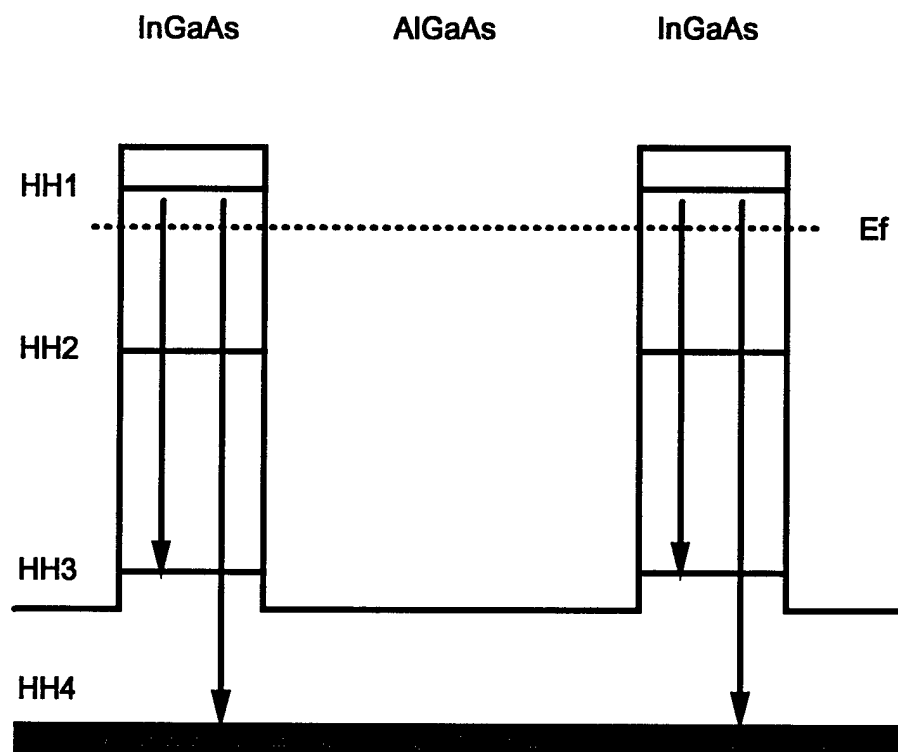


Figure 11: The schematic diagram for the two-color two-band compressively strained InGaAs/AlGaAs p-QWIP.

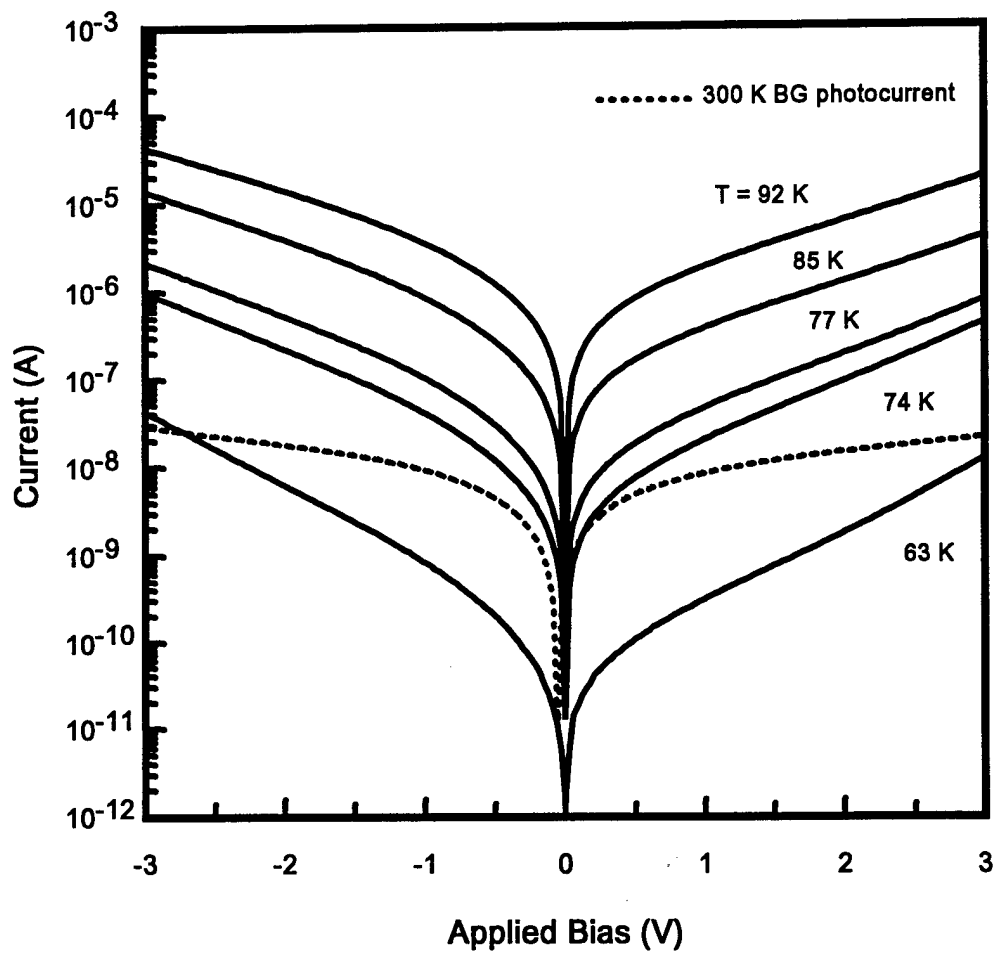


Figure 12: Dark current characteristic of the InGaAs/AlGaAs CSL p-QWIP.

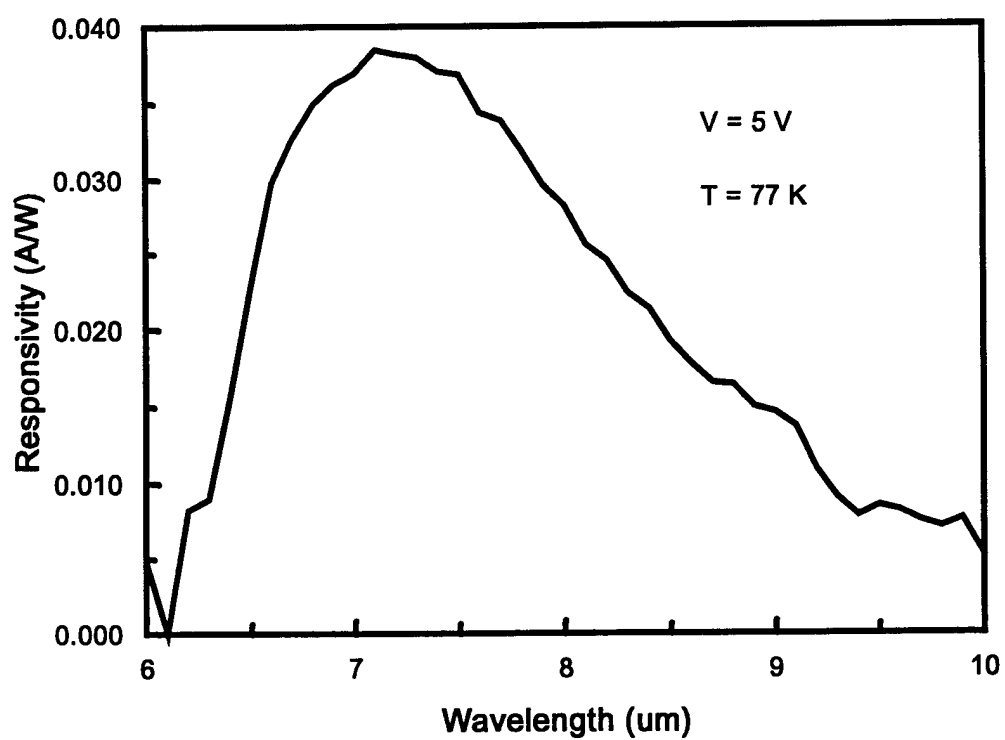


Figure 13: LWIR responsivity of the InGaAs/AlGaAs CSL p-QWIP at 77 K and +5.0 V bias.

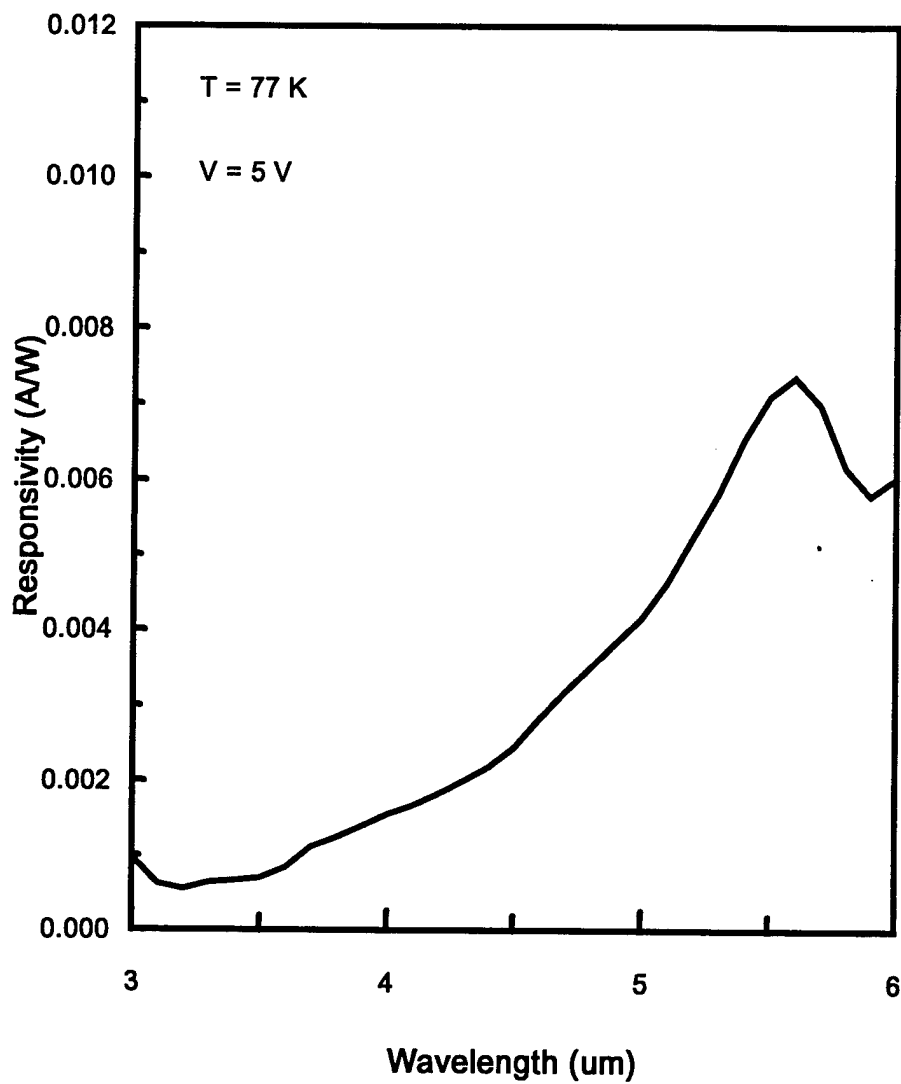
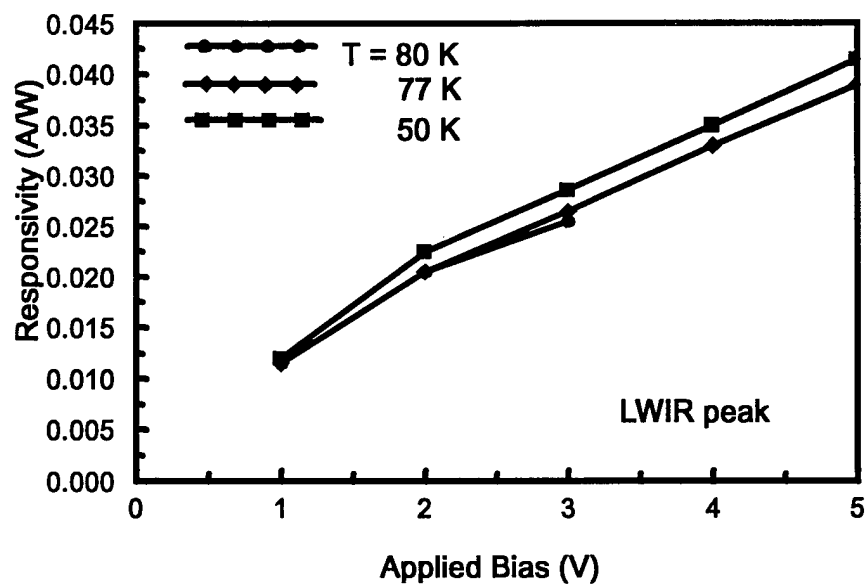
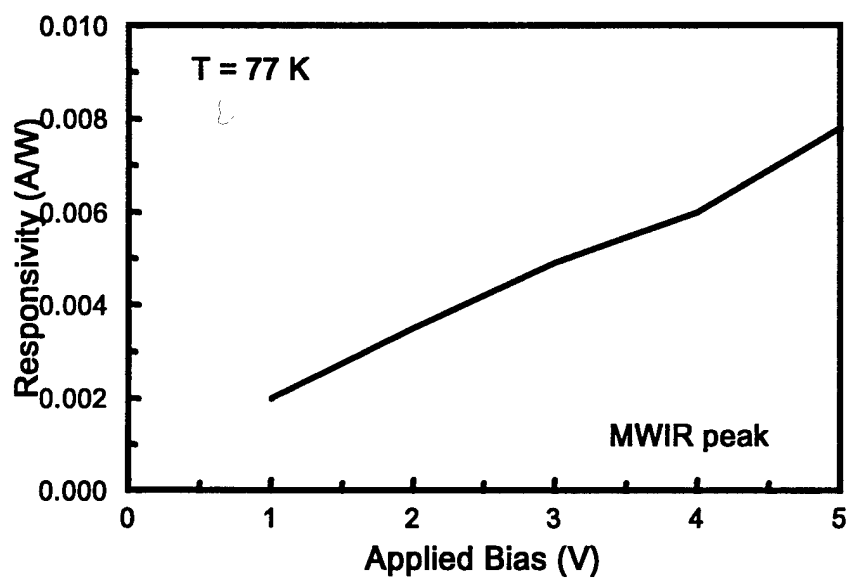


Figure 14: MWIR responsivity of the InGaAs/AlGaAs CSL p-QWIP at 77 K and +5.0 V bias.



(a)



(b)

Figure 15: (a) LWIR responsivity at  $\lambda_p = 7.4 \mu\text{m}$  and (b) MWIR responsivity at  $\lambda_p = 5.5 \mu\text{m}$  as a function of applied bias and temperature.



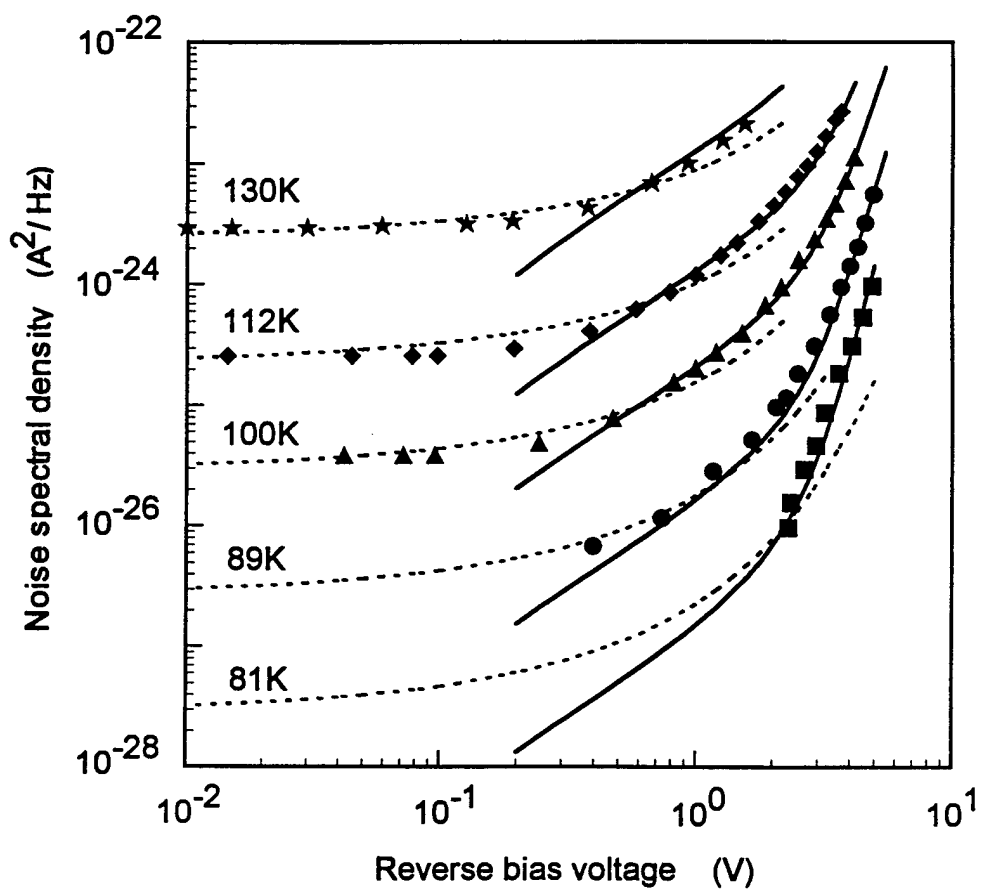


Figure 16: Experimental and theoretical current noise spectral density versus reverse bias voltage for various temperatures.

#### 4.4 A novel Si-doped GaAs/AlGaAs on (311) SI GaAs p-QWIP

All of the p-type QWIPs reported so far in the literature have utilized beryllium (Be) or carbon (C) for the dopant in the quantum well layers. However, both Be and C have serious shortcomings when used for high carrier concentration regions or very low resistance contact regions. The problem with carbon is that it is not very compatible with molecular beam epitaxy. Although Be can be easily used with MBE, it has the problem of a high diffusion coefficient, so that the dopant migration effect [32] occurs during layer growth in QWIPs. This effect can lead to the asymmetrical dark I-V characteristics observed in both the strained and the unstrained p-type QWIPs [4, 39, 40]. To cope with this phenomenon, we have successfully grown the first Si-doped p-type GaAs/AlGaAs QWIP on a SI (311) GaAs substrate. The QWIPs built from this sample do not show any of the dopant migration effect. This is due to the small diffusion coefficient of the Si impurity in the GaAs quantum well.

It has been shown that Si-doped GaAs grown by MBE exhibits a conductivity type which depends on the crystallographic orientation of the GaAs substrate and growth conditions. High concentrations of p-type doping of up to  $10^{20} \text{ cm}^{-3}$  can be achieved by doping (311) GaAs with silicon; which achieves a Hall mobility that is comparable to either Be or C doping. The GaAs/AlGaAs QWIP was grown in a Varian Modular GEN II MBE system at  $550^\circ\text{C}$ , with a group V/III beam equivalent pressure (BEP) ratio of 10, which were optimized for p-doping and material quality. An acceptor concentration of  $3 \times 10^{18} \text{ cm}^{-3}$  was achieved by Si-doping under the aforementioned conditions.

The Si-doped p-QWIP consists of GaAs quantum wells with a thickness of  $28 \text{ \AA}$  and  $300 \text{ \AA}$  wide  $\text{Al}_{0.29}\text{Ga}_{0.79}\text{As}$  barrier layers. Forty periods of the quantum well/barrier structures were grown on the (311) oriented SI GaAs substrate. The quantum wells were doped to the previously mentioned  $3 \times 10^{18} \text{ cm}^{-3}$  to obtain p-type conduction in the quantum well, while the  $\text{Al}_{0.29}\text{Ga}_{0.79}\text{As}$  barriers were not doped. A  $0.5 \text{ }\mu\text{m}$  thick GaAs cap layer and a  $1.0 \text{ }\mu\text{m}$  thick GaAs buffer layer were also Si-doped to  $3 \times 10^{18} \text{ cm}^{-3}$  to serve as ohmic contact layers. In contrast to our previous designs, a blocking barrier layer was not grown for this sample. As a result, the triangle potential formed by the heavily doped ohmic contact layers contribute to a large tunneling current which was observed in the dark I-V characteristic.

In order to test this device, a  $216 \times 216 \text{ }\mu\text{m}^2$  mesa was formed by means of wet chemical

etching. After which a thin film of 120 Å of Cr and a 1000 Å film of Au were deposited by means of e-beam evaporation on both the cap and buffer layers to serve as ohmic contact pads. The top ohmic contact consists of a thin ring type structure around the edge of the mesa with a  $50 \times 50 \mu\text{m}^2$  contact pad for electrical connection. With this contact formation, the normal incidence IR radiation is allowed to pass through the multi-quantum well layers. The technique of backside thinning to provide a waveguide-like structure and adding a reflective layer on the top of the mesa was not considered due to the mechanical brittleness of the (311) GaAs substrate; although a backside thinned structure can significantly improve the responsivity of the QWIP.

As shown in figure 17, the dark I-V characteristics of this QWIP are quite symmetrical in both the forward and reverse biased regions. This is a characteristic of uniformly doped quantum well layers, since dopants do not pile up along the growth direction of the quantum wells and therefore create a built-in electric field. Due to the lack of biaxial strain in this QWIP design, a triangular potential barrier, and the lack of a blocking barrier layer, the dark current characteristics are not as low as to be expected for a strained-layer p-QWIP. Two MWIR band peaks were found for this QWIP at 3.0 and 5.2  $\mu\text{m}$ , as seen in figure 18. Although this device is based upon the 8.0  $\mu\text{m}$  p-QWIP first grown by Levine, et al., the detection peak does not correspond with that predicted using his model. A possible reason for this is that during layer growth on the (311) substrate quantum wires can sometimes be formed throughout the QWIP layer structure. This phenomenon will further confine the allowed energy states in the QWIP and therefore the detective peaks will shift to the shorter wavelength bands. Another possible explanation of the detection peak wavelength shift is that the (311) substrate behaves much like the (110) substrate, which exhibits similar responsivities in the MWIR band.

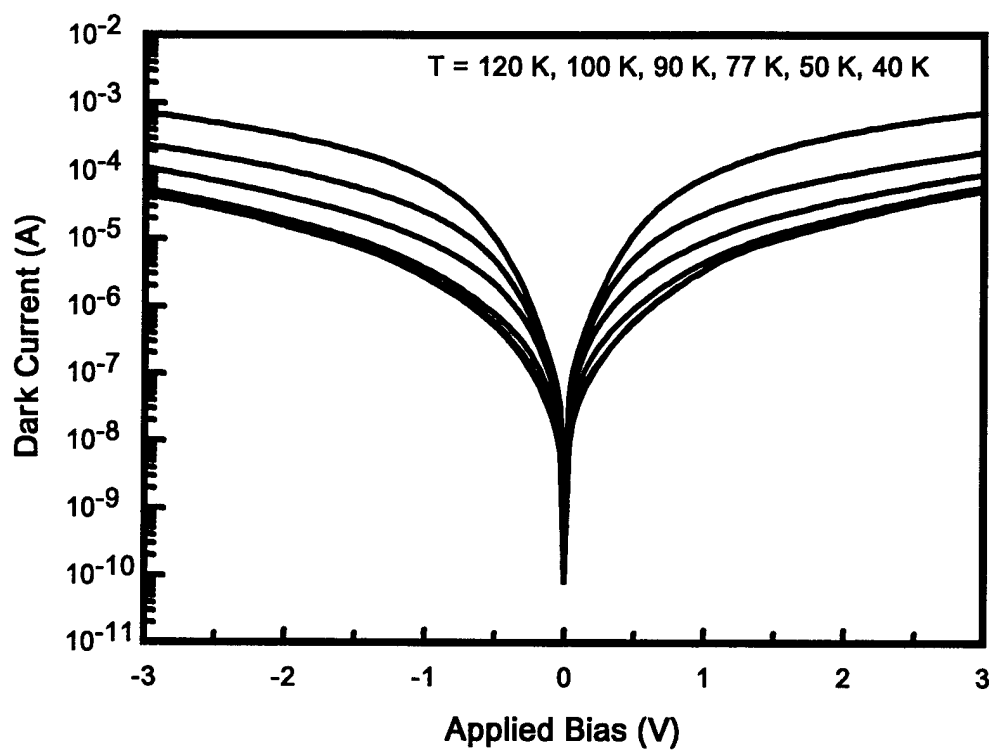


Figure 17: Dark current characteristic for the Si-doped unstrained GaAs/AlGaAs p-QWIP.

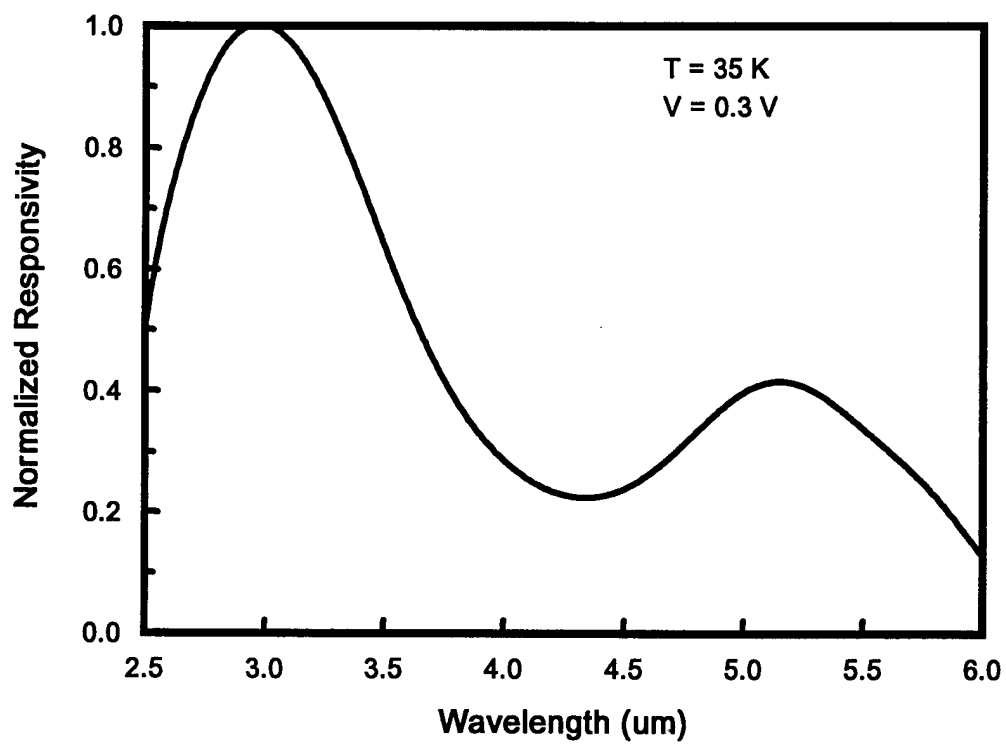


Figure 18: Normalized responsivity for the Si-doped p-QWIP.

#### 4.5 New compressively strained InGaAs/AlGaAs p-QWIPs for 10.1 and 9.2 $\mu\text{m}$ detection

Although the LWIR band ranges from 8  $\mu\text{m}$  to above 14  $\mu\text{m}$ , the main wavelength for usable detectors can be found at or near 10  $\mu\text{m}$ . Thus, there is a need to develop and characterize p-QWIPs with peak detectivity and responsivities at or near 10  $\mu\text{m}$ . After analyzing the data obtained from the 7.4  $\mu\text{m}$  compressively strained-layer p-QWIP, we have determined that the proper band offset in the InGaAs/AlGaAs system is closer to a 60/40 split with the conduction band offset being 60% of the difference in bandgap energies. Using this information, we have designed two new Be-doped p-QWIPs with peak detective wavelengths at 9.2 and 10.1  $\mu\text{m}$ . Both of these designs utilize the ground state heavy hole (HH1) to third bound state heavy hole (HH3) transition for LWIR detection. The HH3 state was designed to be in resonance with the edge of the barrier valence band edge for lowered dark current and high responsivity. With the HH3 in resonance with the barrier valence band edge, it was expected that the responsivity curve could be much broader than that obtained previously with the 7.4  $\mu\text{m}$  design which utilized a bound-to-bound state transition for detection in the LWIR band.

Similar to the previous p-QWIPs, the  $200 \times 300 \mu\text{m}^2$  mesas for these two QWIPs were created by wet chemical etching. Afterwards, a 120  $\text{\AA}$  thick layer of Cr was deposited, along with a 1000  $\text{\AA}$  thick layer of Au, to create the ohmic contacts and in this case a top reflective layer. The (100) SI GaAs substrate was then mechanically lapped to a thickness of 150  $\mu\text{m}$  to create the waveguide-like structure which the incident IR radiation passes through. It was found that this substrate thickness was more efficient than the 250  $\mu\text{m}$  structure and that it still had the mechanical strength to stand up to the ultrasonic bonding process which electrically connected the QWIPs.

As seen in figures 19 and 20, the dark current characteristics for each of these p-QWIPs is rather high. If we compare the dark current at a certain temperature for each QWIP, we see that there is a three times increase in dark current when comparing the 10.1  $\mu\text{m}$  p-QWIP with the 9.2  $\mu\text{m}$  one. This agrees with the thermionic emission theory since the difference in energy of these two levels is about 11 meV. Figure 21 shows the current responsivity of the 10.1  $\mu\text{m}$  p-QWIP. From this graph, we obtain a maximum responsivity,  $R_A$ , of 17 mA/W under an applied bias of -1.0 V at 55 K. Using the lock-in amplifier to obtain a rough estimate of the spectral noise density,  $S_n \approx 1.6 \times 10^{-25} \text{ A}^2/\sqrt{\text{Hz}}$ . When combined with the mesa area,

we calculate a detectivity,  $D^*$ , at  $10.1 \mu\text{m}$  of  $1.04 \times 10^9 \text{ cm}\sqrt{\text{Hz}}/\text{W}$ . Further studies on the noise characteristics of this  $10.1 \mu\text{m}$  p-QWIP and the  $9.2 \mu\text{m}$  p-QWIP are currently being pursued. It is interesting to note the relative wideness of the responsivity curve especially compared to the two-color  $7.4 \mu\text{m}$  peak curve. The FWHM spectral bandwidth of this detector was found to be  $\Delta\lambda/\lambda = 40\%$ . Figure 22 shows the current responsivity of the  $9.2 \mu\text{m}$  peak p-QWIP. Note the extreme broadness of this responsivity curve with a peak at  $9.2 \mu\text{m}$  which corresponds to a responsivity of  $28 \text{ mA/W}$ . The FWHM spectral bandwidth of this device is estimated at  $\Delta\lambda/\lambda = 54\%$  since the shorter wavelength cut-off was abruptly terminated by the long-pass filter which has a cut-on at  $6.7 \mu\text{m}$ . Again, using the lock-in amplifier to obtain an estimate of the noise spectral density of the device,  $S_n \approx 6.4 \times 10^{-25} \text{ A}^2/\sqrt{\text{Hz}}$ . Using this information and the device area with the measured responsivity, we determine a detectivity at  $9.2 \mu\text{m}$  and  $T = 45 \text{ K}$  with an applied bias of  $-2.5 \text{ V}$  of  $2.7 \times 10^9 \text{ cm}\sqrt{\text{Hz}}/\text{W}$ . Although the forward bias responsivity is slightly lower than that measured for the reverse bias case, e.g.  $22 \text{ mA/W}$  at  $T=45 \text{ K}$  and  $V=3.0 \text{ V}$  we can expect a higher detectivity due to the lower dark current and the lower corresponding spectral noise density. Further modifications on this design are in progress in an attempt to lower the dark current density, and the corresponding noise spectral density, in addition to narrowing the responsivity curve. Additionally, further studies into a MWIR peak for both of these p-QWIPs and further characterization of these p-QWIPs at higher temperatures are currently being pursued.

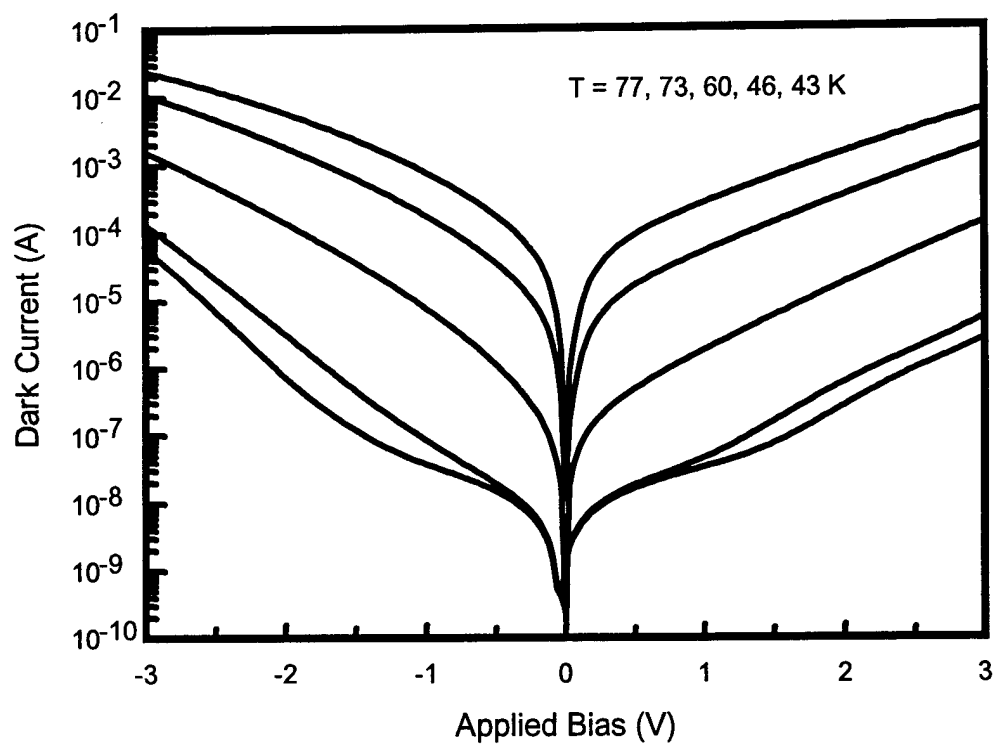


Figure 19: Dark current characteristic for the CSL InGaAs/AlGaAs p-QWIP with a detective peak at  $\lambda_p = 10.1 \mu\text{m}$ .



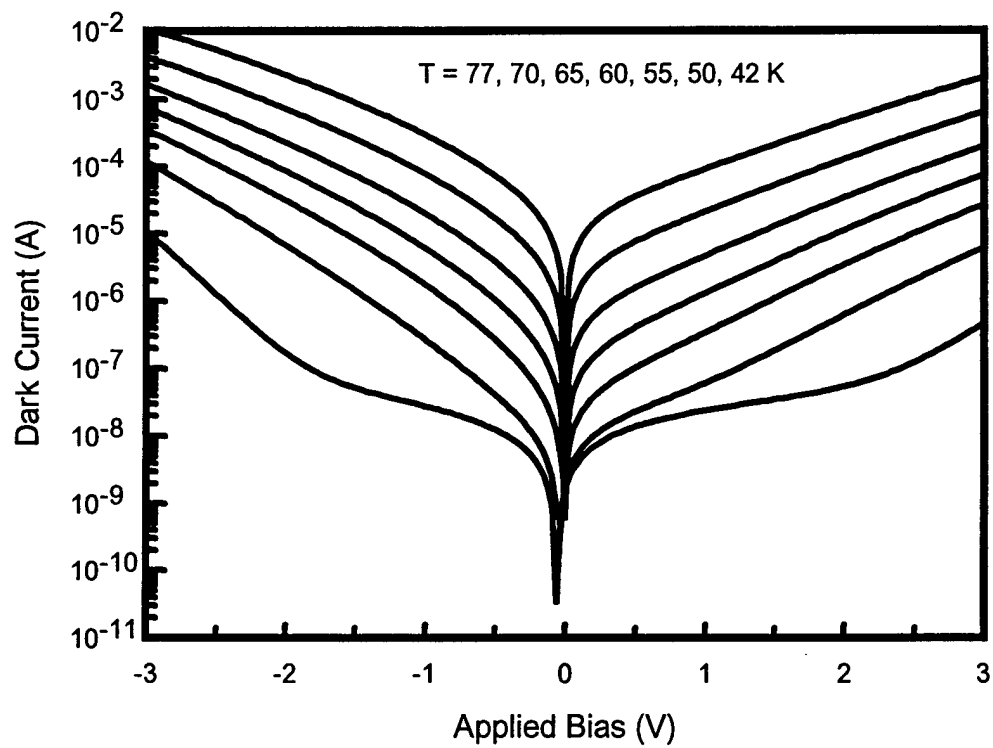


Figure 20: Dark current characteristic for the CSL InGaAs/AlGaAs p-QWIP with a detective peak at  $\lambda_p = 9.2 \mu\text{m}$ .

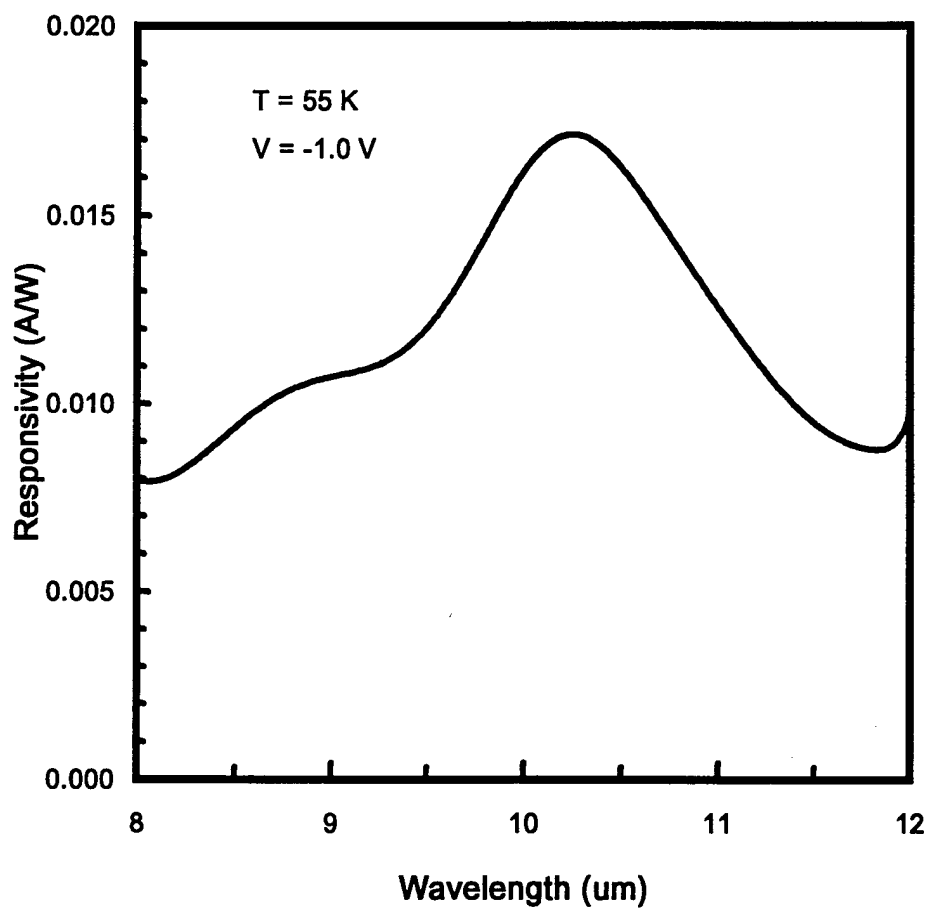


Figure 21: Measured LWIR responsivity of the  $\lambda_p = 10.1 \mu\text{m}$  CSL p-QWIP at 55 K and -1.0 V bias. Estimated  $D^* = 1.04 \times 10^9$  Jones.

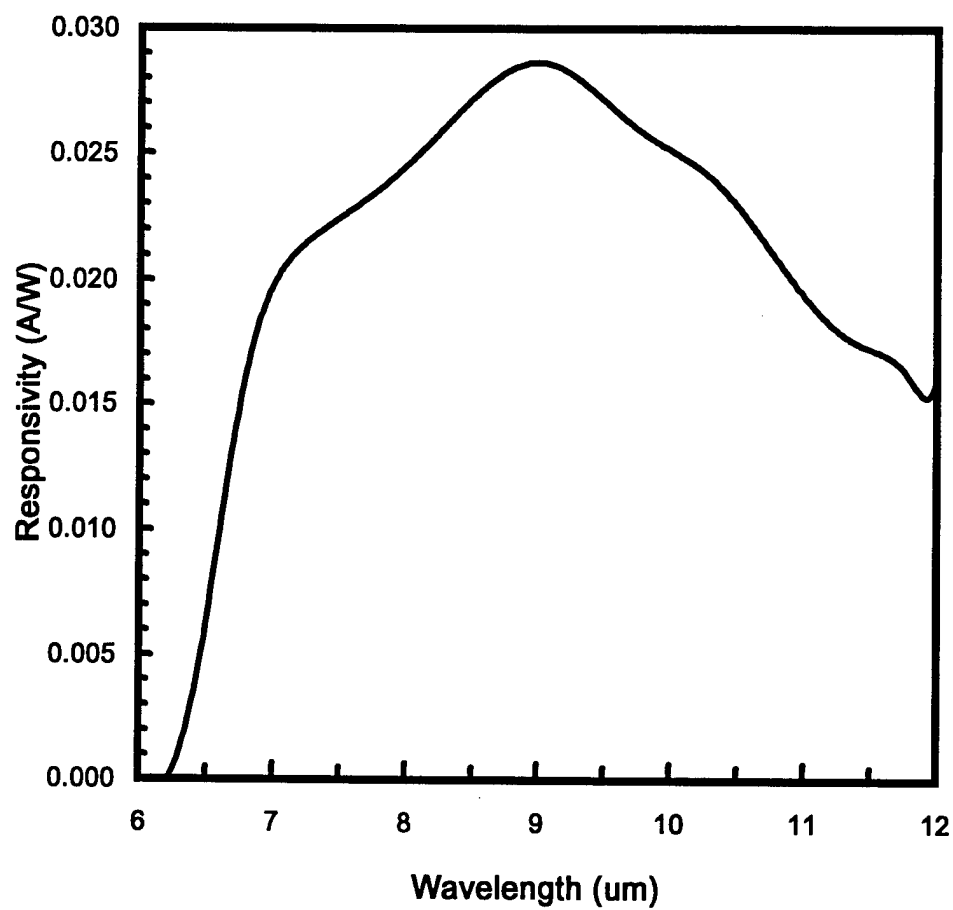


Figure 22: Measured LWIR responsivity of the  $\lambda_p = 9.2 \mu\text{m}$  CSL p-QWIP at 45 K and -2.5 V bias. Estimated  $D^* = 2.7 \times 10^9$  Jones.

#### 4.6 A New p-type InGaAs/GaAs/AlGaAs SBTM QWIP at 10.4 $\mu\text{m}$

A new compressively strained-layer (CSL) p-type QWIP with a detective peak at 10.4  $\mu\text{m}$  based on the InGaAs/GaAs/AlGaAs material system was designed, fabricated, and characterized. The new p-QWIP uses the step-bound-to-miniband (SBTM) intersubband transition as the basis for infrared detection. With this structure, we have again demonstrated the flexibility of the compressively strained p-type QWIP system. This structure exhibits the longest peak wavelength and corresponding cut-off wavelength ( $\geq 13 \mu\text{m}$ ) of any of the p-type QWIPs previously studied, in addition to exhibiting excellent uniformity from device to device.

As illustrated in figure 23, the transition scheme for this p-QWIP is from the ground bound heavy hole state (HH1) to the third excited heavy hole state (HH4), which is in resonance with the miniband formed by the GaAs/ $\text{Al}_{0.35}\text{Ga}_{0.65}\text{As}$  superlattice (SL) barriers. This structure creates a potential difference between the SL barriers and the quantum well which blocks part of the undesirable dark current from the heavily doped ground state in the wide  $\text{In}_{0.12}\text{Ga}_{0.88}\text{As}$  quantum well [41]. The physical parameters described later were chosen so that the ground state in the wide InGaAs quantum well is well above the top of the GaAs/AlGaAs SL barrier, and the third excited heavy-hole state (HH4) is resonant with the ground level of the superlattice miniband (SL1) so that a large quantum well width is maintained for high quantum efficiency, although the absorption coefficient is sacrificed. Along the miniband, the photoexcited holes can easily tunnel due to the large overlap of allowed states in the superlattice barrier at the correct energy, thus transporting through the superlattice barriers until the hole is reabsorbed into a quantum well or collected by the ohmic contacts. The calculated transmission coefficient versus energy is shown in figure 24.

The p-type SBTM CSL-QWIP was grown on a (100) S.I. GaAs substrate by molecular beam epitaxy. It is made up of 90 Å thick quantum wells Be-doped to a density of  $3 \times 10^{18} \text{ cm}^{-3}$ , which populates the ground heavy-hole states (HH1). The quantum well layer is compressively strained with a lattice mismatch of -0.8%. Surrounding the quantum well layers are the superlattice barriers which consist of 20 Å thick superlattice barriers of undoped  $\text{Al}_{0.35}\text{Ga}_{0.65}\text{As}$  alternating with 27 Å thick undoped GaAs superlattice wells. The complete superlattice barrier is then made from ten periods of the alternating superlattice barrier/well structure, which is lattice matched to the GaAs substrate. The whole superlat-

tice barrier/quantum well formations are then repeated 20 times to create the active layers of the p-type SBTM CSL-QWIP. Ohmic contacts are formed from a  $0.5\text{ }\mu\text{m}$  thick GaAs cap layer and a  $1.0\text{ }\mu\text{m}$  thick GaAs buffer layer, which are heavily Be-doped to  $5\times 10^{18}\text{ cm}^{-3}$  and are grown on top of the QWIP stack and between the QWIP stack and substrate, respectively. The complete layer structure is given in figure 25.

To facilitate the characterization of the p-QWIP, a  $216\times 216\text{ }\mu\text{m}^2$  mesa was etched onto the wafer by wet chemical etching. After patterning with a contact photomask, a thin film of  $120\text{ }\text{\AA}$  of Cr was deposited by e-beam evaporation. This layer was topped off by a  $1000\text{ }\text{\AA}$  thick layer of Au to form both the top and bottom ohmic contacts. The top ohmic contact consists of a ring-like structure around the edge of the mesa with a  $50\times 50\text{ }\mu\text{m}^2$  contact pad for electrical connection. In this type of contact formation, the normal incidence radiation is only allowed one pass through the QWIP layers; which limits the effective quantum efficiency, especially when compared with those backside illuminated, thinned QWIPs which take advantage of a reflective top layer and waveguide structure to increase the number of times the incident IR radiation passes through the SBTM QWIP.

Device characterization was performed in a closed cycle helium cryogenic dewar. A HP 4145B semiconductor parameter analyzer was used to measure the dark I-V characteristics and the 300 K background photocurrent. Under dark conditions, holes can be transferred out of the quantum wells and produce the thermally generated carriers by two main mechanisms—thermionic emission out of the quantum wells and thermally generated carriers tunneling through the superlattice barriers. Given the high aluminum content in the superlattice barriers (Al fraction is 0.35), a considerable indium content in the quantum well (In fraction is 0.12), and the effect of the compressive strain lowering the energy of the heavy hole states in the quantum well regions, the effective barrier seen by the ground heavy-hole states is 299 meV; which should suppress thermionic emission out of the quantum wells. Because of the heavily doped ohmic contact regions, a large triangle potential is formed which should lower (or thin) the barrier to thermionically assisted tunneling and thus gives rise to a higher than expected dark I-V characteristics. Future designs will take this into account and compensate for the large triangle potential.

Figure 26 shows the measured dark I-V characteristic with the 300 K background photocurrent superimposed. When compared with a similar n-type SBTM QWIP [41], the dark

current is much higher. As previously mentioned, the high dark current of this p-QWIP is attributed to the triangle potential formed by the heavily doped ohmic contact, which contributes a large tunneling current component to the dark current.

The measured long-wavelength photoresponse for the p-type SBTM CSL-QWIP is shown in figure 27. A single peak was found at  $\lambda_p = 10.4 \mu\text{m}$ , which is in excellent agreement with the theoretically calculated value of  $10 \mu\text{m}$ . With a long wavelength cut-off,  $\lambda_c \geq 13 \mu\text{m}$ , and a half-peak value at  $12 \mu\text{m}$ , we determined the spectral bandwidth to be,  $\Delta\lambda/\lambda_p = 20 \%$ . This narrow responsivity bandwidth is consistent with that expected from a bound-to-miniband transition scheme. The maximum responsivity of  $28 \text{ mA/W}$  was found at  $T=65 \text{ K}$  and  $V_b=+3.0 \text{ V}$ , as seen in figure 28, the responsivity versus bias curve. As seen in the  $T=40 \text{ K}$  curve, the gain of the p-type SBTM CSL-QWIP has not saturated at  $V=5.0 \text{ V}$ . The apparent saturation of the photoresponse of the  $T=65 \text{ K}$  curve is due to the limitations of our amplifiers. At  $T=65 \text{ K}$ , the noise spectral density was estimated as  $4.0 \times 10^{-26} \text{ A}^2/\text{Hz}$  at a bias of  $1.0 \text{ V}$ . Corresponding to this operating point, the measured responsivity at  $10.4 \mu\text{m}$  was  $13 \text{ mA/W}$ . Using the above data, the spectral detectivity was determined to be  $D^* = 1.4 \times 10^9 \text{ cm}\sqrt{\text{Hz}}/\text{W}$ .

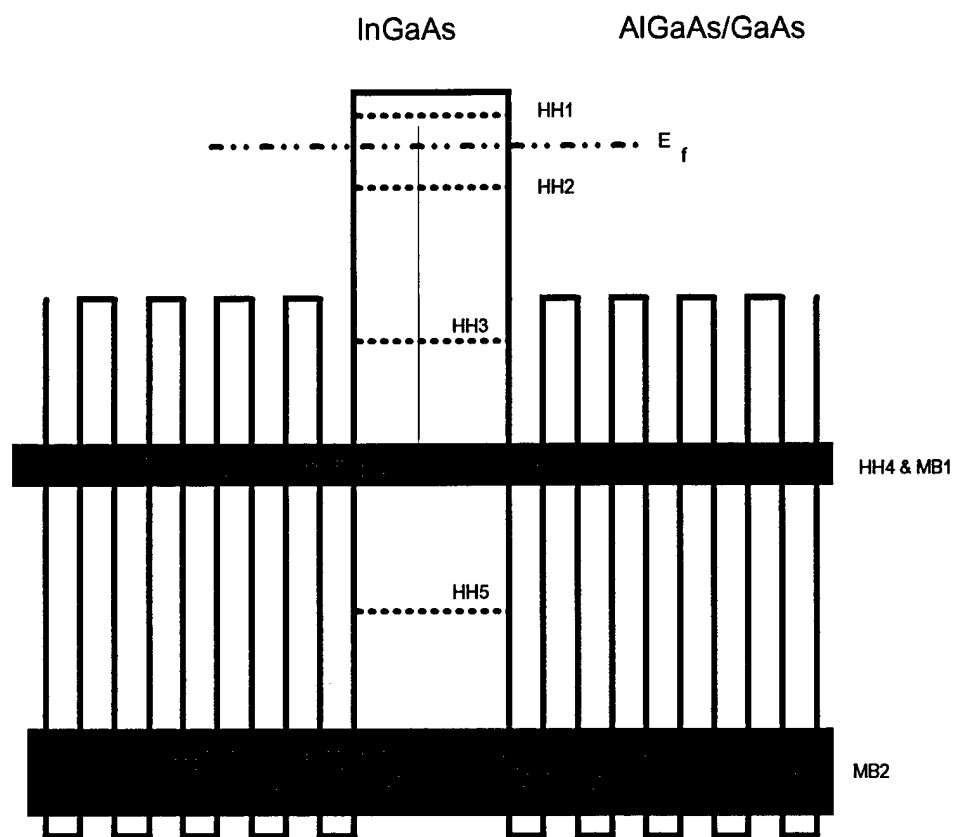


Figure 23: The schematic diagram for new 10.4  $\mu\text{m}$  peak compressively strained InGaAs/AlGaAs/GaAs p-type SBTM CSL-QWIP.

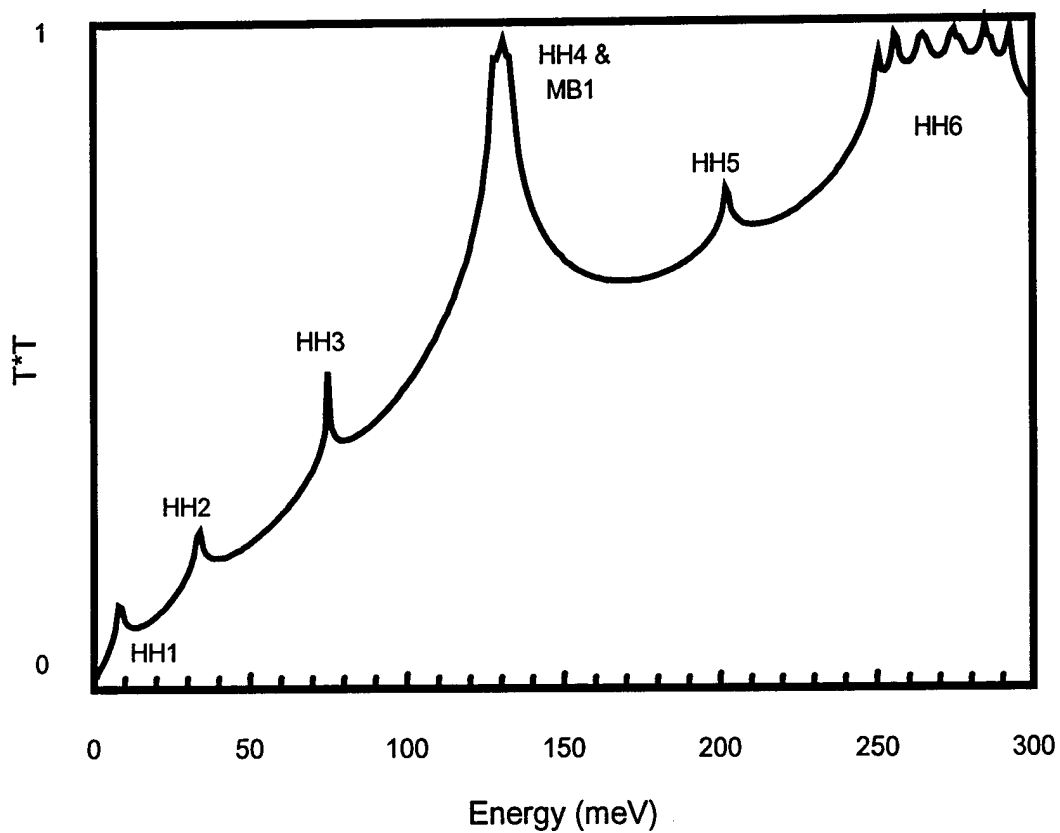


Figure 24: The calculated transmission peaks for the InGaAs/AlGaAs/GaAs compressively strained p-type SBTM CSL-QWIP.



				<hr/>	
		0.5 $\mu\text{m}$	GaAs	$p=5\times 10^{18} \text{ cm}^{-3}$	<hr/>
		20 $\text{\AA}$	$\text{Al}_{0.35}\text{Ga}_{0.65}\text{As}$	undoped	
$20 \times \left\{ \right.$		27 $\text{\AA}$	GaAs	undoped	<hr/>
		$\vdots$			
		90 $\text{\AA}$	$\text{In}_{0.12}\text{Ga}_{0.88}\text{As}$	$p=3\times 10^{18} \text{ cm}^{-3}$	
		$\vdots$			
		20 $\text{\AA}$	$\text{Al}_{0.35}\text{Ga}_{0.65}\text{As}$	undoped	<hr/>
		27 $\text{\AA}$	GaAs	undoped	
		$\vdots$			<hr/>
		1.0 $\mu\text{m}$	GaAs	$p=5\times 10^{18} \text{ cm}^{-3}$	
SI (100) GaAs				<hr/>	

Figure 25: The layer structure for the p-type SBTM CSL-QWIP.

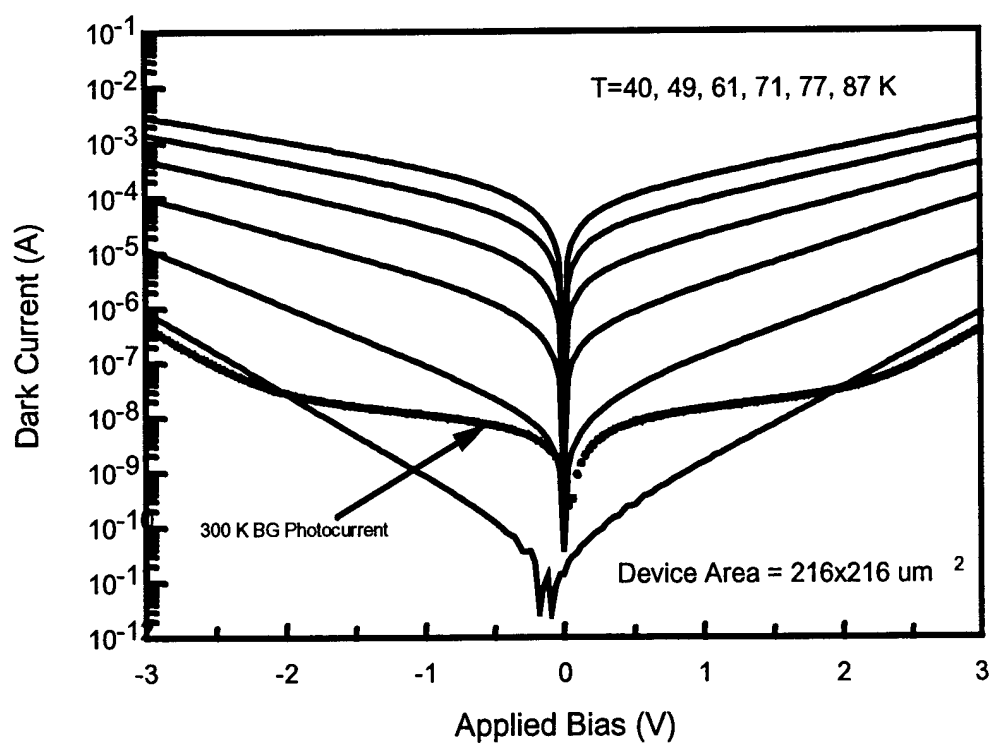


Figure 26: Measured dark I-V and 300 K background photocurrents for the p-type SBTM CSL-QWIP.

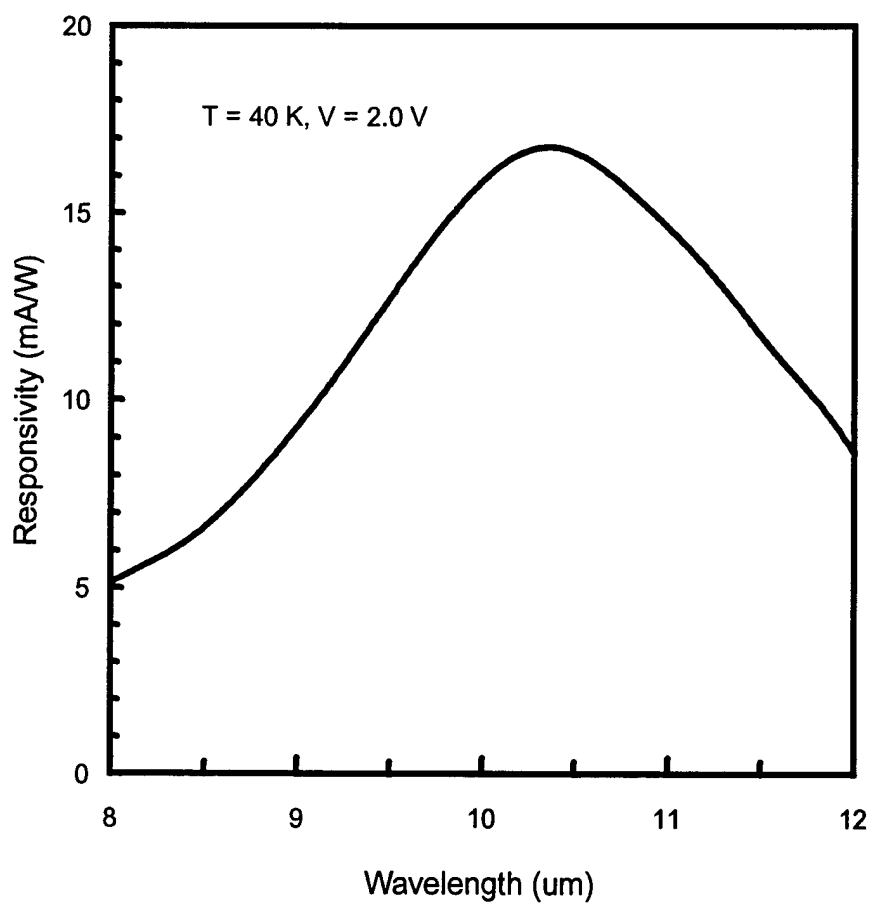


Figure 27: The measured photoresponse versus incident IR wavelength at  $T=60$  K,  $V=2.0$  V for the p-type SBTM CSL-QWIP.

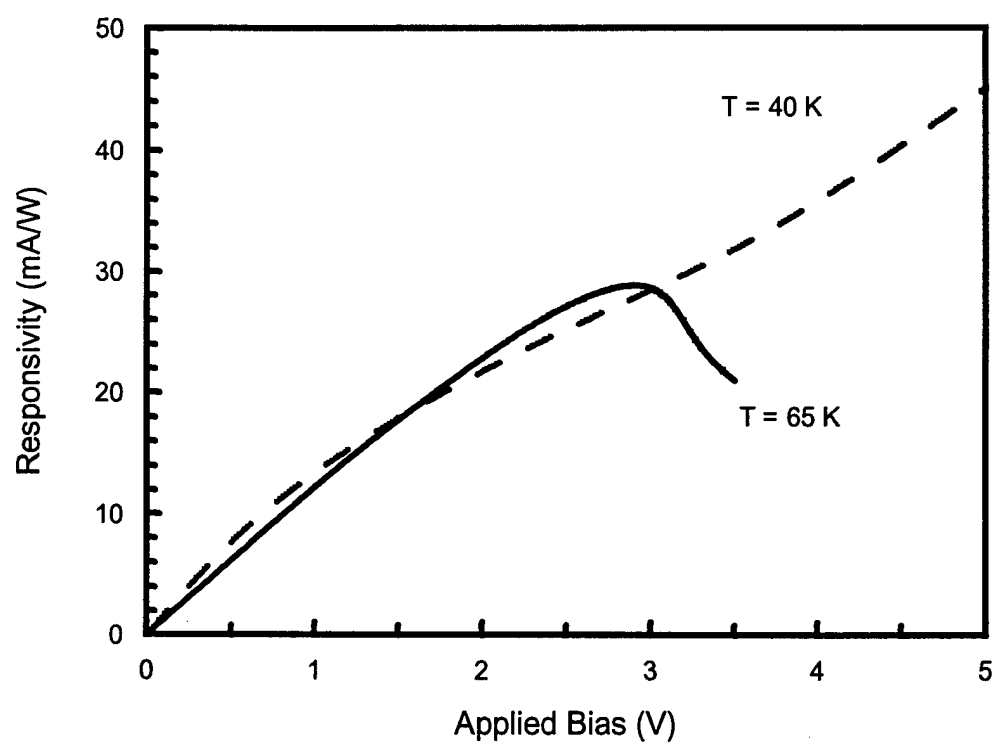


Figure 28: The measured responsivity versus bias at  $10.4\text{ }\mu\text{m}$  and various temperatures.

#### 4.7 Noise Performance of a p-type Strained-layer QWIPs

The noise performance of the 7.4  $\mu\text{m}$  peak ultra-low dark current p-QWIP was extensively studied during this reporting period. The performance specifications of this p-QWIP are summarized in Table A and are explained in detail in the previous report.

Measurements were carried out using standard noise measurement procedures [38]. A Brookdeal 5004 low noise amplifier (LNA) which has an input referred current noise,  $S_{in} \approx 4 \times 10^{-27} \text{ A}^2/\text{Hz}$ , was used to amplify the signal generated by the device. Since this detector exhibits very low current noise and high dynamic resistance, we were limited by the amplifier current noise. The spectral density of the output of the LNA was measured using a HP 3561A spectrum analyzer. The device was placed in a nitrogen flow cryostat which allows for temperature variation between 80 K and room temperature. The cryostat also acted as an external noise shield.

Figure 29 shows the noise spectra measured from 10 Hz to 100 kHz. In the high frequency range ( $f > 1 \text{ kHz}$ ), the noise spectral density is affected by RC parasitic effects. But after corrections are made, frequency independent noise levels are found. The noise plateaus are attributed to hole trapping and detrapping in the quantum well bound states. The data also indicates that most of the current spectra are frequency independent down to 10 Hz. Only under high bias, e.g.  $|V_{bias}| > 4 \text{ V}$ , does excess noise show up in the spectra for frequencies below 100 Hz.

The noise plateau values plotted as a function of dark current is shown in Figure 30. From this plot, two distinct regimes of operation can be recognized. In the low field diffusion dominant regime, noise values are nearly independent of the DC current. The observed low bias noise values agree with those calculated from the Nyquist expression at zero applied bias voltage for the measured temperatures. In the high field, drift dominated regime, the noise values become strongly dependent on the DC current. This general behavior is quite similar to what Rose predicted for traditional photoconductive devices [42].

From the measured data, we were able to determine the expression for the noise current plateau values in the drift dominant regime as

$$S_i = \frac{4I_d^2}{NAL_w C e^{(-\frac{E_b - \Delta E}{k_B T})}}, \quad (63)$$

where  $I_d$  is the dark current,  $N$  is the total number of quantum wells,  $A$  is the device cross-

sectional area,  $L_w$  is the width of the quantum well,  $E_b = E_v - E_o$  is the energy barrier seen by the holes in the quantum well states,  $\Delta E = q\Delta\phi + q\varepsilon L_w$ , which is the total energy barrier lowering including both the electric field effect and the Schottky image effect,  $k_b$  is the Boltzmann constant,  $T$  is the temperature, and  $C$  is the hole generation rate constant.  $C$  was determined to be  $9.4 \times 10^{30} \text{ cm}^{-3}\text{s}^{-1}$ , by fitting measured data with the above equation. Using this data and the expression for the noise current spectral density in the diffusion dominated regime,

$$S_i = 4q^2 N A L_w C e^{(-\frac{E_b - \Delta E}{k_B T})} \left( \frac{L_D}{L} \right)^2, \quad (64)$$

we can determine the diffusion length,  $L_D$ . For this device, the diffusion length was found to be 450 Å.

The following model is used to explain the value of  $C$  and derive a value for the capture cross section  $\sigma_p$  within the context of the hole transport mechanism and quantum well characteristics. Thermally generated heavy holes will move via drift or diffusion in the barrier region to a neighboring quantum well. These quantum wells are heavily doped with beryllium acceptors to a concentration of  $2 \times 10^{18} \text{ cm}^{-3}$ , which results in an inter-acceptor spacing of about 100 Å. Since the well width is only 48 Å, these acceptors are postulated to basically form a thin plane of nearly neutral charge centers. The holes approaching this monolayer with a thermal velocity determined by barrier parameters will interact with these Be-centers, triggering a recombination process. Assuming ineffective screening of the Be nuclei due to the two dimensionality of the surrounding electron gas, the Be perturbation potential can be approximated by  $\frac{Zq}{4\pi\epsilon_o\epsilon_r r}$ , where  $Z=4$  [43]. Note that holes impinging on the Be-centers gain kinetic energy by crossing the barrier/quantum well interface. Thus the perturbation potential must equal the energy gained from the barrier/quantum well interface and the hole thermal energy, or

$$\frac{Zq}{4\pi\epsilon_o\epsilon_r r} = E_b + E_{th}, \quad (65)$$

from which  $\sigma_p = \pi r^2$  can be calculated.

We calculated at  $T=100 \text{ K}$ , that  $\sigma_p(100 \text{ K}) = 1.9 \times 10^{-13} \text{ cm}^2$ . The measured value that follows from  $C = N_a N_v v_{th} \sigma_p = 9.4 \times 10^{30} \text{ cm}^{-3}\text{s}^{-1}$ . Using  $N_a = 2 \times 10^{18} \text{ cm}^{-3}$  and bulk GaAs values for  $N_v$  and  $v_{th}$ , we find that  $\sigma_{p,exp} = 2.6 \times 10^{-13} \text{ cm}^2$ , which is in good agreement with the predictions of this model.

At zero bias, the following picture emerges for QWIP operation. Holes are thermally generated from the quantum well bound states into the extended states of the device with equal probabilities for transferring to the neighboring quantum well on the anode or cathode side, in equilibrium. The hole lifetime of the bound states is large compared to the barrier transit time, allowing the holes to fully thermalize in the wells. This thermalization process decouples the statistical fluctuations in hole transport through a barrier from one period to the next. As a result, the QWIP can be thought of as consisting of  $N$  statistically independent sections made up of a barrier region with two contacts from which the holes are emitted. In equilibrium, the net hole current through any cross sectional plane is zero, which results from the detailed balance between two opposing currents,  $I_o$ . Assuming full shot noise in each current, the current noise spectral density of a single section becomes  $S_{i(section)} = 4qI_o$ . Then the total noise is

$$S_i = \frac{S_{i(section)}}{N} = \frac{4qI_o}{N} = S_{i(Nyquist)}. \quad (66)$$

When an electric field is present, producing a voltage drop,  $V_b$  across a section, then the total current becomes

$$I = I_s[1 - \exp(-\frac{qV_b}{k_B T})] \quad (67)$$

where  $I_s$  is the saturation current. In equilibrium,  $I_s = I_o$  and the total current is zero. With an electric field, the saturation current will increase due to field induced barrier lowering and the image effect. So that,  $I_s = I_o \exp(\frac{\Delta E}{k_B T})$ , and the dark current values can be calculated. The measured dark current and our calculated results based on the above equations are shown in figure 31.

Figure 32 shows the dark I-V characteristics of this 9.2  $\mu\text{m}$  peak p-QWIP. The current was calculated assuming a constant applied electric field throughout the device, and at low fields, the holes are thermally generated from a quantum well and travel, on average, one period before they trap and fully thermalize into the neighboring quantum wells. Good agreement is obtained between the theoretical calculations (symbols) and the measured results (solid line).

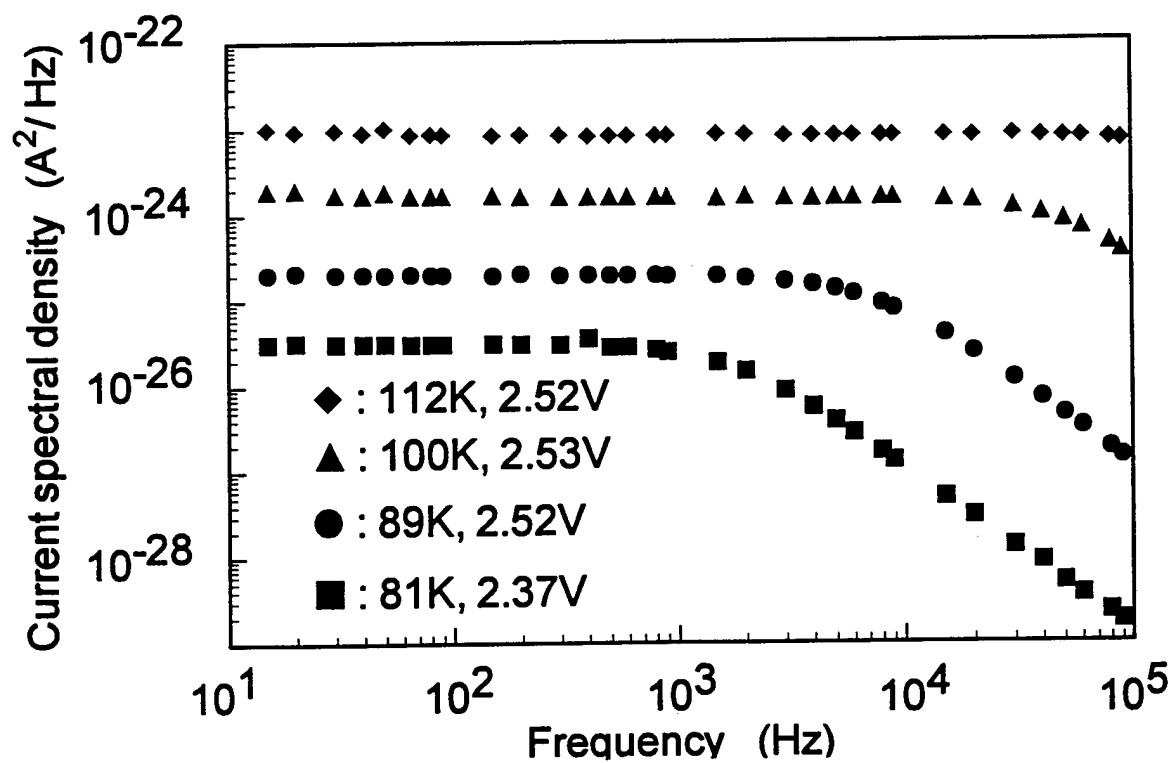


Figure 29: Current noise spectral density versus frequency at different bias voltages and temperatures.



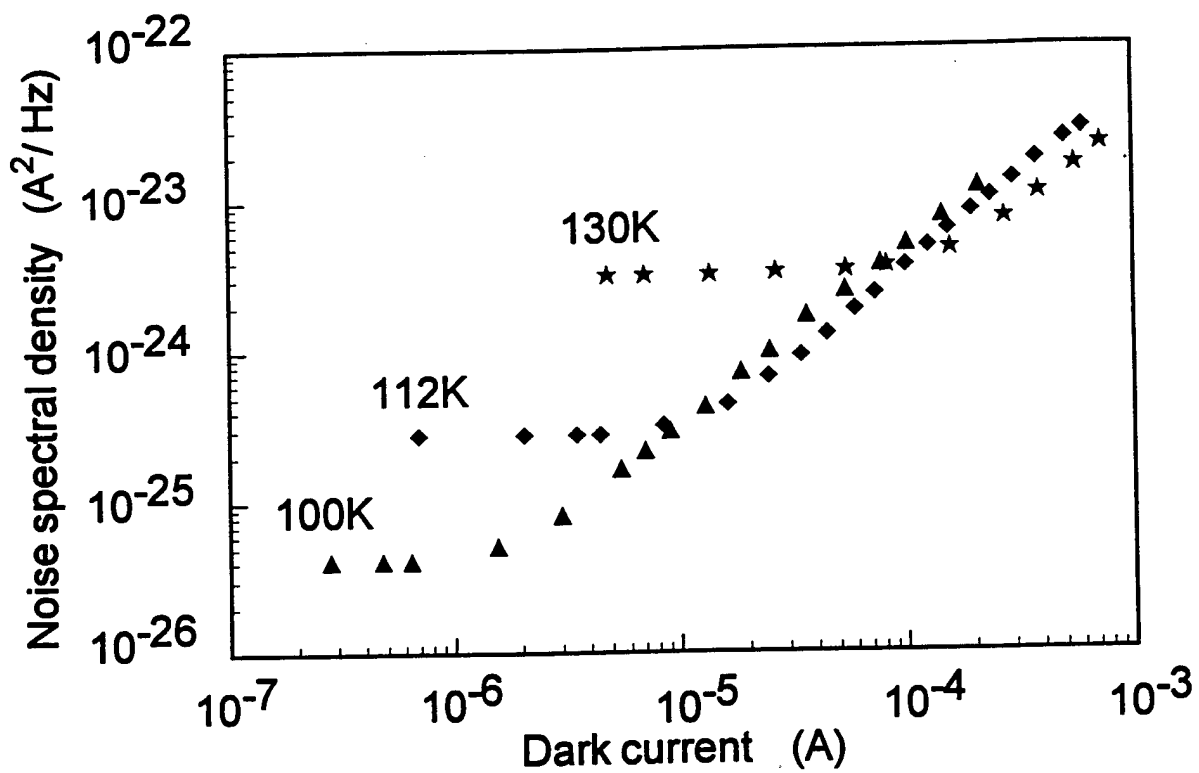


Figure 30: Current noise spectral density versus dark current for various temperatures.

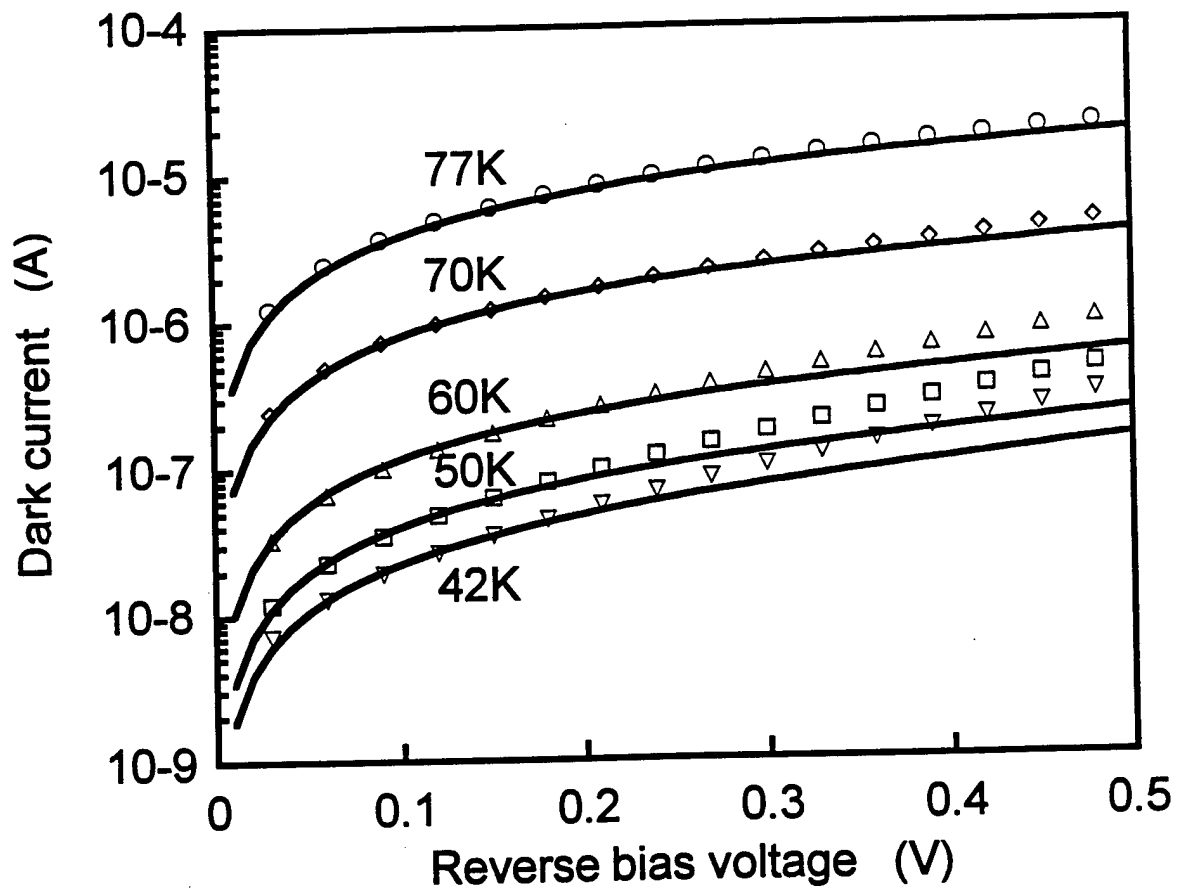


Figure 31: Measured and calculated dark currents of the 7.4  $\mu\text{m}$  peak InGaAs/AlGaAs at low bias voltages and different temperatures.

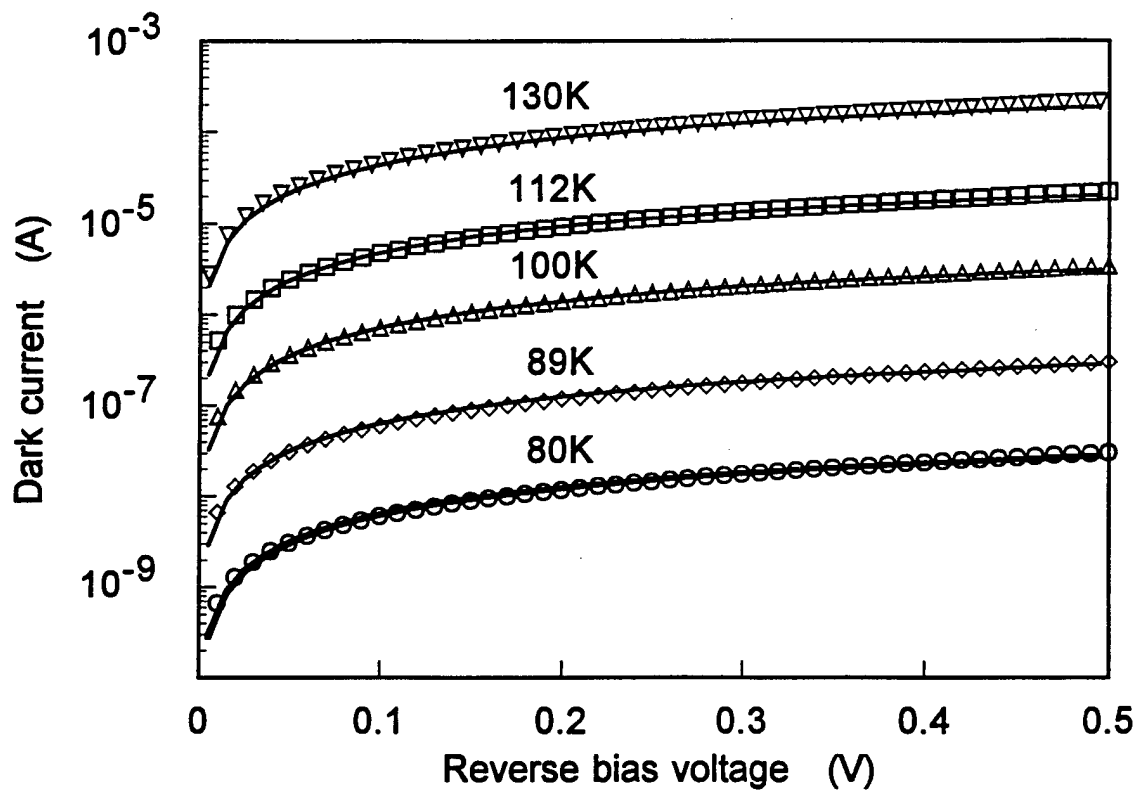


Figure 32: Measured and calculated dark current of the 9.2  $\mu\text{m}$  peak p-QWIP at low applied biases and various temperatures.

#### 4.8 A Stacked Two-color Two-band Compressively Strained-Layer P-QWIP

The p-QWIP studied in this section is a multicolor stacked P-QWIP for the MWIR and LWIR two-band detection. Figure 33 shows the energy band diagram of a stacked p-type compressively strained layer (PCSL) InGaAs/AlGaAs QWIP for the MWIR and LWIR detection. This multicolor QWIP consists of two distinct multi-quantum well stacks separated by a common ohmic contact layer and sandwiched between the two (top and bottom) ohmic contact layers. This stacked PCSL-QWIP was grown by the MBE technique on Si (100) GaAs substrate. The bottom contact consists of a heavily Be-doped GaAs contact layer. On top of the contact, the  $\text{Al}_{0.3}\text{Ga}_{0.7}\text{As}/\text{In}_{0.2}\text{Ga}_{0.8}\text{As}$  QWIP layer structure was grown for the MWIR stack. The LWIR QWIP stack was formed by using Be-doped  $\text{In}_{0.15}\text{Ga}_{0.85}\text{As}$  quantum wells surrounded with the undoped  $\text{Al}_{0.1}\text{Ga}_{0.9}\text{As}$  barrier layers. The whole stack was sandwiched between two thin  $\text{Al}_{0.1}\text{Ga}_{0.9}\text{As}$  blocking barriers. Finally, heavily Be-doped GaAs layers were grown for the top and middle ohmic contacts. Both the LWIR and MWIR quantum wells are in biaxial compression. This multicolor stacked QWIP used the bound-to-quasi-bound (BTQB) intersubband transition scheme for detection of MWIR and LWIR radiation.

In order to evaluate the performance of the QWIP, a mesa structure with area of  $216 \times 216 \mu\text{m}^2$  was formed on the MBE grown QWIP wafer by wet chemical etching for radiometric and electrical characterization. A narrow ring of Cr/Au film was deposited by E-beam evaporation to create the ohmic contacts. It is noted that in this type of mesa and ring contact structures, the normal incidence IR radiation is allowed only one pass through the QWIP stack.

For this multicolor stacked QWIP, three mesa structures of different thicknesses were etched to allow separate characterization of the LWIR, MWIR, and the combined stacked QWIP devices. The LWIR QWIP mesa structure was formed using the top and middle ohmic contacts, while the MWIR QWIP mesa structure had the top LWIR stack etched away before the mesa formation. The combined stacked QWIP used the top and bottom ohmic layers for contacts.

The device characterization was performed in a closed cycle helium cryogenic dewar. An HP 4145B semiconductor parameter analyzer was used to measure the dark I-V characteristics and the 300 K background photocurrent. Under dark conditions, holes can be

transferred out of the quantum wells and produce the observed dark current mainly due to two mechanisms: the thermionic emission out of the quantum wells and thermally generated carriers tunneling through the superlattice barriers.

The dark I-V characteristic for the MWIR, LWIR, and the combined stacked QWIP measured at  $T = 77$  K is shown in Fig. 34(a). As expected the dark current of the LWIR QWIP stack is several orders of magnitude higher than the MWIR QWIP stack, due to the exponential dependence of the dark current on the barrier height. As clearly seen in Fig. 34(a), most of the voltage drop is across the MWIR stack due to the much larger dynamic resistance of the MWIR stack. Figure 34(b) shows the measured I-V curves at  $T = 40, 60,$  and  $77$  K for the LWIR QWIP stack. The asymmetry in the dark I-V characteristics observed in this device can be attributed to the dopant migration effect [32].

The spectral responsivity for the MWIR QWIP measured at  $V = 5$  V and  $T = 77$  K is shown in Fig. 35. The responsivity measurements were performed with the device mounted in a closed cycle helium dewar and illuminated by a blackbody source running through a grating monochromator and appropriate IR filters. The resulting photocurrent is amplified and detected by a lock-in amplifier. Results of the measurements revealed that two photoresponse peaks were observed in the MWIR band at  $\lambda_{p,mw1} = 4.8$   $\mu\text{m}$  and  $\lambda_{p,mw2} = 5.4$   $\mu\text{m}$ . The  $4.8$   $\mu\text{m}$  peak is in excellent agreement with the ground heavy hole (HH1) to second bound heavy hole (HH3) transition calculated by the TMM, which predicts a detection peak at  $4.7$   $\mu\text{m}$ . The detectivity for this MWIR peak was determined to be  $D^* = 3.3 \times 10^{11}$   $\text{cm}\sqrt{\text{Hz}}/\text{W}$  at  $V_b = 1.0$  V and  $T = 77$  K. The measured spectral bandwidth for the first MWIR peak was found to be  $\Delta\lambda/\lambda_{p,mw1} = 21\%$  and  $\Delta\lambda/\lambda_{p,mw2} = 26\%$  for the second peak. The second, longer wavelength peak is attributed to the transition from the HH1 states to the second bound light hole (LH2) states within the quantum well. The calculated responsivity peak for this transition is  $5.6$   $\mu\text{m}$ , which is also in good agreement with the measured value. The higher responsivity of the  $5.4$   $\mu\text{m}$  peak is attributed to the higher absorption coefficient inherent with the HH to LH transition. The spectral detectivity for this MWIR peak was found to be  $5.5 \times 10^{11}$   $\text{cm}\sqrt{\text{Hz}}/\text{W}$  at  $V_b = 1.0$  V and  $T = 77$  K.

The responsivity for the LWIR QWIP stack as a function of the wavelength is shown in Fig. 36. A peak detection wavelength at  $\lambda_{p,lw} = 10.0$   $\mu\text{m}$  was found for the LWIR QWIP device, which is in excellent agreement with the calculated value of  $10$   $\mu\text{m}$  from the TMM.

The maximum responsivity measured at  $T = 40$  K and  $V = 2.0$  V was found to be 25 mA/W, with a detectivity of  $1.1 \times 10^{10}$  cm $\sqrt{Hz}$ /W under the same conditions. It is interesting to note that a very broad response with full width at half maximum bandwidth of 40% was achieved for this device. Figure 37 shows the relative spectral response of the combined MWIR and LWIR QWIP stack, displaying one dominant response band at MWIR and two smaller response peaks at LWIR bands.

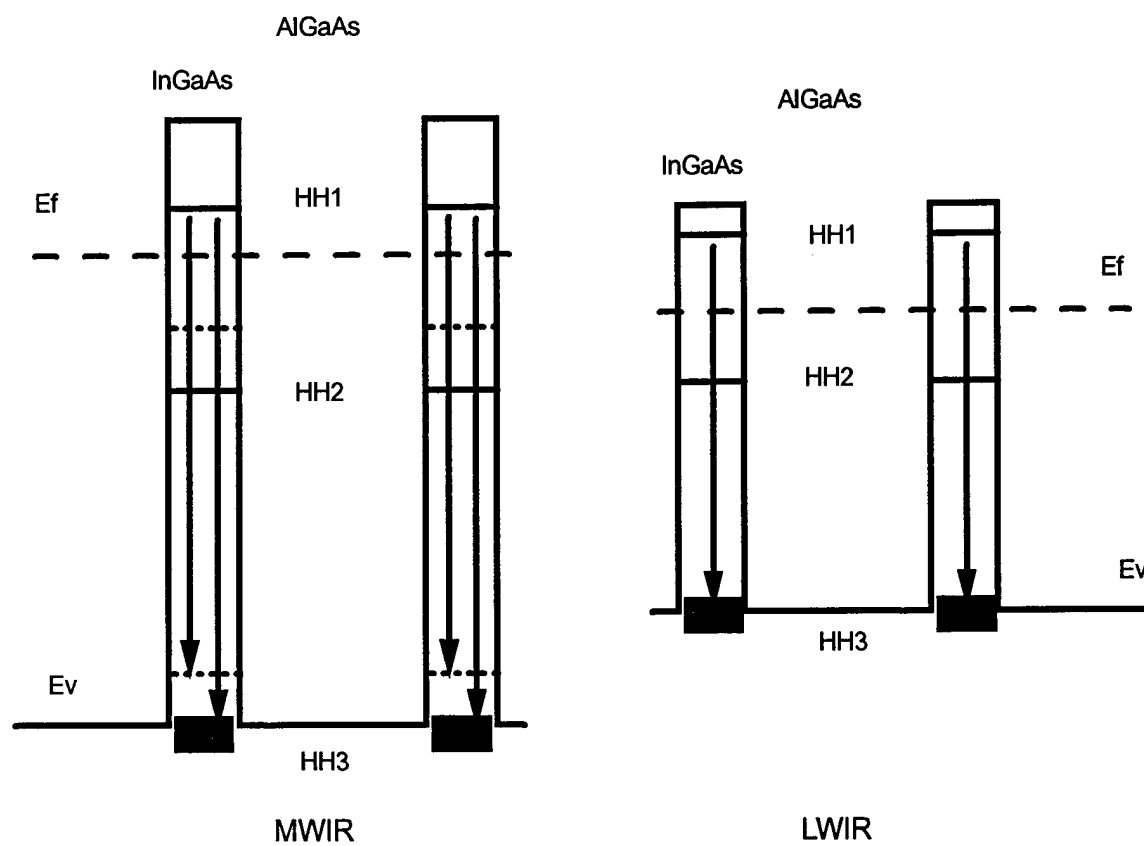
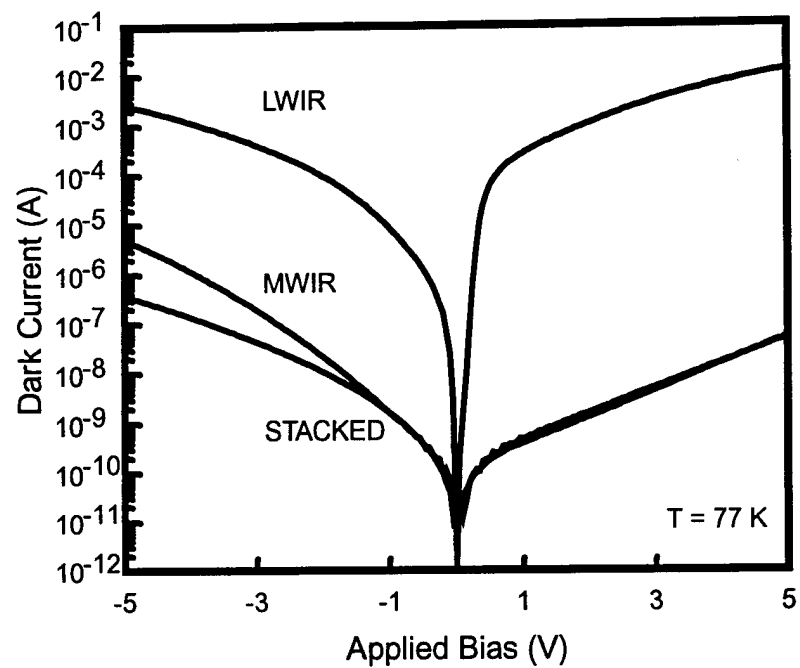


Figure 33: The energy band diagrams and intersubband transition scheme for the two-color stacked PCSL-InGaAs/AlGaAs QWIP for the MWIR and LWIR detection.



(a)

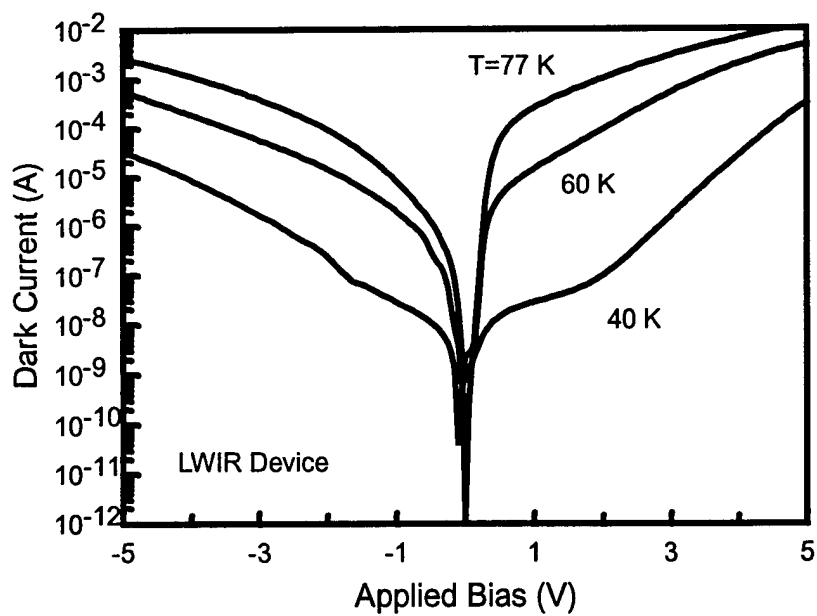


Figure 34: The dark I-V characteristics for (a) the stacked, MWIR, and LWIR PCSL-QWIP, and (b) the LWIR QWIP for  $T = 40, 60,$  and  $77$  K.



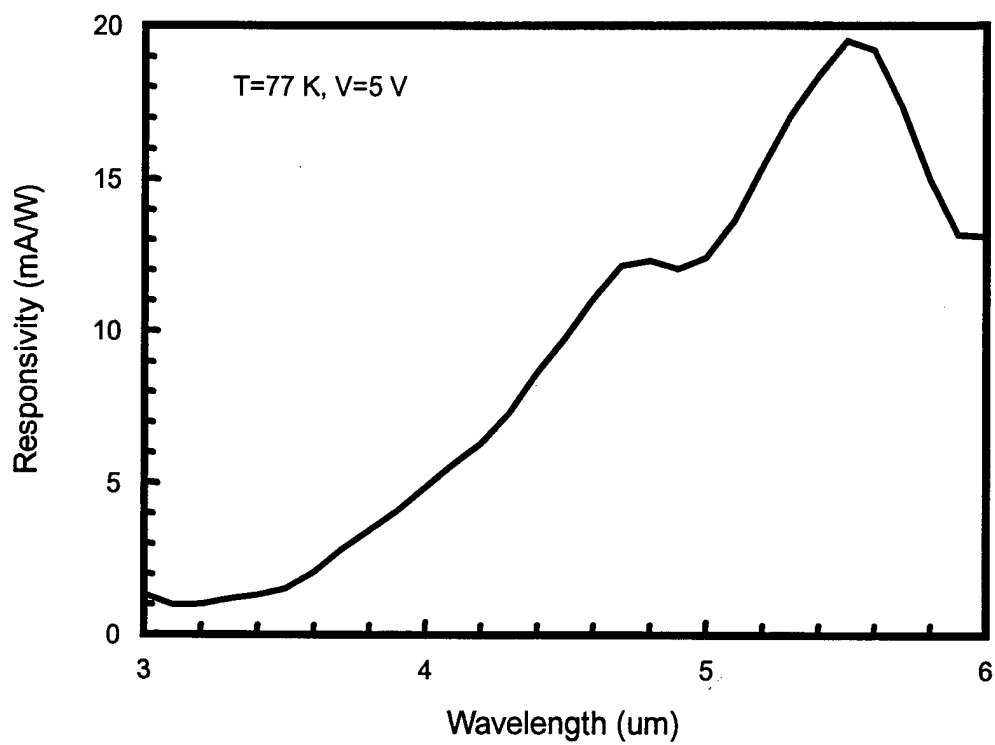


Figure 35: The spectral responsivity versus wavelength for the MWIR PCSL-QWIP, measured at  $T = 77$  K and  $V = 5$  V. Two response peaks at  $4.8 \mu\text{m}$  and  $5.4 \mu\text{m}$  were observed for this device.

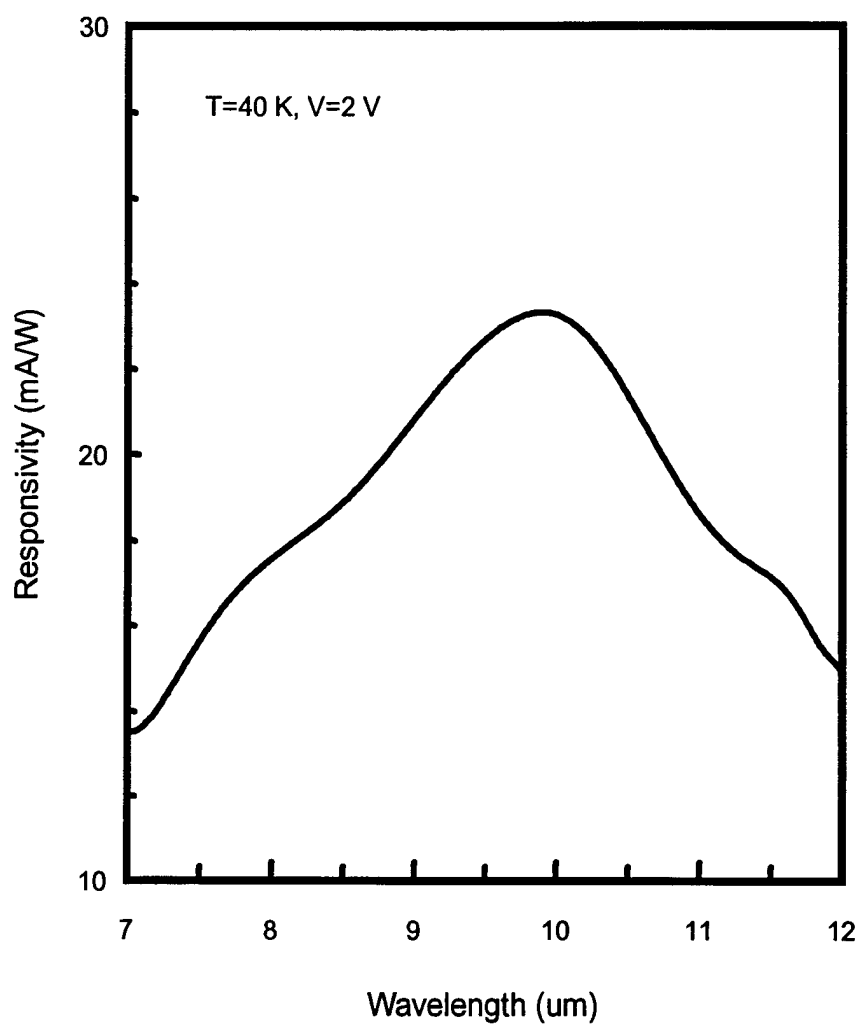


Figure 36: The spectral responsivity versus wavelength for the LWIR PCSL-QWIP, measured at  $T = 40$  K and  $V = 2$  V. One response peak at  $10 \mu\text{m}$  was obtained for this device.

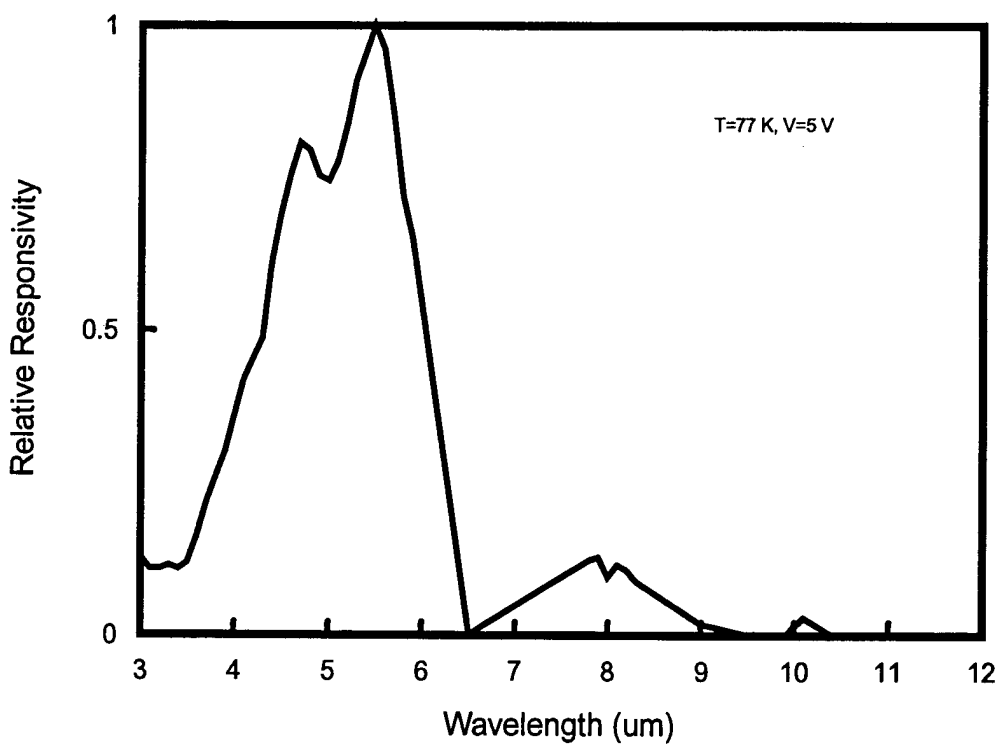


Figure 37: The relative photoresponse versus wavelength for the combined stacked PCSL-QWIP. Three photoresponse bands were detected in this stacked QWIP.

## 5 SUMMARY AND CONCLUSIONS

During this research program, we have achieved a better understanding in regards to the design and characterization of P-QWIPs. We demonstrated a novel strained-layer design that utilizes biaxial tension on an InP substrate with ultra-low dark current, high detectivity, high responsivity, and high BLIP operation. This design achieved the highest BLIP temperature ( $T \leq 90$  K) over a large bias range with a responsivity peak at  $8.1 \mu\text{m}$ , with a corresponding detectivity of  $5.9 \times 10^{10} \text{ cm}\sqrt{\text{Hz}}/\text{W}$  at 77 K. We have also demonstrated several reliable, novel compressively strained-layer designs on a GaAs substrate with detection peaks at 7.4, 8.4, 8.9, 9.2, and  $10.1 \mu\text{m}$  in the LWIR band and  $5.5 \mu\text{m}$  in the MWIR band with high detectivity, high responsivity, and high gain. We have demonstrated detectivities of  $4.0 \times 10^9$ ,  $1.66 \times 10^{10}$ ,  $2.7 \times 10^9$ , and  $1.04 \times 10^9 \text{ cm}\sqrt{\text{Hz}}/\text{W}$  with the 8.9, 7.4, 9.2,  $10.1 \mu\text{m}$  peak wavelength p-QWIPs. We have shown the application of p-type QWIPs with step bound-to-miniband transition schemes in an effort to lower dark current and noise levels while maintaining normal incidence detection and responsivity. The current p-type SBTM CSL-QWIPs exhibit a LWIR detection peak at  $10.4 \mu\text{m}$  with a corresponding  $D^* = 1.4 \times 10^9 \text{ cm}\sqrt{\text{Hz}}/\text{W}$  at  $T=65$  K and  $V=1$  V. Additional effort has been made in the modeling of the dark current characteristics for the 9.2 and  $7.4 \mu\text{m}$  peak compressively strained p-QWIPs, along with the analysis of the noise performance of the  $7.4 \mu\text{m}$  peak p-type compressively strained p-QWIP. Furthermore, multispectral capabilities on single and two-stack p-QWIPs have been studied with single devices that exhibit detection peaks at 7.4, 8.4, and  $8.9 \mu\text{m}$  in the LWIR band and  $5.5 \mu\text{m}$  in the MWIR band. The stacked CSL p-QWIP was analyzed with detection peaks at  $10 \mu\text{m}$  in the LWIR band with corresponding peaks at 4.8 and  $5.4 \mu\text{m}$  in the MWIR band. We were able to achieve detectivities of  $1.1 \times 10^{10}$  and  $5.5 \times 10^{11} \text{ cm}\sqrt{\text{Hz}}/\text{W}$  for the respective LWIR and MWIR peaks for this stacked device. Finally, in a comparison of p-type unstrained QWIPs and compressively strained p-QWIPs, we found that the performance of CSL p-QWIPs is roughly one order of magnitude higher, when comparing responsivities and detectivities for specific cut-off wavelengths, than the unstrained p-QWIPs, as seen in figure 38. While CSL p-QWIPs still exhibit slightly lower detectivities than n-type QWIPs, consideration must be given to the fact that p-QWIPs are inherently normal incidence devices, so that processing is simplified and that all of the devices explored in this research program have not been optimized, in terms of

periodicity, barrier width, and focal plane array structure (*e.g.*, backside thinning and top contact reflectors for multiple pass waveguide-like structures). There is still more work that needs to be done in order to further improve the performance of strained-layer p-QWIPs.

<i>Device</i> (strain)	$\lambda_p$ ( $\mu\text{m}$ )	<i>Responsitivity</i> (mA/W)	<i>Dark Current Density</i> (A/cm <sup>2</sup> ) @ 77 K, 1 V
InGaAs/InAlAs (tensile)	8.1	18	$5 \times 10^{-8}$
InGaAs/GaAs (compressive)	8.9, 8.4, 5.5	45	$2.5 \times 10^{-2}$
InGaAs/AlGaAs (compressive)	7.4, 5.5	38	$1.1 \times 10^{-4}$
InGaAs/AlGaAs (compressive)	9.2	28	$1.6 \times 10^{-2}$
InGaAs/AlGaAs (compressive)	10.1	17	$5 \times 10^{-2}$
InGaAs/GaAs/AlGaAs (compressive)	10.4	25	$4 \times 10^{-2}$
InGaAs/GaAs/AlGaAs (LWIR stack, compressive)	10.0	25	$6 \times 10^{-2}$
InGaAs/GaAs/AlGaAs (MWIR stack, compressive)	4.8, 5.4	12, 19	$6.5 \times 10^{-7}$

Table A. Comparison of the strained layer p-QWIPs studied.

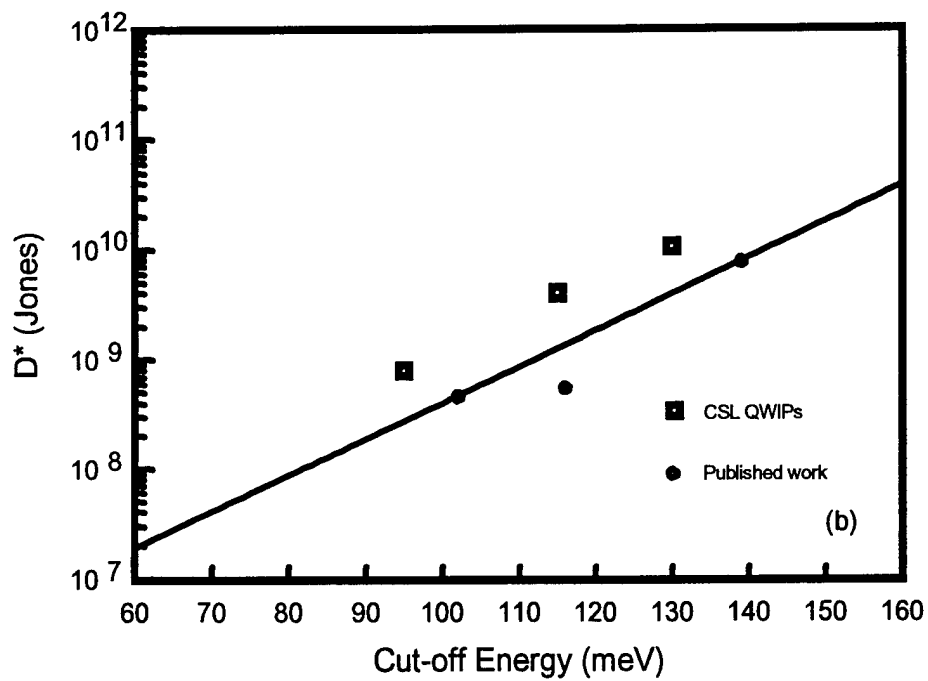
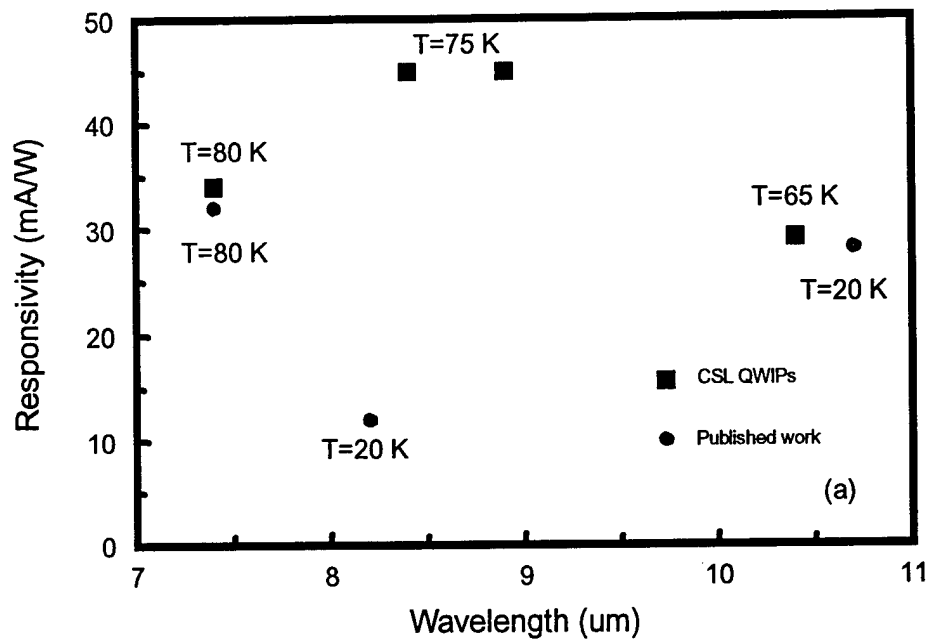


Figure 38: The comparison of the (a) photoresponse and (b) detectivity between the strained and unstrained p-QWIPs at the same operating biases.

## References

- [1] B. F. Levine, R. J. Malik, J. Walker, K. K. Choi, C. G. Bethea, D. A. Kleinman, and J. M. Vandenberg, *Appl. Phys. Lett.* **50**, 273 (1987).
- [2] L. S. Yu, S. S. Li, *Appl. Phys. Lett.* **59**, 1332 (1991).
- [3] G. Hasnain, B. F. Levine, C. G. Bethea, R. A. Logan, J. Walker, and R. J. Malik, *Appl. Phys. Lett.* **54**, 2515 (1989).
- [4] J. Y. Andersson and L. Lundqvist, *J. Appl. Phys.* **71**, 3600 (1992).
- [5] B. F. Levine, S. D. Gunapala, J. M. Kuo, S. S. Pei, and S. Hui, *Appl. Phys. Lett.* **59**, 1864 (1991).
- [6] J. Katz, Y. Zhang, and W. I. Wang, *Electron. Lett.* **28**, 932 (1992).
- [7] W. S. Hobson, A. Zussman, B. F. Levine, and J. deJong, *J. Appl. Phys.* **71**, 3642 (1992).
- [8] J. W. Matthews and A. E. Blakeslee, *J. Cryst. Growth* **32**, 265 (1976).
- [9] Landolt-Börnstein, "Numerical Data and Functional Relationships in Science and Technology", O. Madelung, ed., Group III, **17a**, **22a**, Springer-Verlag, Berlin (1986).
- [10] G. Ji, D. Huang, U. K. Reddy, T. S. Henderson, R. Houre, and H. Morkoç, *J. Appl. Phys.* **62**, 3366 (1987).
- [11] T. P. Pearsall, *Semiconductors and Semimetals*, **32**, 55 (1990).
- [12] H. Asai, and Y. Kawamura, *Appl. Phys. Lett.* **56**, 746 (1990).
- [13] H. Xie, J. Katz, and W. I. Wang, *Appl. Phys. Lett.* **59**, 3601 (1991).
- [14] R. T. Kuroda and E. Garmire, *Infrared Phys.* **34**, 153 (1993).
- [15] L. R. Ram-Mohan, K. H. Yoo, and R. L. Aggarwal, *Phys. Rev B* **38**, 6151 (1988).
- [16] J. M. Luttinger and W. Kohn, *Phys. Rev.* **97**, 869 (1956).
- [17] J. M. Luttinger, *Phys. Rev.* **102**, 1030 (1956).
- [18] G. L. Bir and G. E. Pikus, "Symmetry and Strain-Induced Effects in Semiconductors", Wiley, New York (1974).
- [19] E. L. Derniak and D. G. Crowe, *Optical Radiation Detectors*, Wiley, New York (1984).
- [20] B. F. Levine, C. G. Bethea, G. Hasnain, J. Walker, and R. J. Malik, *Appl. Phys. Lett.* **53**, 296 (1988).
- [21] D. A. Scribner, M. R. Kruer, and J. M. Killiany, *Proc. of the IEEE* **79**, 66, (1991).



- [22] R. Hull, J. C. Bean, F. Cerdeira, A. T. Fiory, and J. M. Gibson, Appl. Phys. Lett. **48**, 56 (1986).
- [23] E. O. Kane, "Semiconductors and Semimetals", eds. R. K. Willardson and A. C. Bear, **1**, 75 (1966).
- [24] F. H. Pollack, "Semiconductors and Semimetals", ed. T. P. Pearsall, **32**, 17 (1990).
- [25] Y. C. Chang and R. B. James, Phys Rev. **B-39**, 672 (1989).
- [26] P. Man and D. S. Pan, Appl. Phys. Lett. **61**, 2799 (1992).
- [27] S. K. Chun, D. S. Pan, and K. L. Wang, Phys. Rev. **B-47**, 15638 (1993).
- [28] B. F. Levine, J. Appl. Phys. **74**, R1 (1993).
- [29] J. W. Matthews and A. E. Blakeslee, J. Cryst. Growth **27**, 118 (1974).
- [30] J. W. Matthews and A. E. Blakeslee, J. Cryst. Growth **29**, 273 (1975).
- [31] K. Hirose, T. Mizutani, and K. Nishi, J. Cryst. Growth **81**, 130 (1987).
- [32] H. C. Liu, Z. R. Wasilewski, and M. Buchanan, Appl. Phys. Lett. **63**, 761 (1993).
- [33] A. K. Ghatak, K. Thyagarajan, and M. R. Shenoy, IEEE J. Quantum Electron. **24**, 1524 (1988).
- [34] H. C. Liu, Appl. Phys. Lett. **60**, 1507 (1992).
- [35] H. C. Liu, Appl. Phys. Lett. **61**, 2703 (1992).
- [36] W. A. Beck, Appl. Phys. Lett. **63**, 3589 (1993).
- [37] S. D. Gunapala, B. F. Levine, and K. West, J. Appl. Phys. **69**, 6517 (1991).
- [38] D. C. Wang, G. Bosman, Y. H. Wang, and S. S. Li, J. Appl. Phys. **77**, 1107 (1995).
- [39] Y. H. Wang, S. S. Li, J. Chu, and Pin Ho, Appl. Phys. Letts., **64**, 727 (1994).
- [40] Y. H. Wang, J. C. Chiang, and S. S. Li, and Pin Ho, J. Appl. Phys. **76**, 2538 (1994).
- [41] L. S. Yu, Y. H. Wang, and S. S. Li, Appl. Phys. Lett. **60** (8), 992 (1992).
- [42] A. Rose, "Concepts in Photoconductivity and Allied Problems", Wiley-Interscience, New York, 1963.
- [43] R. H. Bube, "Electronic Properties of Crystalline Solids", Academic Press, New York, 1974.